Print ISSN 0033-9008
Online ISSN 1880-1765

QUARTERLY REPORT of RTRI

May 2026 Vol. 67 No. 2

CONTENTS

[H] Human factors
[I] Infrastructure
[N] Natural hazards
[O] Operations
[R] Rolling stock
[T] Technical system integration and interaction

RAILWAY TECHNICAL RESEARCH INSTITUTE

QUARTERLY REPORT of RTRI

Print ISSN 0033-9008
Online ISSN 1880-1765

May 2026 Vol. 67 No. 2

CONTENTS

PAPERS

SUMMARIES

[H] Human factors
[I] Infrastructure
[N] Natural hazards
[O] Operations
[R] Rolling stock
[T] Technical system integration and interaction

Evaluation of Cytotoxicity Threshold Induced by Thermal Effects of Millimeter-wave Electromagnetic Fields

Masateru IKEHATA **Sachiko YOSHIE**
Comfort Science and Engineering Laboratory, Human Science Division

Yukihisa SUZUKI
Tokyo Metropolitan University

Hiroshi SASAKI
Kanazawa Medical University

Recent advances in information processing technology have improved wireless data communication across various areas, including railway systems. This study investigated the health effects of 60 GHz millimeter-wave electromagnetic fields (MMW-EMFs), which are used in next-generation communication technology, on the human body. We conducted experiments using three-dimensional tissue models constructed from normal human cells. The threshold for cell damage was between 180-250 mW/cm² with 6-minute exposure under standard conditions. This duration is the evaluation time for current regulatory compliance. Under high-temperature and high-humidity conditions (42.5°C, 80% humidity), the threshold decreased to between 130-150 mW/cm². This mechanism is attributed to thermal factors, and it was found that cell surface temperatures exceeding 50°C can be a condition that causes damage.

Key words**:** *millimeter-wave (MMW), thermal effects, health risks of electromagnetic fields, reconstructed skin tissue model, radio wave protection guidelines (RRPG), cell experiments*

1. Introduction

The development and use of radio wave (EMF) resources is a major imperative for Japan. However, ensuring safety when new frequency bands and technologies are implemented in society is essential, because safety is a prerequisite for social acceptance.

The Ministry of Internal Affairs and Communications (MIC) supervises radio wave use in Japan. It collects scientific data on the health impacts of radio waves through a bioelectromagnetic research framework and develops evaluation technologies.

This study reports the results of an investigation, commissioned by the MIC, into thermal injury thresholds in 60 GHz *in vitro* experiments. The aim of this study is to obtain fundamental knowledge regarding the safety of ultra-high frequency EMFs, which are being developed for future deployment on the railways.

2. Background

2.1 Emerging EMF technologies and safety considerations

Railway systems consist of various elemental technologies. Almost all train operating equipment is electrical or composed of electronic devices. This creates an extremely complex electromagnetic environment in railway vehicles and facilities.

Different frequency bands have different EMF sources. In the extremely low frequency band below 300 Hz, stray EMFs originate from power supply systems and traction motors. In the intermediate frequency band (300 Hz to several kHz), stray EMFs originate from main inverters. In the high frequency band (several hundred MHz and above), EMFs are commonly employed for communications. These EMFs are very weak, however, they show significant temporal and spatial variations.

On the other hand, from a societal perspective there has been considerable interest in the health effects of "EMFs," since the late 1970s when a U.S. epidemiologist reported an association between EMFs from power transmission lines and the risk of childhood leukemia [1]. Today, worry about well-known EMF sources (such as mobile telephony and power transmission lines) is compounded by concern about a growing number of sources encountered daily. Examples include public transport systems using electrified vehicles, induction heating devices, contactless IC cards, anti-theft devices, RFID technology, inter alia. However, adverse health risks from weak environmental EMF exposure have not been clarified. This lack of knowledge is thought to contribute to growing anxiety about EMFs. Therefore, evaluating health risks and clarifying the health impact of EMFs based on scientific evidence is important.

For this reason, the Railway Technical Research Institute has evaluated various electromagnetic field exposures. These include static magnetic fields [2], commercial frequency EMFs [3], intermediate frequency EMFs [4], and combined exposures [5, 6]. These fields are generated by various railway technologies. Examples include newly developed superconducting magnetically levitated trains and commercial electrified trains.

Our research shows that effects can be detected under scientifically rigorous conditions. However, the effects from environmental exposure, where effects exist, have been found to be negligible.

Furthermore, since the fiscal year 2020, Japan has been rolling out fifth-generation mobile communication technology (5G). This enables high-speed, large-capacity communications. In the railways, applications for train-to-ground communications and train control are also being developed.

This is expected to be followed by sixth-generation (6G) and seventh-generation (7G) mobile communication technologies. This will expand utilization of electromagnetic field resources in the 30-300 GHz range. In the railways, technologies using the 100 GHz frequency band [7] are also advancing. These enable high-capacity, high-speed wireless communication with high-speed trains.

Such technologies will be used on railways to enable high-capacity, high-speed wireless data communications. They will contribute to maintaining the safety and security of public transportation networks, including railways, by virtue of data sensing, wireless power transmission, and non-destructive inspection, inter alia.

Additionally, various personal devices utilizing electromagnetic fields at higher frequencies are being developed. Examples include mobile phone terminals, wearable devices, VR goggles, wireless LAN terminals, and wristwatches with 60 GHz band millimeter-wave radar. Electromagnetic field exposure scenarios in daily environments will become more complex.

On the other hand, to develop the utilization of electromagnetic fields, it is necessary to ensure the safety of EMFs for humans and equipment. As such, careful evaluation is particularly necessary with regard to health risks for humans.

2.2 Human protection against radio wave in Japan

In Japan, MIC manages radio wave frequency EMF resources. In response to the rapid spread of mobile wireless communication, the Radio Radiation Protection Guidelines (RRPG) were established in 1990 [8] These guidelines are designed protect the human body from radio wave exposure.

The MIC has introduced regulations under the Radio Act for EMFs from 10 kHz to 300 GHz. These are based on the RRPG. Interference with wireless communications and effects on medical devices and electronic equipment are examined separately under the heading of electromagnetic compatibility (EMC). Regulations for EMC were introduced in part of the same Radio Act and the Electrical Appliance and Material Safety Act of the Ministry of Economy, Trade and Industry.

In the RRPG, biological effects of EMFs that have been clarified and scientifically validated are designated as targets for protection. The types of effects specifically targeted include, for example, nerve stimulation below 100 kHz and thermal effects above 100 kHz. In principle, to prevent these effects from occurring or to prevent physiological change as a result of these effects, “basic restrictions” have been established by applying interpolation and extrapolation across all frequency bands. They are based on scientific evidence relating to effect thresholds with added safety factors. These basic restrictions led to “reference levels.” These are standard values for measurable physical quantities. Examples include electric field strength, magnetic field strength, power density, specific absorption rate, and incident power density.

Reference levels are broadly divided into two categories: “controlled environment (occupational exposure)” and “general public environment.” Each incorporates safety factors appropriate to its environment based on basic restrictions (Tables 1, 2, and 3). These standard values comply with guidelines developed by the International Commission on Non-Ionizing Radiation Protection (ICNIRP) [9] and the International Committee on Electromagnetic Safety (ICES) of IEEE [10].

Nevertheless, ultra-high frequency EMF use, such as MMW electromagnetic fields, is progressing. Meanwhile, the biological evidence needed to support the thermal effect thresholds underlying the current guideline’s basic restrictions is insufficient. This evidence should be based on actual biological material data. Studies examining tissue damage thresholds are particularly limited, and

Table 1 EMF strength guideline values used for protection against stimulation effects in a general environment

Frequency f	rms electric field strength E [V/m]	rms magnetic field strength H [A/m]	rms magnetic flux density [T]
10 kHz-10 MHz	83	21	2.7×10^{-5}

Table 2 EMF strength guideline values for a general environment (Averaging time: 6 min)

Frequency f	rms electric field strength E [V/m]	rms magnetic field strength H [A/m]	Power density S [mW/cm^2]
100 kHz-3 MHz	275	$2.18f^{-1}$	
3 MHz-30 MHz	$824f^{-1}$※1	$2.18f^{-1}$	
30 MHz-300 MHz	27.5	0.0728	0.2
300 MHz-1.5 GHz	$1.585f^{1/2}$	$F^{1/2}/237.8$	f/1500
1.5 GHz-300 GHz	61.4	0.163	1

※1:f is the frequency in MHz (e.g., 30 for 30 MHz, 1500 for 1.5 GHz)

Table 3 Partial-body absorption guidelines (General environment, Averaging time: 6 min)

Frequency f	Index	Standard value
100 kHz-6 GHz	local SAR※1	2 W/kg for any 10 g of tissue (4 W/kg for limbs)
6 GHz-30 GHz	Incident power density※2	2 mW/cm^2 for any 4 cm^2 of body surface※3
30 GHz-300 GHz		2 mW/cm^2 for any 1 cm^2 of body surface※3

※1: “Specific Absorption Rate (SAR)” refers to the amount of energy absorbed per unit mass of tissue per unit time when a living organism is exposed to an electromagnetic field.

※2: “Incident power density” refers to the power passing through per unit area perpendicular to the direction of electromagnetic wave propagation.

※3: Any spaceto be occupied by the human body

few examples exist beyond research by the authors [11, 12]. Therefore, accumulating scientific evidence is required for health risk assessments, especially considering practical exposure scenarios.

2.3 Scheme of research project

This study forms part of a collaborative project entitled, "Research on Ocular Injury Thresholds from Radio Wave Exposure under Various Environmental Conditions" conducted by three institutions: the Railway Technical Research Institute, Kanazawa Medical University, and Tokyo Metropolitan University. It operates under the MIC's bioelectromagnetic research initiative.

As shown in Fig. 1, this research project aimed to identify biological effect thresholds. Specifically, it targeted injury thresholds from electromagnetic field exposure in the millimeter-wave frequency band. New mobile wireless communication technologies use these frequencies. Both *in vitro* and *in vivo* experiments were conducted.

When MMW-EMFs are present in the environment and the human body is exposed to them, most power is absorbed at the body's surface. Therefore, body surface tissues such as skin and eyes are sites where biological effects should be considered.

This research project investigated three-dimensional human skin epidermis and corneal models (assigned to the Railway Technical Research Institute), as well as rabbits' eyes (assigned to Kanazawa Medical University). More specifically, this project aimed to explore injury thresholds of electromagnetic field exposure under high-temperature, high-humidity conditions. These conditions were assumed in diverse weather conditions around the world due to global warming. They were also assumed within VR goggles, as well as standard conditions.

We investigated cytotoxicity, its mechanisms, and the influence of environmental conditions on exposure effects. We used *in vitro* exposure experiments with three-dimensional reconstructed tissue models. These imitate human corneal and skin tissue structures. These findings are expected to supplement knowledge obtained from *in vivo* experiments. They provide fundamental data on mechanisms for evaluating health effects in humans. This paper reports results on experiments conducted with 60 GHz MMW-EMFs.

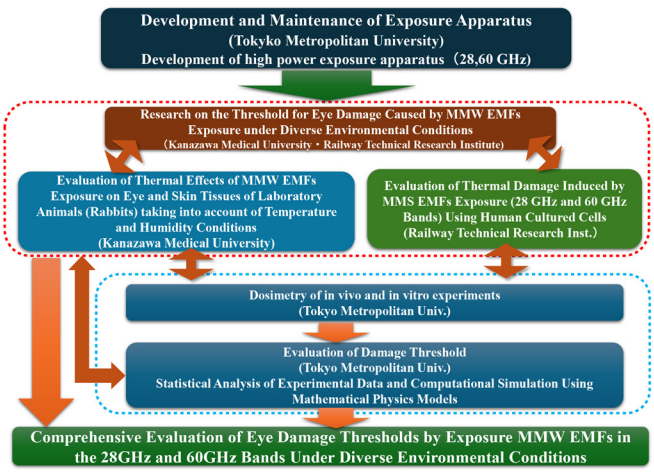

Fig. 1 Research structure of the project: Research on threshold for eye damage caused by MMW-EMFs exposure under diverse environmental conditions

3. Evaluation of cytotoxicity threshold induced due to thermal effects of millimeter-wave electromagnetic fields

This study aimed to strengthen biological evidence for EMF health risk management. We conducted experiments using biological samples composed of human cells. We used the same millimeter-wave electromagnetic field exposure conditions as the rabbit experiments. We used the same exposure equipment that had been used for rabbit exposure experiments. This evaluates thermal injury thresholds in the ultra-high frequency band. This approach allows us to obtain more detailed insights into mechanisms. It also helps us understand factors influencing species differences between rabbits and humans.

To investigate complementary data and possible species differences, we chose exposure conditions similar to those used in the rabbit experiments. These differ from normal cell culture temperature (37°C). Cells were exposed to EMFs under the following environmental conditions: 33°C and 50% RH for standard conditions, and 42.5°C and 80% RH for high-temperature, high-humidity conditions. This was based on rabbit corneal surface temperatures under standard and high-temperature, high-humidity conditions in rabbit experiments [12]. Temperature fluctuation was maintained within ±1.5°C.

The electromagnetic field exposure period was set to 6 minutes. This period is used in evaluations under Japan's Radio Act. It is also the experimental setting period for the rabbit study. Furthermore, normal cell culture is performed in a 5% carbon dioxide environment. However, preliminary experiments showed that decreased carbon dioxide concentration effects during 6-minute exposure (10 minutes total including before and after exposure) were limited. Therefore, carbon dioxide was not controlled during the exposure period.

A culture cup of the tissue model was placed directly under the lens antenna in the exposure chamber. This exposed the three-dimensional tissue model surface to the electromagnetic field from above. Exposure experiments were conducted in open-air conditions (Fig. 2). Fungal contamination of tissue models was rare. Contaminated samples were omitted from experiments.

3.1 60 GHz band electromagnetic field exposure system

This report targets the 60 GHz frequency band. The electromagnetic field exposure system was configured to induce oscillated electromagnetic fields into a chamber with constant temperature and humidity. Target cells were then exposed via a lens antenna.

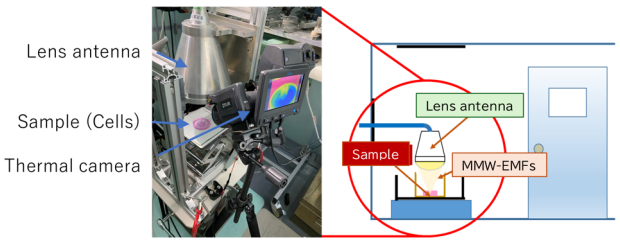

・Mount the lens antenna vertically inside a constant temperature and humidity chamber, with cells placed directly beneath it
・Expose to millimeter-wave electromagnetic fields for 6 minutes under atmospheric conditions in an open system
・Temperature and humidity conditions inside the chamber
a. Standard conditions: 33±1.5°C, 50±10 % RH
b. High temperature and humidity conditions: 42.5±2°C, 80±10 % RH

Fig. 2 Image of MMW-EMFs exposure experiments

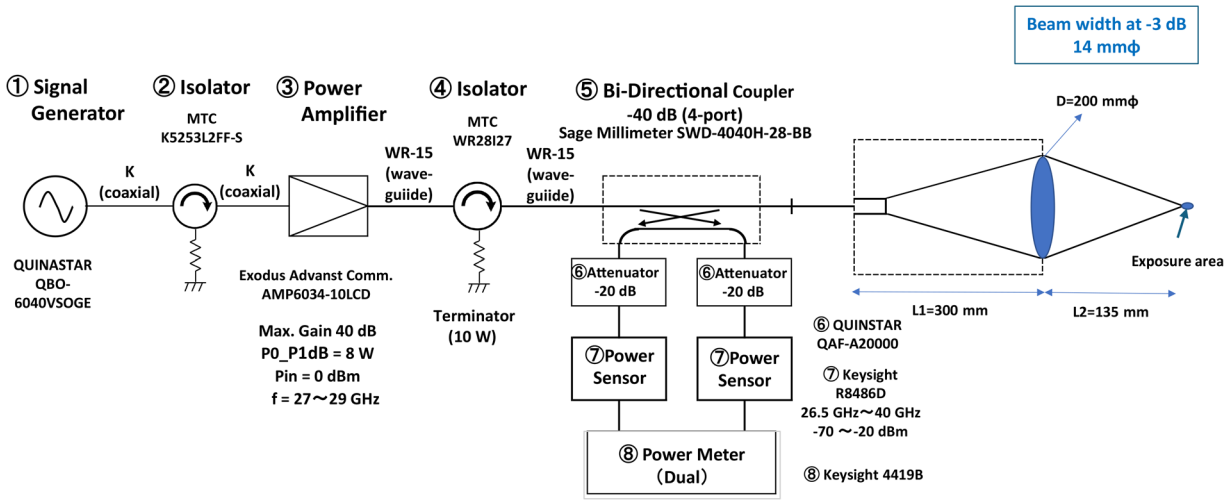

Fig. 3 Component diagram of 60 GHz MMW-EMFs exposure apparatus developed in this study

We measured the lens antenna characteristics. A -3 dB beam width of 14 mmφ or less (7.5 mmφ) was confirmed in the 60 GHz band. Figure 3 shows the electromagnetic field source. A QBO-6040VSOGE signal generator manufactured by QuinStar Technology was used.

Prior to *in vitro* exposure experiments, we measured the output characteristics at the installed lens antenna and the temperature rise in the phantom. This confirmed that the estimated range of beam distribution and incident power was appropriate.

3.2 Reconstructed three-dimensional tissue models using normal human cells

Due to MMW-EMF nature, human surface tissues are targeted. This aligns with human exposure scenarios in the environment. Several types of reconstructed human epidermis or cornea are available. These mimic the biochemical and physiological characteristics of these tissues, mainly for skin and eyes.

These have been adopted in *in vitro* experimental systems. An example is the OECD Test Guideline TG489 [13]. They evaluate skin irritation and other safety-related hazard assessment criteria.

The epidermal model Epi-12 (Japan Tissue Engineering Co., Ltd., Japan) was used as the main sample. These three-dimensional tissue models use normal human skin or corneal cells. The skin model has the same morphological layers as human epidermis. These include the basal layer, spinous layer, granular layer, and stratum corneum. Similarly, the corneal model has a structure similar to human corneal epithelial tissue.

3.3 Exposure to millimeter-wave electromagnetic field

Exposure experiments were conducted using the millimeter-wave electromagnetic field exposure system shown in Fig. 2. Prior to each experiment, we determined the relationship between incident power density, temperature rise, and its distribution as follows:

The surrounding wall of the well containing the human three-dimensional tissue model was cut off. Its center was adjusted to the lens antenna focus point using laser pointers. The well surface was then recorded with a thermal camera (T620, FLIR Systems, Inc., USA). These measurement results show the distribution of sample surface temperature. They were used to conduct exposure experiments on fresh samples at incident power densities ranging from several tens to several hundreds of mW/cm^2.

On the day of the experiment, the walls of the wells of three-dimensional tissue models used in exposure experiments were cut off in advance.

The procedure of the exposure experiments was as follows: one well of the human three-dimensional tissue model was placed in the exposure position. Recording the input power to the exposure system, thermal images, and temperature and humidity inside the exposure chamber began. The millimeter-wave electromagnetic field exposure began one minute after the sample was left unexposed. After 6 minutes of exposure, the samples were left undisturbed for one minute. Then the recording stopped, and the sample wells were collected. The collected sample wells were transferred to a carbon dioxide incubator for a 48-hour post-culture period.

The intensity of the millimeter-wave electromagnetic field during exposure experiments was examined at incident power densities ranging from 50 to 500 mW/cm^2 under standard conditions (33°C, 50%RH). Under high-temperature, high-humidity conditions (42.5°C, 80%RH), the range was 50 to 200 mW/cm^2. This was based on the initial examination of the relationship between incident power density and temperature rise.

The required number of independent exposure experiments (N=3-5) was repeated for each set of conditions. Note that the incident power density used in this study is the average incident power density in an exposure area with a diameter of 13 mm, although the -3 dB beam width of the lens antenna is 7.5 mmφ. This 13 mm diameter was chosen to ensure compatibility with rabbit experiments. In the previous rabbit study by Kojima et al. [12], the exposure area was defined as the corneal surface area exposed to the millimeter-wave beam, which corresponds to approximately 13 mm diameter when accounting for the rabbit eye geometry. To maintain consistency in dose metrics between *in vitro* and *in vivo* experiments, we adopted the same spatial averaging diameter. This approach allows direct comparison of incident power density thresholds between the two experimental models, despite differences in the physical setup. The power distribution within this 13 mm diameter area follows a Gaussian profile, with the highest intensity at the center (7.5 mm beam width at -3 dB) and decreasing intensity toward the periphery.

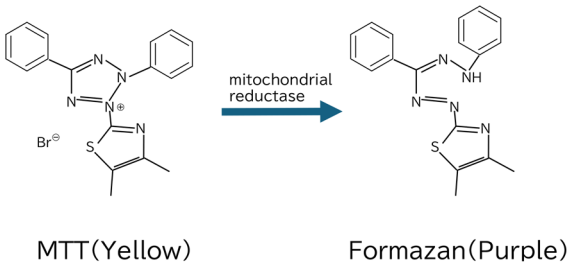

Fig. 4 Key reaction of MTT assay

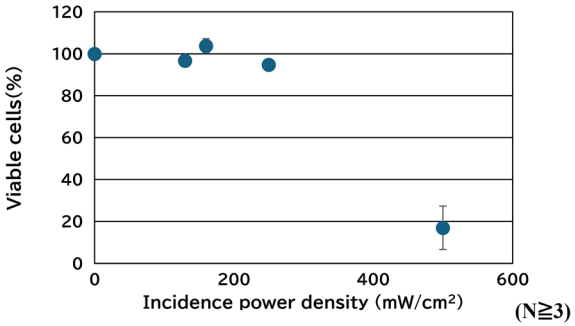

Fig. 5 Evaluation of cell damage by absorbance using MTT assay in standard condition

3.4 Evaluation method for cytotoxicity by MTT assay

The MTT assay is a colorimetric method for measuring viable cell numbers (absorbance at 570 nm). It is based on MTT reduction. MTT is [3-(4,5-dimethyl-thiazol-2-yl)-2,5-diphenyltetrazolium bromide], a tetrazolium salt. Mitochondrial dehydrogenase in cells takes it up to produce formazan, a purple substance. The amount of formazan correlates with the number of metabolically active cells (Fig. 4).

The experimental procedure is as follows. After electromagnetic field exposure, all experimental samples were post-cultured in the same 33°C CO_2 incubator used for pre-culture for approximately 42 hours. The samples were then transferred to a plate containing warmed MTT medium at 37°C. They were left to react for 3 hours.

After the reaction, the insert cup bottom surface was washed with phosphate-buffered saline (PBS). The washed insert cup was transferred to a new 12-well plate (1 ml of PBS dispensed into each well) and stored at 4°C. The three-dimensional tissue model surface in the insert cup was photographed before and after storage.

Subsequently, the three-dimensional tissue model was peeled off from the insert cup with tweezers. It was immersed in isopropanol for at least one night to completely extract the formazan that is the product of MTT reduction.

The extract absorbance at 570 nm and 650 nm was measured. Using isopropanol as control, the value obtained by subtracting absorbance (650 nm) from absorbance (570 nm) was taken as the measured value (Equation 1):

Measured value = <Absorbance of sample (570 nm - 650 nm)> - <Absorbance of control (570 nm - 650 nm)> ... (1)

Based on this measured value, the viable cell rate of the exposed sample was calculated from Equation (2):

Viable cell rate (%) = (Average measured value of exposed sample / Average measured value of control) × 100 ... (2)

As described later, electromagnetic field exposure is non-uniform. Effects leading to cell damage appear concentrically from the center. The sample state after exposure is not homogeneous. The MTT assay usually targets homogeneous samples. Therefore, the values of extracted dye were used as a reference.

In determining the threshold for cell damage, we did not rely on the absorbance measurement data described above. Instead, the determination was based on the presence or absence of cell damage using the taken images as a basis.

3.5 Evaluation results of injury threshold

MTT staining evaluates serious effects due to electromagnetic fields. The index shows decreased cellular activity, including whether cells have died. Generally, when conducting *in vitro* experiments, the fundamental approach is to expose all cells uniformly to the agent being evaluated.

However, uniform millimeter-wave electromagnetic field exposure over the tissue model surface is difficult due to the nature of high-frequency electromagnetic fields. In this study, we used a lens antenna. Power intensity follows a Gaussian distribution, with strong intensity at the center focal point and weaker intensity at the periphery due to lens antenna characteristics. Therefore, damage from strong incident power appears from the sample center.

When an MTT assay was performed in this state, cell damage occurred locally in the center. However, it could not be captured as a significant change when evaluated by overall absorbance. The standard MTT assay averages results across the entire sample, and effects may be underestimated in non-uniform systems.

For example, in the skin model exposure experiment under standard conditions, we extracted dye from the entire sample and measured absorbance. No clear effect was observed at 250 mW/cm^2, and a clear viability decrease was observed at 500 mW/cm^2. This suggested the threshold exists between these values (Fig. 5). However, stained sample images in Fig. 6 show that lethal damage was clearly observed around the center (the lens antenna focal point) at 250 mW/cm^2. These results demonstrate that averaging the sample before measuring it overestimates the threshold based on cellular damage.

Therefore, we adopted image-based evaluation to determine cell damage thresholds. The three-dimensional tissue model surface was photographed after MTT staining following 48-hour post-culture. Cell damage was judged as “present” when a clearly visible white or pale discolored region appeared in the central area of the tissue model, indicating loss of formazan production due to cell death. This contrasted sharply with the surrounding purple-stained viable tissue. In cases where visual assessment was ambiguous, samples were categorized as “no damage” to ensure conservative threshold estimation. This criterion, similar to that employed in the rabbit study, allowed consistent and reproducible evaluation across all experiments.

Figure 6 shows representative staining images of skin model exposure samples under standard conditions (33°C, 50%RH). The images confirm that no damage occurred at 180 mW/cm^2, but clear damage was observed at 250 mW/cm^2. This phenomenon was consistently observed in all exposure experiments conducted in this study. Considering the presence or absence of such damage and the temperature rise described later, the threshold was determined to be between 180-250 mW/cm^2.

On the other hand, under high-temperature, high-humidity conditions (42.5°C, 80%RH), no cell damage was observed at 130 mW/cm^2, but it was repeatedly observed at 150 mW/cm^2. Figure 7 illustrates typical examples.

Thermal images recorded during the experiments confirmed

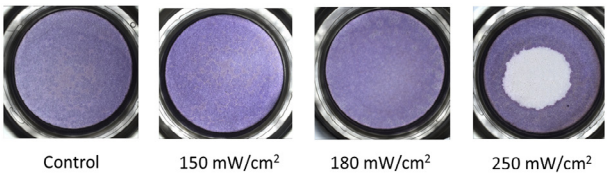

Fig. 6 Representing microscopic image of MTT staining in 3D reconstructed skin model after 6 min. 60 GHz MMW-EMFs exposure in standard condition

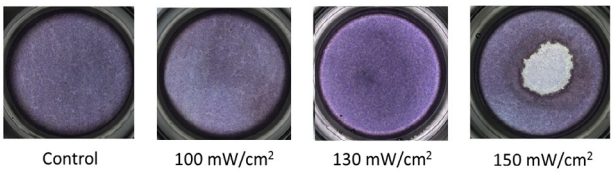

Fig. 7 Representative microscopic image of MTT staining in 3D reconstructed skin model after 6 min. 60 GHz MMW-EMFs exposure in hot and humid conditions

that temperature rises corresponded to incident power density and time elapsed since exposure start. Compared to standard conditions, the starting point temperature was higher under high-temperature, high-humidity conditions. This meant that the time to reach the temperature causing cell damage was shorter, and the time spent at high temperature during the 6-minute exposure period was longer. Therefore, cell viability decreased with exposure at relatively low power density.

3.6 Discussion

We conducted fundamental investigations on cell damage thresholds and other effects from 6-minute exposure to 60 GHz MMW-EMFs in a human three-dimensional reconstructed skin tissue model. From the knowledge obtained in the experiments, we found that the main factor for cell damage was temperature rise correlated with incident power density. Cell damage was observed when temperatures reached approximately 51°C± 1-2°C. Figure 8 shows the incident power density, maximum temperature reached, and temperature rise (Δt) achieved during the experiments.

Regarding environmental effects, damage occurred at lower incident power densities under high-temperature, high-humidity conditions (42.5°C, 80%RH) than under standard conditions (33°C, 50%RH). Cell damage occurred when surface temperatures exceeded approximately 51°C during the exposure period used in this study, rather than when incident power density increased.

This suggests that initial temperature is a major factor. Cell damage depends on both the initial temperature and the extent to which it is elevated by MMW-EMF exposure. Thus, under high-temperature, high-humidity conditions, a lower incident power density is sufficient to induce cellular damage.

These findings suggest that cell damage from millimeter-wave electromagnetic field exposure is primarily caused by heat generated by MMW-EMF energy absorption. In reality, an incident power density that elevate surface temperature reaching approximately 50°C, depending on the environment, can be considered the cell damage threshold.

In comparison with previous rabbit experiments, our results tended to show lower thresholds than those obtained by Kojima et

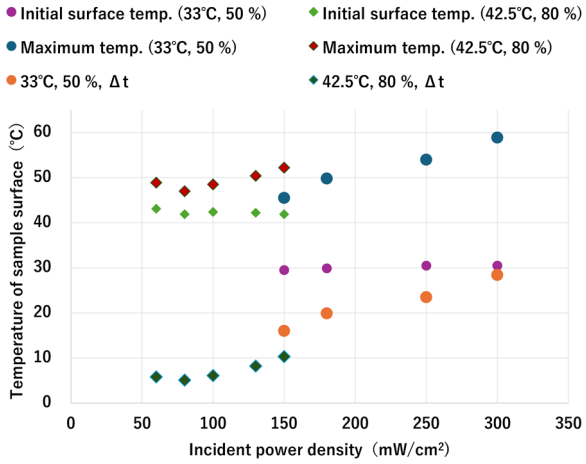

Fig. 8 Relationship between incident power density and surface temperature elevation following 6-minute exposure to MMW-EMFs in a 3D tissue model

al. [12]. An important observation was that thermal elevation was greater at the same incident power density than in the rabbit study. During exposure in the rabbit experiments, active heat transport occurred. Examples include blood flow and tear fluid. Heat dissipation also occurred. In contrast, there is no active heat transport or heat dissipation in the reconstructed skin tissue model, even through the culture medium below it.

Regarding temperature measurement, the thermal camera (FLIR T620) has an accuracy of ±2°C. The emissivity of the tissue model surface was set to 0.95, a typical value for biological tissues. Considering these uncertainties, the observed critical temperature for cell damage (approximately 51°C ± 1–2°C) should be interpreted with an additional uncertainty of about ±2°C due to the measurement system. Nevertheless, the clear correlation between surface temperature and cell damage supports a thermal mechanism as the primary cause of cytotoxicity.

Detailed comparisons are planned for future studies. These include analyses of cell responses such as changes in gene expression.

4. Conclusions

In this study, we conducted research as part of the project "Research on Ocular Injury Thresholds from Radio Wave Exposure under Various Environmental Conditions." This examined thermal effect thresholds and their mechanisms. These serve as the basis for human protection from electromagnetic field exposure.

The millimeter-wave electromagnetic field band is expected to be used for next-generation wireless communication technology which will be introduced in the future.

Specifically, we performed 60 GHz millimeter-wave electromagnetic field exposure experiments on human three-dimensional skin tissue models. We considered various environmental conditions in daily life and the effects that diverse environments may have on biological responses to electromagnetic field exposure.

We conducted experiments on human three-dimensional skin tissue models for 6 minutes. We used standard conditions or high-temperature, high-humidity conditions. These simulate the environmental conditions of corneal surfaces in our research group's previous rabbit study.

Under standard conditions (temperature 33°C, humidity

50%RH), exposure experiments showed that the threshold for cell damage was between an incident power density of 180-250 mW/cm^2. Under high-temperature, high-humidity conditions (temperature 42.5°C, humidity 80%RH), the threshold for cell damage was between 130-150 mW/cm^2.

These values are several tens to approximately 100 times higher than the local absorption guideline standard value for general environments (2 mW/cm^2) in Japan's Radio Radiation Protection Guidelines. This suggests that equipment operated according to current regulations has sufficient margin for protection against thermal effects from radio wave exposure.

Furthermore, the observed effect is only thermal damage. Under conditions where cell damage occurred, the maximum cell surface temperature reached approximately 50°C. Therefore, under the 6-minute exposure condition, our data show that the threshold for cell damage is the incident power density that reaches this temperature.

In this study, we focused on thermal effects. These serve as the basis for protecting the human body from radio wave exposure. We conducted investigations using a human three-dimensional tissue model regarding cell damage.

Future investigations should focus on whether non-thermal effects exist. This will address social anxiety and enable secure and safe radio wave use.

Acknowledgment

The authors would like to express their sincere gratitude to Sachi Matsumoto of TESS Co., Assistant Professor Toshio Kamijo and Research Assistant Aki Hada of Tokyo Metropolitan University, and Associate Professor Takafumi Tasaki and Professor Masami Kojima of Kanazawa Medical University for their guidance and advice.

This research was conducted under the project by Ministry of Internal Affairs and Communications (JPMI10001), Japan.

References

[1] Wertheimer N, Leeper E., Electrical wiring configurations and childhood cancer. Am J Epidemiol. 1979 Mar;109(3):273-284. doi: 10.1093/oxfordjournals.aje.a112681.

[2] Takashima, Y., Miyakoshi, J., et al., Genotoxic Effects of Strong Static Magnetic Fields in DNA-Repair Defective Mutants of Drosophi-la melanogaster, J Radiat. Res., 45, (2004), 393-397.

[3] Takashima, Y., Ikehata, M., et al., Inhibition of UV-induced G1 arrest by exposure to 50 Hz magnetic fields in repair-proficient and -deficient yeast strains, Int J Radiat Biol., 79, (2003) 919-924.

[4] Nakasono, S., Ikehata, M., et al., Intermediate frequency magnetic fields do not have mutagenic, co-mutagenic or gene conversion potentials in microbial genotoxicity tests, Mut. Res., 649, (2008), 187-200.

[5] Yoshie, S., Ogasawara, Y., et al., Evaluation of biological effects of intermediate frequency magnetic field on differentiation of embryonic stem cell, Toxicology Reports, Volume 3, 2016, Pages 135-140.

[6] Ikehata. M., Suzuki, Y., et al., "An Approach for Evaluation of Biological Effects of Complex Magnetic Fields with Various Frequency Components in Electric Train," *RTRI Report*, Vol. 20, No. 1, pp. 35-40, 2006 (in Japanese).

[7] Kawasaki, K., Nakamura, K., "Trend of the Development of Millimeter Wave Technology for Railway Application," *RTRI Report*, Vol. 30, No. 1, pp. 51-54, 2016 (in Japanese).

[8] Ministry of International Affairs and Communications, Radio Radiation Protection Guidelines, Revised September 12, 2018.

[9] International Commission on Non-Ionizing Radiation Protection (ICNIRP). Guidelines for Limiting Exposure to Electromagnetic Fields (100 kHz to 300 GHz). Health Phys. 2020 May;118(5):483-524. doi: 10.1097/HP.0000000000001210. PMID: 32167495.

[10] "IEEE Standard for Safety Levels with Respect to Human Exposure to Electric, Magnetic, and Electromagnetic Fields, 0 Hz to 300 GHz - Corrigenda 2," in IEEE Std C95.1-2019/Cor2-2020 (Corrigenda to IEEE Std C95.1-2019) , pp. 1-15, 21 Oct. 2020, doi: 10.1109/IEEESTD.2020.9238523.

[11] Kojima, M., Suzuki, Y., Sasaki, K. et al. Ocular Effects of Exposure to 40, 75, and 95 GHz Millimeter Waves. J Infrared Milli Terahz Waves 39, 912-925 (2018). https://doi.org/10.1007/s10762-018-0497-z.

[12] Kojima, M., Tasaki, T., Suzuki, Y. et al. Threshold for Millimeter-Wave (60 GHz)-Induced Ocular Injury. J Infrared Milli Terahz Waves 43, 260-271 (2022). https://doi.org/10.1007/s10762-022-00850-w.

[13] OECD (2019), Test No. 431: In vitro skin corrosion: reconstructed human epidermis (RHE) test method, OECD

Authors

Masateru IKEHATA, Ph.D.
Manager, Comfort Science and Technology Laboratory, Human Science Division
Research Areas: Genotoxicity, Bioelectromagnetics, Occupational Hygiene

Yukihisa SUZUKI, Ph.D.
Professor, Tokyo Metropolitan University
Research Areas: Electromagnetic Theory, Bioelectromagnetics, Large-scale Numerical Simulation

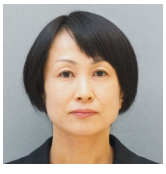

Sachiko YOSHIE, Ph.D.
Senior Researcher, Comfort Science and Technology Laboratory, Human Science Division
Research Areas: Molecular Biology, Microbiology, Bioelectromagnetics

Hiroshi SASAKI, M.D., Ph.D.
Professor, Kanazawa Medical University
Research Areas: Ophthalmology

Experimental Analysis of Mechanism of Steady State Caused by Extreme Earthquakes and Development of an Effective Stress Analysis Method for Sandy Soil

Tomoya ONODERA **Ryuichi IBUKI** **Jun IZAWA**
Soil Dynamics and Earthquake Engineering Laboratory, Center for Railway Earthquake Engineering Research

Kiyoshi FUKUTAKE
Ohsaki Research Institute

Takatoshi KIRIYAMA
Shimizu Corporation

Souichi MABUCHI **Tsuyoshi KODAMA**
Itochu Techno-Solutions Corporation

When designing railway structures to withstand extreme earthquake motion, it is necessary to evaluate the response of the ground using effective stress analysis. It is known that the "steady state" occurs during large soil deformation. In this steady state, shear strain increases while stress remains constant. Few studies to date have examined the steady state mechanism under actual ground conditions. This study examines the behavior of sandy soil under large deformation conditions using elemental tests with Toyoura sand. An effective stress analysis method which can reproduce the steady state behavior is then proposed.

Key words**:** *extreme earthquake, liquefaction, steady state, effective stress analysis, extended Bowl model*

1. Introduction

In the Design Standards for Railway Structures and Commentary (Seismic Design) [1], hereinafter referred to as the "Seismic Standards," the maximum expected ground motion at the construction site of a structure is defined as L2 seismic motion. In particular, in areas where seismic motion exceeding standard L2 seismic motion can occur, it is necessary to estimate site-specific seismic motion using strong ground motion prediction methods. Near the source region, extremely large seismic motion may be calculated. In fact, during the 2024 Noto Peninsula Earthquake (Magnitude 7.6), ground surface motion exceeding 2,000 Gal was recorded [2].

When examining liquefaction behavior during massive earthquakes, there is a possibility that even relatively dense ground may liquefy, or a phenomenon known as steady state may occur, in which shear deformation progresses at a constant shear stress. As will be discussed later, the occurrence of steady state significantly affects the acceleration and displacement responses of liquefied layers. Therefore, in the design of railway structures, it is necessary to calculate the seismic response accurately by taking the steady state into account.

This study aims to understand the behavior of liquefied ground during massive earthquakes through various laboratory tests, including hybrid ground response tests, and to develop an effective stress analysis method capable of evaluating such behavior. This report discusses the mechanism of steady state in Chapter 2, presents the results of the laboratory tests conducted to understand this phenomenon in Chapter 3, and outlines the developed effective stress analysis method and its validation results in Chapter 4.

2. Steady state of sandy soil

2.1 Steady state due to soil critical state

Yoshimine and Ishihara (1998) [3] organized the conditions under which sand reaches a steady state at different levels of effective stress depending on its initial density, where shear strain progresses while shear stress remains constant. This phenomenon occurs when sand reaches what is known as the critical state. Figure 1(a) schematically illustrates the deformation behavior of saturated sand until it reaches the critical state. Under drained conditions, loose sand with a high void ratio undergoes volumetric compression, while dense sand expands volumetrically. Finally, regardless of the initial void ratio, the sand converges to a constant void ratio. This state, in which shear deformation progresses without any change in volume, is defined as the critical state of soil, and the void ratio at this point is referred to as the critical void ratio, e_{cr}.

Conversely, under undrained conditions, where volume change does not occur, loose sand undergoes a reduction in effective stress, while dense sand recovers its effective stress. Eventually, shear deformation progresses while effective stress remains constant. Although this is the critical state under undrained conditions, it is commonly referred to as the steady state. The effective stress at which sand reaches a steady state, denoted as σ'_s, is determined by the initial void ratio e_0. Figure 1(b) shows sand behaviors in undrained conditions, which correspond to seismic behavior, until it reaches a steady state. It is known that loose sand softens while dense sand hardens as they reach steady state, both of which occur along a straight line on the shear stress-effective stress plane, known as the critical state line. Furthermore, it is also known that the critical state line shown on the e-logσ' plane is parallel to the normal consolidation line (Fig. 1(c)). This phenomenon is referred to as "steady state due to critical state," and identifying the critical state line is necessary in order to determine the void ratio and effective stress at that time.

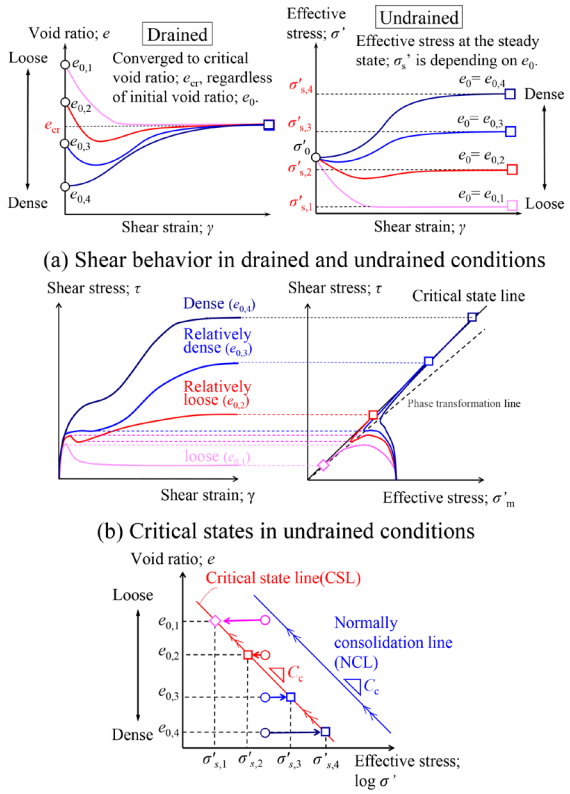

(a) Shear behavior in drained and undrained conditions

(b) Critical states in undrained conditions

(c) Behavior on *e*-logσ' plane

Fig. 1 Conceptual diagram of soil deformation behavior under monotonic shear

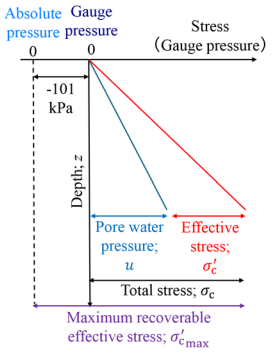

Fig. 2 Conceptual diagram of negative pressure limit

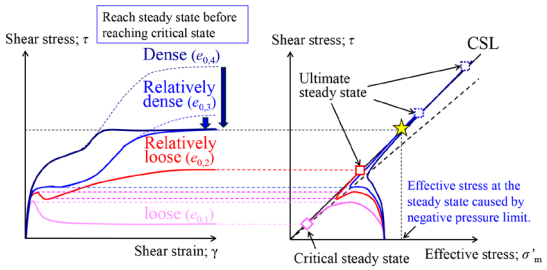

Fig. 3 Soil behavior leading to steady state; considering negative pressure limit

2.2 Steady state due to negative pore water pressure

When dense sand is sheared under undrained conditions, the pore water pressure may reach negative pressure. This negative pressure has a lower limit, and it is possible that the steady state may be reached due to this limit before the sand reaches the critical state. Figure 2 schematically illustrates the stress conditions within saturated ground. It is common to express ground stress using gauge pressure relative to atmospheric pressure. A gauge pressure of 0 kPa corresponds to an absolute pressure of approximately 101 kPa. When the ground undergoes cyclic shear during an earthquake, the pore water pressure increases and the effective stress decreases, leading to liquefaction. However, in the case of dense sand, cyclic mobility causes a decrease in the pore water pressure and recovery of the effective stress. In this process, although the pore water pressure may drop to negative values, it cannot fall below 0 kPa absolute pressure (approximately −101 kPa gauge pressure). Therefore, the upper limit of the recoverable effective stress, σ'_{max}, is given by:

$$\sigma'_{max} = u + \sigma'_c + 101 = \sigma_c + 101 \,(\mathrm{kPa}) \quad (1)$$

where u is the pore water pressure and σ_c is the total stress. In element tests and model experiments, the pore water pressure u often does not reach a gauge pressure of −101 kPa but rather bottoms out at around −40 to −80 kPa, due to the characteristics of the testing apparatus. This phenomenon, where steady state behavior occurs due to the bottoming out of pore water pressure, is referred to as steady state due to “negative pressure limit” in this report. In ground conditions where the critical state is reached under high effective stress and shear stress, considering the negative pressure limit suggests that the steady state may occur at lower stress levels, as shown in Fig. 3. Therefore, to accurately evaluate the conditions under which the steady state occurs in actual ground, it is necessary to assess the contributing factors in relation to pore water pressure conditions.

3. Laboratory testing on steady state

The previous chapter discussed the principles behind the occurrence of the steady state of sand. This chapter presents the results of laboratory soil tests conducted to verify this phenomenon. In this study, the following tests were carried out: undrained monotonic shear tests to confirm the occurrence of steady state behavior; an isotropic triaxial consolidation test to determine the critical state line, which is considered to represent the condition where sand reaches a steady state; and, hybrid ground response tests [4], which combine ground response analysis with element testing to accurately reproduce the seismic behavior of the ground.

3.1 Undrained monotonic shear test

To confirm the steady state behavior of sand, undrained monotonic shear tests were carried out on *Toyoura* sand using a hollow cylindrical torsional shear apparatus up to large strain levels. The test conditions are shown in Table 1. In order to verify steady state

Table 1 Conditions for undrained monotonic shear test

Soil sample	*Toyoura* sand				
Relative density; D_r (%)	10	40	60	80	90
Initial effective confining pressure; σ'_c (kPa)	50	100	100	100	100
Back pressure (kPa)	100	200, 500	200, 500	200	200

behavior caused by two mechanisms, critical state and negative pressure limit, multiple tests were carried out on specimens with varying relative densities and back pressure conditions. In this case, the back pressure corresponds to the initial pore water pressure under actual ground conditions. Under typical back pressure conditions (approximately 200 kPa), steady state behavior was observed due to the negative pressure limit being reached before the critical state was attained. Therefore, additional tests were carried out under a high back pressure condition of 500 kPa to confirm that steady state behavior occurred because the critical state had been reached. Figure 4 shows representative results from the tests, including shear stress vs. shear strain relationships, effective stress paths, and pore water pressure vs. shear strain relationships. In the cases with D_r = 40% and 60% under 200 kPa back pressure, the steady state was reached at an effective stress of approximately 340 kPa, despite differences in density. In the case with 500 kPa back pressure (indicated by dashed lines), the same density reached a higher effective stress, suggesting that the 200 kPa cases reached the steady state due to the negative pressure limit. Furthermore, in the case with D_r = 60% and 500 kPa back pressure, the effective stress at the steady state was approximately 640 kPa. This is 300 kPa higher than in the BP = 200 kPa case and indicates that the steady state was also reached due to the negative pressure limit. In all these cases, pore water pressure bottomed out at around −40 kPa, suggesting that the lower limit of negative pressure in the hollow cylindrical torsional shear apparatus used in this study was also around −40 kPa. Similar steady state behavior due to the negative pressure limit was also observed in the cases with D_r = 80% and 90%.

On the other hand, in the case with Dr = 40% and 500 kPa back pressure, as indicated by the red dashed line, the steady state occurred under conditions where the effective stress was lower than the total stress +40 kPa and the pore water pressure was higher than −40 kPa. This suggests that the steady state was reached due to the ultimate steady state of the soil. In the case with D_r = 10%, the steady state was reached as the effective stress continued to decrease, indicating that the behavior corresponds to the critical steady state of the soil. Additionally, in the cases with D_r = 40% and 60%, differences in behavior prior to reaching steady state were observed depending on the back pressure conditions. However, the cause of these differences remains unclear and is considered a subject for future investigation.

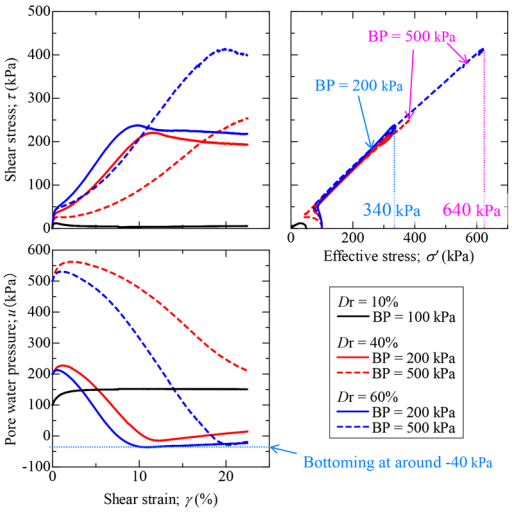

Fig. 4 Undrained monotonic shear test results

3.2 Triaxial isotropic compression test

Considering that the critical state line is generally parallel to the normal consolidation line [5], the authors determined the normal consolidation line through an isotropic triaxial consolidation test and then derived the critical state line based on the result. The test conditions are shown in Table 2. A triaxial test apparatus was used to perform isotropic consolidation over a wide range of stress levels, from 20 to 3,000 kPa. The test results are shown in Fig. 5. The dashed lines represent the compression and swelling curves, obtained by applying the least squares method to the plots from the following loading and unloading sequences: Loading from 20 to 1,000 kPa, loading from 1,000 to 3,000 kPa, and unloading from 3,000 to 100 kPa. Up to a consolidation stress of approximately 1,000 kPa, the compression behavior followed a slope equivalent to the swelling curve (C_s). Beyond this stress level, the slope became steeper, corresponding to the normal consolidation line (C_c).

The results of the consolidation tests and the effective stress and void ratio at the point of steady state observed in the monotonic shear tests were plotted in Fig. 6. The straight line passing through

Table 2 Conditions for triaxial isotropic consolidation test

Specimen	*Toyoura* sand 50×100 mm cylindrical specimen
Initial relative density	D_r = 19.6%
Initial stress condition	Effective confining pressure; 20 kPa Back pressure; 200 kPa
Loading	20 → 3,000 kPa (11 steps)
Unloading	3,000 → 100 kPa (5 steps)

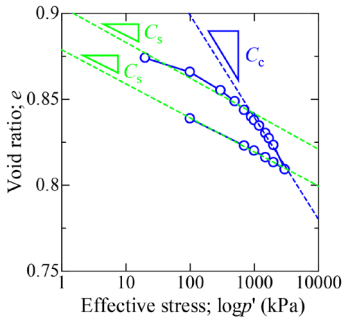

Fig. 5 Results of triaxial isotropic consolidation tests on *Toyoura* sand

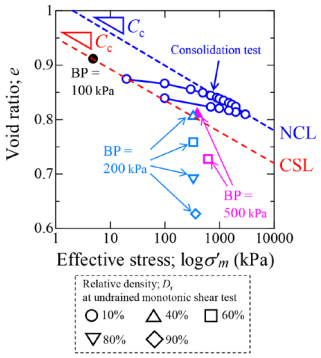

Fig. 6 *e-logσ′m* relationship concerning limit state of *Toyoura* sand

the steady state points of the D_r = 40%, back pressure 500 kPa and D_r = 10%, back pressure 100 kPa cases, which are considered to have reached their steady states due to the critical state of the soil, is nearly parallel to the normal consolidation line obtained from the isotropic consolidation test. This line is therefore regarded as the critical state line for *Toyoura* sand. From this, it can be concluded that to determine the critical state line in practice, it is sufficient to conduct an isotropic consolidation test and a single undrained monotonic shear test under low-density conditions that are likely to reach the critical state. All other cases, including those with D_r = 80% and 90%, were plotted below the critical state line. In cases with a back pressure of 200 kPa, the steady state was reached at an effective stress of approximately 340 kPa. In the cases with a back pressure of 500 kPa, the steady state was reached at approximately 640 kPa. In both cases, the effective stresses of the steady states are around initial total stresses plus 40 kPa. Regardless of the initial density of the sand, the effective stress at a steady state was determined solely by the back pressure condition, confirming that in these cases the steady state occurred because of the negative pressure limit.

3.3 Hybrid ground response analysis

To investigate the seismic behavior of saturated sand layers within stratified ground and to confirm the occurrence of the steady state phenomena, a hybrid ground response test was conducted [6]. This testing apparatus enables the ground response to be evaluated precisely by replacing the target layer in a one-dimensional ground response analysis with a simple shear element test with static loading.

The test was conducted on the ground model shown in Fig. 7. The sand layer located at a depth of 4 to 6 meters was replaced with *Toyoura* sand at D_r = 60% for a simple shear test, while the other layers were modeled using the GHE-S model for total stress analysis with standard parameters [1]. Assuming the groundwater level is at the ground surface, the hydrostatic pressure at a depth of 5 meters is approximately 50 kPa. Two test cases were conducted by setting the back pressure to 50 kPa and 200 kPa, resulting in different negative pressure limits. Although the back pressures differed, the initial average effective stress was adjusted to 20 kPa in both cases by adjusting the cell pressure. Preliminary tests confirmed that the lower limit of negative pressure in this apparatus is approximately −80 kPa. Thereby, the effective stress at the steady state due to the negative pressure limit is estimated to be approximately (1) 150 kPa and (2) 300 kPa, respectively. According to Fig. 6, for *Toyoura* sand at D_r = 60%, the effective stress at the steady state exceeds 1,000 kPa as it has reached the critical state, suggesting that the steady state was achieved in both cases because of the negative pressure limit. To observe the ground behavior including the steady state during an extreme earthquake, the input seismic motion was adjusted to a maximum amplitude of 5,000 Gal, based on the L2 seismic motion spectrum II (G1) described in the Seismic Standards (Fig. 8). This input motion was applied to the base layer through a viscous boundary with parameters ρ = 2.0 g/cm^3 and V_s = 400 m/s. Rayleigh damping was applied with coefficients α = 3.78 and $\beta = 4.53 \times 10^{-4}$.

Figure 9(a) shows the surface response acceleration and the stress-strain behavior of the tested layer. In Case (1) with a back pressure of 50 kPa, the effective stress reached 150 kPa (the steady state effective stress due to the negative pressure limit,) at around six sec-

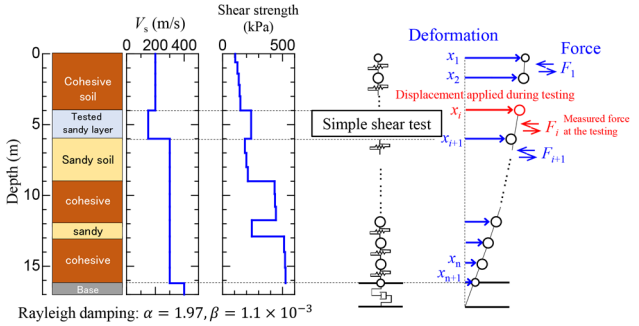

Fig. 7 Ground model for hybrid ground response test

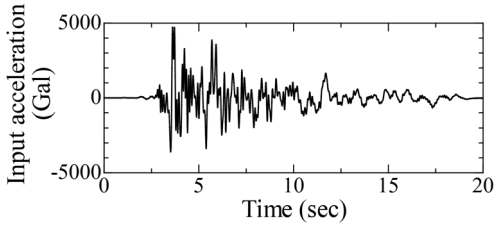

Fig. 8 Input seismic wave

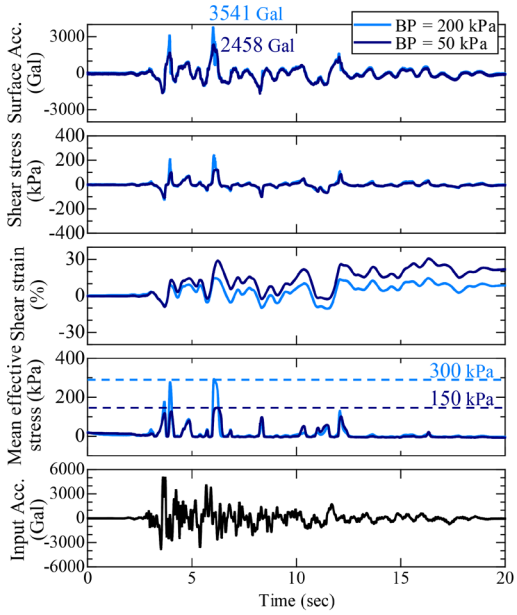

(a) Time histories

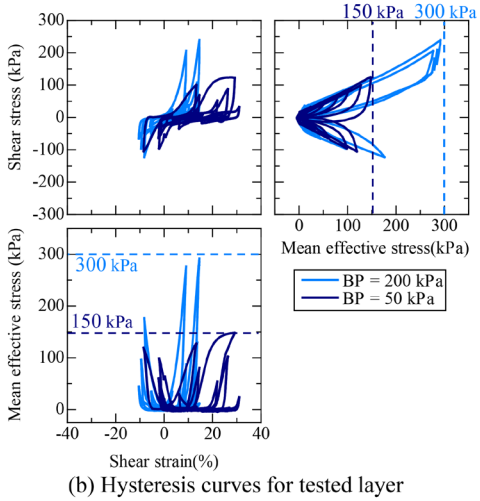

(b) Hysteresis curves for tested layer

Fig. 9 Hybrid ground response test results

onds, after which both the effective stress and shear stress plateaued. In contrast, in Case (2) with a back pressure of 200 kPa, the effective stress increased to approximately 290 kPa, approaching the steady state effective stress of 300 kPa due to the negative pressure limit, but did not reach it. At this point, the surface response acceleration was 2,458 Gal in Case (1) and 3,541 Gal in Case (2), indicating that the maximum response acceleration varied depending on the back pressure condition. Additionally, the shear strain in Case (2) (BP = 200 kPa) was about half that of Case (1) (BP = 50 kPa). Figure 9(b) shows the shear stress-shear strain relationship and the effective stress path of the hybrid test layer. In Case (1) with a back pressure of 50 kPa, steady state was reached, and the shear stress plateaued, while the shear strain increased under constant stress.

From the results above, in evaluating ground response to extreme earthquakes during which the steady state may occur, it is essential to appropriately take pore water pressure conditions into account. Furthermore, to accurately reproduce such behavior through numerical simulation, it is necessary to conduct dynamic analysis with properly defined effective stress at steady state.

4. Effective stress analysis model

In the previous chapter, the behavior of sand under large deformation was confirmed through various tests. On the basis of these findings, this chapter discusses an effective stress analysis model capable of evaluating such behavior.

4.1 Previous models for effective stress analysis

When conducting a dynamic analysis on ground where liquefaction may occur, it is recommended that an effective stress analysis method is used which can account for the effects of rising pore water pressure. In the Seismic Standards [1], the GHE-S model is adopted as the standard total stress analysis model. This model is a modified version of the GHE model, and is designed to account for the phenomenon where, due to cyclic mobility, the shear stress-shear strain relationship in the large strain region exhibits a reverse S-shape, resulting in a decrease in hysteretic damping. In effective stress analysis, such phenomena can be automatically considered. Therefore, the GHE model is combined with the "Bowl model [7]," a dilatancy model that evaluates pore water pressure, to perform effective stress analysis.

The Bowl model expresses the dilatancy ε_v^s that occurs during shear of soil as the sum of compressive and expansive components (2), as illustrated in Fig. 10. By applying undrained conditions (3), the generation of pore water pressure can be modeled.

$$\varepsilon_v^s = A\cdot\Gamma^B + \frac{G^*}{C+D\cdot G^*} \tag{2}$$

$$d\sigma_m' = \frac{-\sigma_m'\cdot d\varepsilon_v^s}{0.434\left(C_s \text{ or } C_s'\right)/(1+e_0)} \tag{3}$$

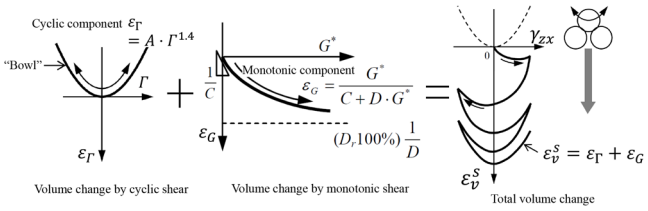

Fig. 10 Conceptual diagrams of Bowl model (Add to [7])

Here, Γ is total shear strain, G^* is cumulative shear strain, and A, B, C, D, $C_s/(1+e_0)$, $C'_s/(1+e_0)$ are parameters of the Bowl model.

4.2 Extended Bowl model

4.2.1 Modeling of steady state

In the "conventional" Bowl model, the swelling component $A\cdot\Gamma^B$ continues to increase with strain. This makes it unable to account for steady state behavior, and can lead to the effective stress being overestimated under large deformation conditions. To address this problem, the "extended Bowl model" was developed [8]. This model considers the steady state by shifting the bowl horizontally when the void ratio reaches the critical void ratio (e_{cr}), setting the increment of void ratio to zero (Fig. 11). This ensures accurate calculation of shear stress and response acceleration in the large strain domain, avoiding overestimation and allowing for precise reproduction of liquefied ground response during extreme earthquakes.

Furthermore, using the results presented in Chapter 3, the model was improved to also account for steady state due to the negative pressure limit. Utilizing the correspondence between the critical void ratio (e_{cr}) under drained conditions and the effective stress at steady state (σ_{cr}') under undrained conditions (as shown in Fig. 1 and (4)), the model was modified so that σ_{cr}' could be specified directly as the steady state threshold instead of e_{cr}. This enables the model to reproduce behavior in which, once the effective stress reaches σ_{cr}', it no longer increases, and shear strain continues to develop under constant stress.

4.2.2 Setting effective stress at the steady state

When employing the extended Bowl model, it is necessary to define not only the parameters of the conventional Bowl model but also additional parameters that govern steady state behavior, specifically, the critical void ratio (e_{cr}) or the effective stress at steady state (σ_{cr}'). This section describes the method for setting σ_{cr}', using the laboratory test results presented in the previous chapter. First, an isotropic triaxial consolidation test is conducted up to high pressure levels to determine the normal consolidation line of the target soil, as shown in Fig. 12 by blue dashed line. Secondly, an undrained monotonic shear test is performed under low-density conditions that are likely to reach the critical state, and the effective stress and void ratio at the point of steady state are obtained. From these two tests, the critical state line of the target soil can be determined, as illustrated in Fig. 12 by the red dashed line. Meanwhile, using the hydrostatic pressure at the depth of interest in the analysis, the effective stress at the steady state due to the negative pressure limit can be estimated, shown as the purple dashed line in Fig. 12. To determine the effective stress at steady state, it is first necessary to specify the initial condition of the target soil layer on the e-logσ' plane (e.g., the trian-

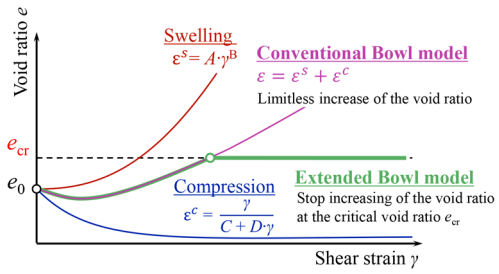

Fig. 11 Conceptual diagram of extended Bowl model

gle symbol in Fig. 12). From this point, a horizontal line representing constant volume shear should be traced. The steady state is then considered to occur at the point where either the critical state line or the negative pressure limit line is reached first (e.g., star symbol in Fig. 12). The effective stress at this point is taken as the effective stress at steady state, σ_{cr}'.

When performing effective stress analysis using the extended Bowl model, σ_{cr}' should be set for each layer using the procedure above, enabling dynamic analysis that accounts for steady state behavior.

4.3 Reproduction analysis of laboratory tests

4.3.1 Parameter fitting and reproduction of liquefaction test

Using the extended Bowl model, a reproduction analysis of the undrained cyclic shear test performed on *Toyoura* sand with D_r = 60% was conducted, using a hollow cylindrical torsional shear test apparatus. The parameters used in the analysis were derived from deformation property tests and liquefaction strength tests, and are shown in Table 3: for the meaning of parameters (b) and (c), refer to references [1] and [7]. Note that the Bowl model parameters $C_s/(1+e_0)$ and $C'_s/(1+e_0)$ are adjustment parameters related to strain development, and do not correspond to the compression index obtained from a consolidation test.

The simulation results of the cyclic test using the parameters in Table 3 are shown in Fig. 13. They generally reproduce the liquefaction strength curve, which shows the relationship between the number of cycles to reach γ_{DA} = 7.5% and the shear stress ratio obtained from the test. The effective stress at steady state was set to 150 kPa to match the difference between an initial total stress (70 kPa) and the negative pressure limit of the apparatus (−80 kPa), in order to reproduce the hybrid ground response test.

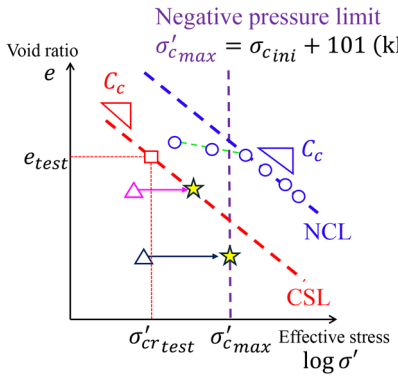

Fig. 12 Conceptual diagram of effective stress setting at steady state

Table 3 Parameters for *Toyoura* sand D_r = 60% analysis

(a) Soil properties

Initial shear stiffness G_{0i} (kPa)	Standard strain γ_{ri} (%)	Internal friction angle ϕ'(°)	Cohesion c(kPa)
9820	0.00732	35.7	0

(b) GHE parameters

$C_1(0)$	$C_1(\infty)$	$C_2(0)$	$C_2(\infty)$	α	β	h_{max}	κ
1.00	0.265	0.424	1.00	1.32	0.97	0.36	1.1

(c) Bowl model parameters

A	B	C	D	$C_s/(1+e_0)$	$C'_s/(1+e_0)$	X_1	σ'_{cr} (kPa)
−0.5	1.4	10.0	30.0	0.01	0.0102	0.15	150

4.3.2 Three-cycles undrained cyclic test

An undrained three-cycle shear test in the ±20% strain range was conducted using a simple test apparatus, and a reproduction analysis was performed with the extended Bowl model. The relationships between shear stress-shear strain and average effective stress-shear strain are shown in Fig. 14. The test was conducted using *Toyoura* sand specimens with D_r = 60%, under initial confining pressure conditions of 20 kPa and back pressure conditions of 200 kPa.

In the effective stress analysis employing the extended Bowl model, the average effective stress plateaued at approximately 320 kPa and the shear stress at around 230 kPa in the high strain level. This successfully reproduced the steady state behavior observed in the test. It should be noted that the loop shape at small strain levels differed somewhat from the test results.

4.3.3 Hybrid ground response test

The results of the reproduction analysis for the hybrid ground response test under BP = 50 kPa are shown in Fig. 15, with a comparison between cases applying the extended Bowl model which

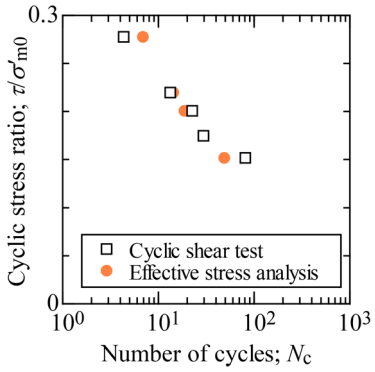

Fig. 13 Reproduced results of liquefaction tests

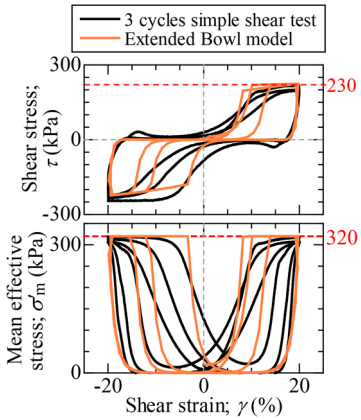

Fig. 14 Reproduction analysis of three-cycles shear test

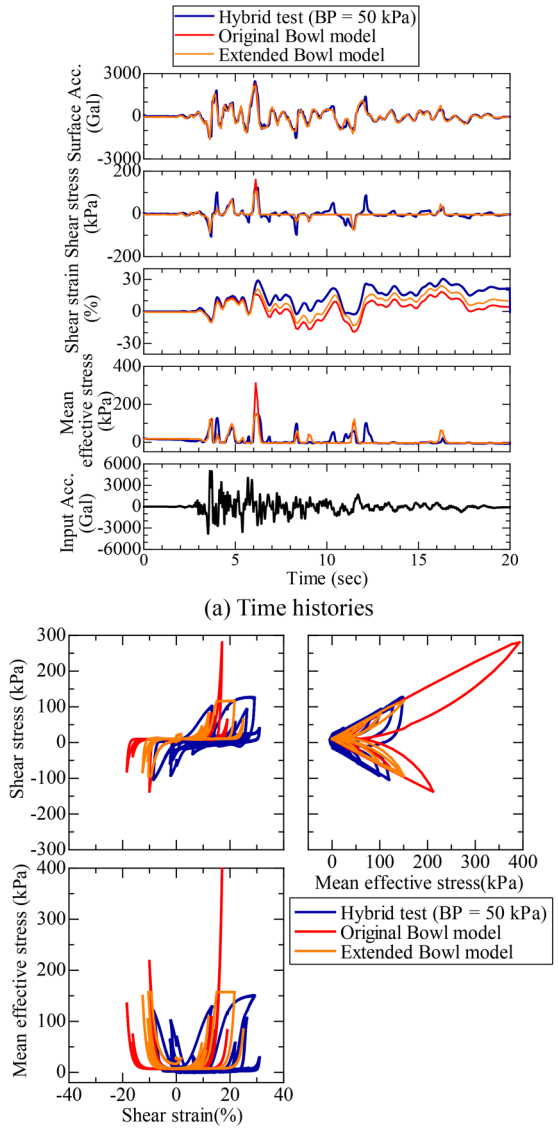

(a) Time histories

(b) Hysteresis curves for tested layer

Fig. 15 Reproduction analysis of hybrid ground response test (Back pressure = 50 kPa)

considers steady state, and the conventional Bowl model which does not. Looking at the time history illustrated in Fig. 15(a), the conventional Bowl model failed to reproduce the plateauing of the stress level after around six seconds. In other words, the average effective stress increased up to 300 kPa and the shear stress to 250 kPa. This resulted in the maximum acceleration at the ground surface being overestimated by up to approximately 3,000 Gal. Conversely, the extended Bowl model reproduced the behavior observed in the hybrid test, where the average effective stress plateaued at approximately 150 kPa. This behavior in shear stress and acceleration response time histories also matched the experimental result.

As can be seen in Fig. 15(b), the conventional Bowl model produced hysteresis curves that overestimated the stress level and underestimated the maximum strain level compared with the test results. In contrast, the extended Bowl model produced hysteresis curves and maximum stress and strain values that were generally consistent with the experimental data. These findings demonstrated that using the extended Bowl model allows for response analysis that accounts for steady state behavior of the ground, enabling simulations that closely reflect actual ground behavior.

5. Conclusions

This study experimentally investigated the behavior of sand under large deformation and proposed an effective stress analysis model capable of reproducing its behavior. The main findings are as follows:

1. In addition to the critical state of sand, negative pressure limits in pore water pressure can also lead to a steady state. Due to this limit, the steady state may occur at different stress levels depending on back pressure conditions, even when using specimens of the same soil type and density.
2. Through hybrid ground response tests simulating extreme earthquakes, it was confirmed that the steady state caused by negative pressure limits affects ground response characteristics such as acceleration.
3. A method was proposed for estimating the effective stress at the steady state by deriving the critical state line from isotropic consolidation tests up to high pressure and undrained monotonic shear tests under low-density conditions that lead to the critical steady state.
4. An extended Bowl model was proposed as an effective stress analysis model capable of accounting for steady state behavior.
5. The extended Bowl model was effective in analyzing stress, successfully reproduced phenomena such as stress plateauing and hysteresis curve shapes observed in element and hybrid ground response tests. This demonstrates the model's ability to simulate ground behavior realistically.

References

[1] Railway Technical Research Institute, "*Design standard for railway structure and commentary (seismic design)*," Maruzen, 2012 (in Japanese).

[2] National Research Institute for Earth Science and Disaster Resilience, HP: Strong ground motion caused by the Noto Peninsula Earthquake on 2024. 1. 1., https://www.kyoshin.bosai.go.jp/kyoshin/topics/html20240101160813/main_20240101160813.html (View on 2025. 7. 2.) (in Japanese).

[3] Yoshimine, M. and Ishihara, K., "Flow potential of sand during liquefaction," *Soils and Foundations*, Vol. 38, No. 3, pp. 189-198, 1998.

[4] Izawa, J., Toyooka, A., Kojima, K., Murono, Y., and Suzuki, A., Deformation properties of soils for a nonlinear dynamic response analysis, *The 7th International Conference on Earthquake Geotechnical Engineering*, 2019.

[5] N. Schofield and C. P. Wroth, *Critical State Soil Mechanics*, McGraw-Hill Inc., 1968.

[6] Ibuki, R., Onodera, T., Izawa, J., Fukutake, K., Kiriyama, T., Mabuchi, S., and Kodama, T., Hybrid ground response tests for pore water pressure condition affecting to the steady state behavior of sandy soil, *Proc. 59th Japan National Conference on Geotechnical Engineering*, 2024 (in Japanese).

[7] Fukutake, K. and Kiriyama, T., "LEAP-2017 Centrifuge Test Simulation using HiPER, *Model Tests and Numerical Simulations of Liquefaction and Lateral Spreading*," Springer, pp. 461-479, 2018.

[8] Onodera, T., Ibuki, R., Izawa, J., Fukutake, K., Kiriyama, T.,

Mabuchi, S., and Kodama, T., Effective stress analysis method on sandy soil considering steady state caused by huge earthquakes, *44th JSCE Earthquake Engineering Symposium*, 2024. (in Japanese).

Authors

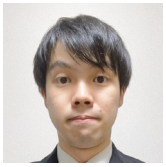

Tomoya ONODERA
Soil Dynamics and Earthquake Engineering Laboratory, Center for Railway Earthquake Engineering Research
Research Areas: Liquefaction, Soil Dynamics

Ryuichi IBUKI
Soil Dynamics and Earthquake Engineering Laboratory, Center for Railway Earthquake Engineering Research
Research Areas: Soil Dynamics, Numerical Simulations

Jun IZAWA, Dr. Eng.
Head of Soil Dynamics and Earthquake Engineering Laboratory, Center for Railway Earthquake Engineering Research
Research Areas: Liquefaction, Soil Dynamics

Kiyoshi FUKUTAKE, Ph.D.
Principal Researcher, Ohsaki Research Institute
Research Areas: Liquefaction, Soil Dynamics

Takatoshi KIRIYAMA, Dr.Eng.
Center for Construction Engineering, Shimizu Corporation Institute of Technology
Research Areas: Liquefaction, Soil Dynamics

Souichi MABUCHI
Science & Engineering Systems Division, Itochu Techno-Solutions Corporation
Research Areas: Numerical Simulations

Tsuyoshi KODAMA
Science & Engineering Systems Division, Itochu Techno-Solutions Corporation
Research Areas: Numerical Simulations

Development of an Inspection Support System Using Tunnel Wall Images

Yudai YAMASHITA **Takashi NAKAYAMA** **Kazuhide YASHIRO**
Tunnel Engineering Laboratory, Structures Technology Division

We developed two systems to improve the efficiency of tunnel inspections. In railway tunnel maintenance, periodic inspections are mandatory. Structural conditions are currently evaluated through visual and hammering inspections. However, these inspections are time-consuming because inspectors must compare paper-based reference documents with the tunnel surfaces under poor lighting conditions. To address these challenges, we first developed an AI-based damage detection and soundness assessment application that automatically identifies surface defects and repair marks in tunnel images and evaluates overall tunnel soundness. Secondly, we developed a mobile projection system that uses red mesh overlays to visualize AI-detected defects on the tunnel lining and indicate critical areas. This paper presents these systems and reports on field validation results demonstrating their effectiveness.

Key words**:** *tunnel, artificial intelligence, inspection, maintenance, projection system*

1. Introduction

Many railway tunnels in Japan, as shown in Fig. 1, were constructed either before World War II or during the period of rapid economic growth. Over the years, systematic inspection cycles and methods have been established. According to the "Maintenance Standards for Railway Structures and Commentary" (hereafter referred to as the "Tunnel Maintenance Standards" [1], a regular inspection known as the "Regular General Inspection" is conducted every two years to identify tunnels exhibiting performance deterioration or potential risks. In addition, a more detailed inspection known as the "Special General Inspection" is conducted at intervals not exceeding 10 years for Shinkansen tunnels and 20 years for non-Shinkansen tunnels. Currently, these inspections—consisting of visual inspections and hammering inspections (Fig. 2)—are conducted on schedule under the supervision of experienced inspectors with sufficient resources, and necessary repairs are carried out accordingly.

However, Japan's railway tunnels span a total length of around 4000 km [2]. With the country facing a declining birthrate and a shrinking labor force [3], streamlining inspection operations has become a pressing challenge. In recent years, the use of digital technologies in tunnel inspections has gained significant attention [4]. The most widely adopted technologies include systems that continuously capture images of tunnel linings to assist in sketching and organizing inspection records [5], as well as AI-based tools that automatically detect cracks from images [6].

However, even with these technologies, identifying and logging tunnel defects other than cracks still relies entirely on manual labor. In addition, during hammering inspections at critical locations using image review results, inspectors often spend a long time locating the exact inspection points inside dark tunnels, as they have to match the actual site with paper-based records.

To address these challenges and improve the efficiency of tunnel inspections further, this study has developed a support system that utilizes tunnel lining images to assist with inspection tasks.

The first component is an application called the "Defect Detection and Soundness Assessment App," which uses AI to identify not only cracks but also other types of damage and repair marks from tunnel lining images. It automatically evaluates the overall structural soundness condition of the tunnel and highlights critical areas that require focused inspection. The second component is a device called the "Critical Area Projection System," which projects red-filled mesh markers directly onto the tunnel lining at key inspection points, helping inspectors quickly locate areas of concern during on-site inspections.

This paper presents details of the developed technologies and reports the results of accuracy verification and their effectiveness.

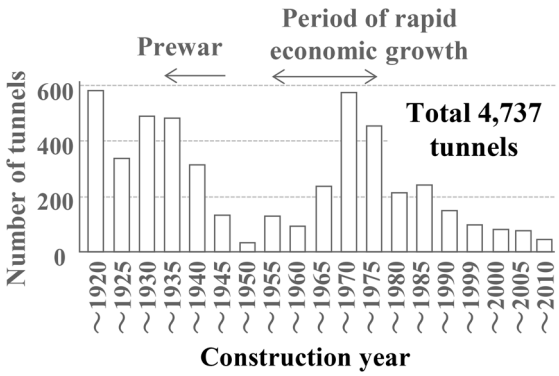

Fig. 1 Construction year and number of railway tunnels

Fig. 2 Hammer sounding inspection along tunnel lining

2. DEFECT DETECTION AND SOUNDNESS ASSESSMENT APP

2.1 Overview

Figure 3 shows an overview of the "Defect Detection and Soundness Assessment App" (hereafter referred to as "the App").

The App runs on a standard personal computer and features a "Defect Detection AI" that automatically identifies defects, such as rust stains and water leakage in captured tunnel images. It also includes a "Soundness Assessment Matrix," developed using typical assessment examples from the Tunnel Maintenance Standards. By comparing detected defects against this matrix, the App automatically displays the most severe condition level as an indicator of structural health for each designated tunnel section.

In general, AI detection technologies demonstrate high accuracy when the target is easily identifiable, as in the case of facial recognition. However, tunnel defects are often overlapping and difficult to distinguish, and assessing structural soundness requires consideration of site-specific factors. As a result, only moderate accuracy was expected. Nevertheless, the current process for detecting non-crack defects relies entirely on manual labor and requires inspectors to invest considerable effort compiling inspection records. Therefore, the App was developed with the belief that even moderate accuracy would provide valuable support to inspectors.

2.2 Defect Detection AI

The AI targets defects that are critical for soundness assessment, including exposed rebar, rust stains, and water leakage. It also detects deposits such as efflorescence and free lime, which may indicate hidden cracks behind the tunnel lining. In addition, the AI is designed to identify common features, including partial lining repairs and drainage pipe installations, which are frequently recorded in inspection logs.

Figure 4 shows an example of defect detection results using the developed AI. To simulate two separate inspections, images representing the "previous inspection" and the "current inspection" were artificially prepared. In Fig. 4(a), the "current inspection" image was further processed to simulate an increase in water leakage compared to the "previous inspection." Figure 4(b) presents the detection results, highlighting defects, including water leakage and deposits, with colored bounding boxes. Figure 4(c) indicates the differences between the "previous inspection" and "current inspection" images, showing the newly detected leakage areas.

The App also allows inspectors to manually add or modify detected defects. For example, Fig. 4(d) shows a manually added bounding box and the result of importing crack data from a CAD file.

To build the Defect Detection AI, we adopted YOLOv5 (You Only Look Once version 5), a convolutional neural network (CNN) that was highly rated at the time of development for its performance

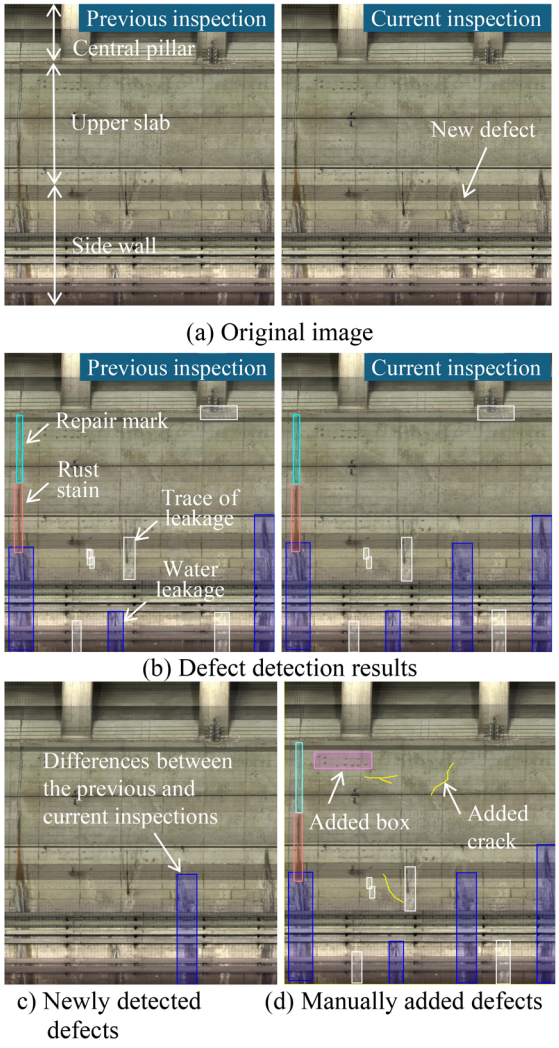

Fig. 4 Examples of defect detection results

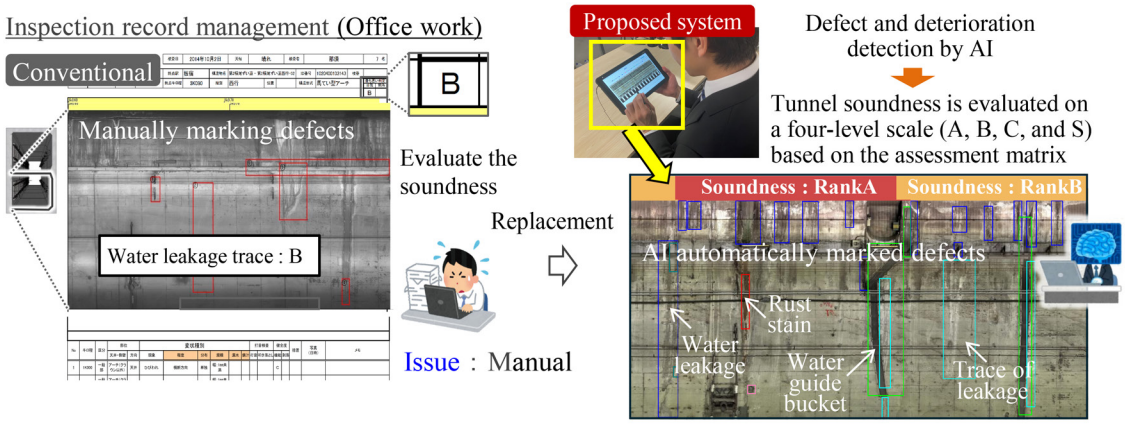

Fig. 3 Overview of deterioration detection and soundness assessment App

on Microsoft's COCO (Common Objects in Context) dataset. YOLOv5 offers four model sizes—s, m, l, and x—based on network complexity. As the model size increases (i.e., more convolutional layers), memory requirements and training time also increase, but detection accuracy tends to improve accordingly.

For training data, we used defect images collected by the Railway Technical Research Institute. Since accurate annotation requires expert knowledge to distinguish between different types of defects, all labeling was performed by tunnel inspection specialists. Because a larger dataset generally leads to higher detection accuracy, we continued to expand the training data even after the system was initially built. In this report, however, we present validation results based on the original dataset used during system development: 512 images of exposed rebar, 2704 of rust stains, 15,684 of water leakage, 5452 of efflorescence, 2774 of partial lining repairs, and 1200 of drainage pipes. All images were augmented through vertical and horizontal flipping.

Figure 5 shows the results of training the model using different YOLOv5 variants and epoch counts (i.e., the number of times the entire dataset was used for training). Figure 5(a) illustrates the relationship between the number of epochs and two key AI performance metrics when using the 's' model: mAP@0.5, which measures the accuracy of object detection predictions, and the F1 score, which reflects the balance between precision and recall. Significant improvements in evaluation metrics, such as mAP@0.5, were observed up to around 500 epochs. Figure 5(b) shows the relationship between model size and performance, indicating that accuracy improves between the 'm' and 'l' models. A visual inspection of the detection results confirmed that the 'x' model, when trained for 500 epochs, achieved the best overall performance on the current training dataset.

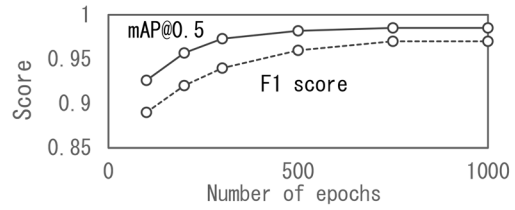

(a) Relationship between the number of epochs, mAP@0.5, and F1 score

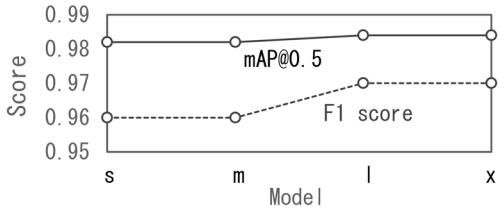

(b) Relationship between the model and mAP@0.5, F1 score

Fig. 5 Evaluation of defect detection accuracy

Table 1 shows the detection accuracy of the AI model when applied to images that were not used during training. The results indicate that the model correctly identified exposed rebar in 90% of cases, and achieved over 95% accuracy for rust stains, water leakage, deposits, repair marks, and drainage pipes.

2.3 Structural soundness assessment matrix

According to the Tunnel Maintenance Standards, structural soundness is classified into several ranks, as shown in Table 2. During general inspections, tunnel conditions are typically categorized into four levels: A, B, C, and S.

For structures rated as soundness rank A, a detailed investigation called an "individual inspection" is conducted to perform a more refined assessment, further classifying them into ranks AA, A1 and A2.

Table 1 Confusion matrix of the constructed model

		Correct answer					
		a	b	c	d	e	f
Detection results	a	0.90					
	b		0.96				
	c			0.98			
	d				0.96		
	e					0.98	
	f						0.97
	–	0.10	0.04	0.02	0.04	0.02	0.03

a: Exposed rebar, b: Rust stain, c: Water leakage
d: Efflorescence, e: Lining repair, f: Drainage pipe
–: Not detected

Table 2 Standard classification of structural soundness

Soundness		Structure State
A		State that threatens operational safety, safety of passengers, public safety, guarantee of regular train operation, or deterioration that might cause this state
	AA	Deterioration that threatens operational safety, safety of passengers, public safety, or the guarantee of regular train operation, and which require emergency countermeasures
	A1	Progressive deterioration that causes the performance of structures to drop, or heavy rain, floods, or earthquakes that might impair the performance of structures
	A2	Deterioration that might cause a future drop in performance of structures
B		Deterioration that might result in a future soundness rank of A
C		Slight deterioration
S		Sound

However, if a defect is found that threatens operational safety, passenger safety, public safety, or the stable operation of trains, it is to be treated as an AA rank issue and immediate action is to be taken.

In this study, we focused on tunnel structural stability which is defined as one of the performance criteria in the Tunnel Maintenance Standards, and conducted condition assessments using a four-level rating (A,B,C,S), assuming the general inspection framework.

Table 3 shows the soundness assessment matrix. This matrix was developed using examples provided in the Tunnel Maintenance Standards, adopting a conservative, safety-focused approach. As previously described, the App uses this matrix to determine the soundness level of each detected defect. The most severe rating within a given section is then assigned as the overall structural soundness rating.

A two-level assessment scheme was defined for rust stains and water leakage based on size and location, referencing examples from the Tunnel Maintenance Standard. In the App, if defects are located above the spring line and the density of defects (i.e. bounding box occupancy) within a single image (tunnel length 10m) along the track direction is high (20% or more), the condition is classified as severe.

Although the Tunnel Maintenance Standard does not provide specific assessment examples for repair marks, the default condition rating for these cases was set to C.

We validated the accuracy of the soundness assessments by comparing them with the ratings recorded in inspection logs maintained by railway operators. The comparison focused solely on the condition levels assigned to the specific types of defects targeted by the detection system. Figure 6 shows how the soundness assessment were validated by comparing them with the railway operator's evaluations across ten station segments. The soundness trends were analyzed using a one-kilometer moving average to facilitate comparison. Although the condition ratings in the inspection logs represent final judgments made after on-site inspections of critical areas, the App demonstrates its ability to capture these trends directly from the tunnel images. On the other hand, as indicated by the asterisks in Fig. 6, there are cases where the App provides fewer conservative judgements, deeming the condition to be sounder than it actually is. These cases reflect site-specific considerations, such as the fact that the damage before repair was quite severe. As a result, the post-repair soundness was not rated as fully restored to level S, but rather kept at levels B or C. These are areas where inspectors are expected to review and adjust the output accordingly.

To conduct this validation, we measured the time required for one person to manually inspect a one-kilometer section of tunnel, both using only manual methods and using the app's automated detection results with manual adjustments. The results showed that while a full manual inspection took about 35 minutes, using the app reduced the time to around one minute, clearly demonstrating its efficiency. Although performance may vary depending on image quality and the number of visible defects, these results demonstrate that the app has shown strong potential as a tool for streamlining inspection work.

3. CRITICAL AREA PROJECTION SYSTEM

3.1 Overview

Figure 7 shows the developed 'Critical Area Projection System' (hereafter referred to as 'the projection system'). As illustrated in Fig. 7(a), the system consists of a projector to display critical areas, a mounting base fixed onto a lightweight trolley, a control PC, and a distance measurement device. As shown in Fig. 7(b), the system can project square mesh diagrams—highlighting critical areas in red—onto precise locations while moving, using data transferred from the defect detection and soundness assessment app.

To accurately project square meshes onto tunnels of various shapes, the mesh diagrams must be geometrically corrected to match the tunnel profile. In this system, the tunnel shape is input using structural drawings, and the distance between the projection device and the tunnel lining is measured. Using this data, an algorithm was developed (Fig. 8) to automatically adjust the mesh diagrams according to the projector's tilt angle and travel distance, ensuring precise projection.

Table 3 Structural condition and standard classification for soundness assessment

	Correct answer				
	Exposed rebar	Rust stain	Water leakage	Water leakage strain Repair mark	No defect
Soundness	A	A～B※	A～B※	C	S

※ Judgement depends on the size and location of defects.

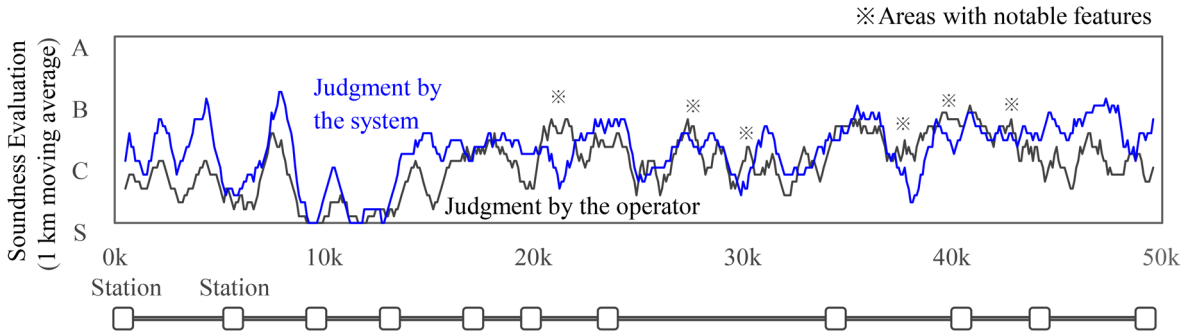

Fig. 6 Verification results of structural soundness assessment

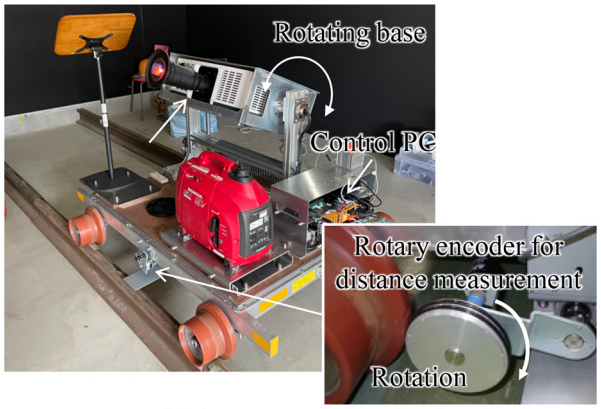

(a) Appearance of projection device

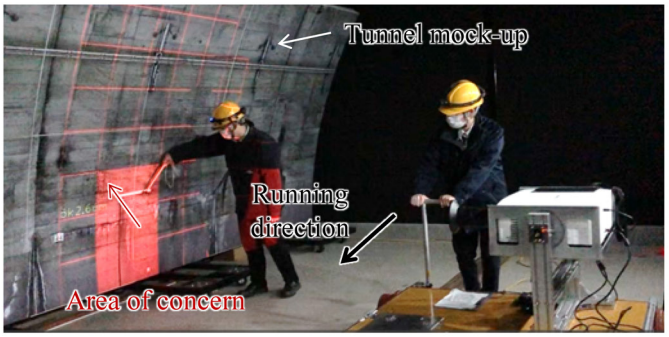

(b) Test projection onto tunnel mock-up

Fig. 7 Overview of device for projecting area of concern

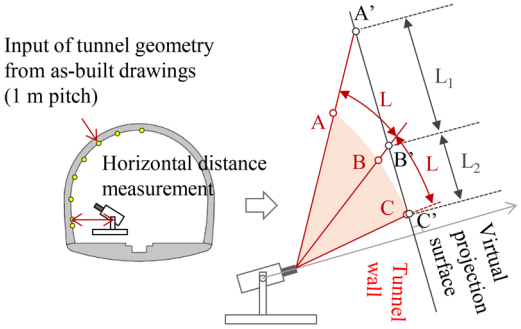

Fig. 8 Mesh correction method

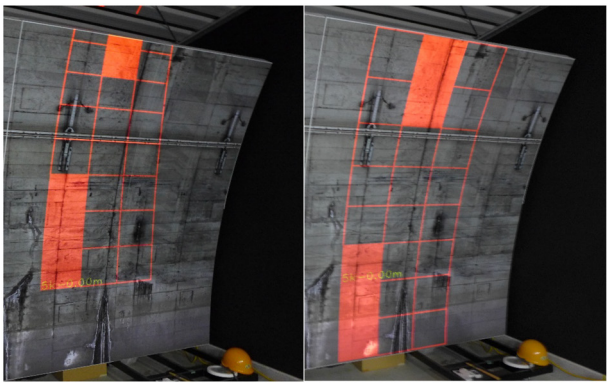

Fig. 9 Difference in projection results due to shape correction

Specifically, to ensure an accurate projection onto the virtual surface shown in Fig. 8, the projector adjusts the output so that points A to C are projected at equal intervals of length L on the tunnel lining. This process involves geometrically correcting the mesh so that the corresponding points A' to C' on the virtual surface are spaced at intervals L_1 and L_2. Figure 9 illustrates the difference with and without shape correction, confirming that the squares are properly projected when the correction is applied.

3.2 Validation using a mock-up

As part of developing the projection system, a one-third scale mock-up made of FRP was constructed in a dark room with adjustable lighting, as shown in Fig. 7(b). This setup was used to select appropriate equipment and to validate the mesh correction algorithm.

Since the validation of the mesh correction algorithm overlaps with the on-site testing described later, this report focuses on the evaluation of the projector's luminous flux required to clearly display critical areas.

The indoor lighting was set to approximately 30 lx to simulate the brightness inside a real tunnel. The projector's luminous flux was then adjusted, and the optimal brightness level for clearly displaying the mesh diagram was determined through visual inspection. Figure 10 shows photographs of the projection conditions along with the corresponding luminous flux values. When the light flux is low, the mesh diagram appears unclear, but as the light flux increases, the diagram becomes noticeably sharper and more visible. From these results, it was determined that a projector with a luminous flux of at least 8000 lm is sufficient for clearly displaying mesh diagrams.

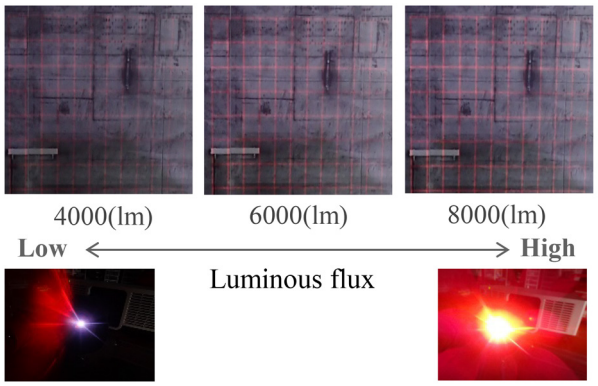

Fig. 10 Verification results of required luminous flux

3.3 Field testing

Using pre-captured images of the tunnel lining provided by the railway operator, defects and critical areas were automatically extracted in advance using AI. The projection system was then brought to the site to verify whether the identified areas could be accurately projected onto the tunnel lining.

To verify projection accuracy across typical tunnel cross-sections—horseshoe-shaped, rectangular, and circular—tests were conducted, as shown in Fig. 11. The photos confirm that the square mesh diagrams were correctly projected on all tunnel shapes.

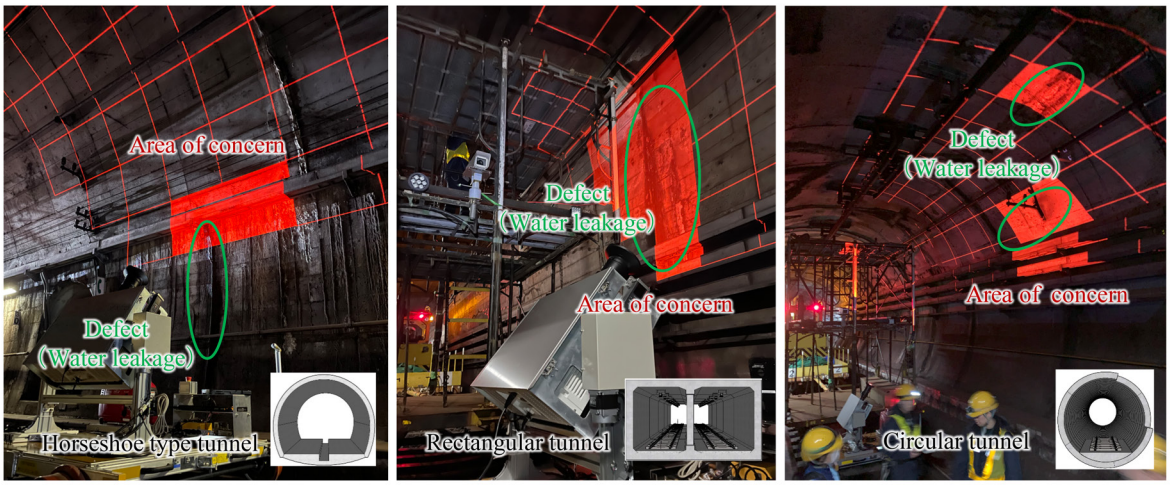

Fig. 11 Projection conditions onto actual tunnels with different shapes

Figure 12 shows a trial of hammering inspection conducted from an elevated work platform. Positioning the projection system slightly away from the platform ensured that the projector's light would not be obstructed and that the mesh diagram could be clearly projected onto the tunnel lining.

The accuracy of the travel distance measurement device was also verified. This validation was conducted over a total distance of 400 meters, using measurements from a high-precision laser doppler rail distance meter as the reference. The goal was to evaluate the accuracy of the projection system's distance measurement and determine the extent of any deviation. The results showed that the error was as small as 18 cm per 100 m. In general, tunnel inspection work is limited to about three to five hours per night, meaning that only a few hundred meters can be inspected during a single session. For example, even if adjustments were needed every time a 20 cm error occurred, the number of corrections required would be minimal. Moreover, since the adjustment can easily be made by manually rotating the distance measurement device, the measurement accuracy is considered sufficient for practical use.

Furthermore, to evaluate the time reduction effect of the hammering inspection, the time required for the survey was measured over a 10 m section under the same conditions, both with and without the projection device. The results clearly showed that using the projection device could halve the time required for the hammering inspection.

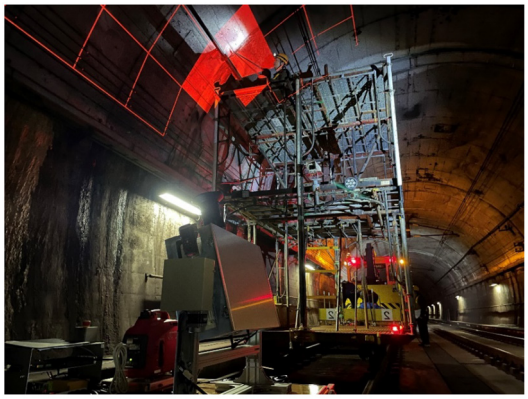

Fig. 12 Trial of hammering inspection from an aerial work platform

4. Conclusions

The key outcomes of this study are summarized below.

(1) The defect detection and soundness assessment application was validated through comparison with inspection records maintained by the railway operator. This confirmed that the application can accurately detect surface defects and assess overall tunnel soundness trends prior to on-site inspections of critical sections.

(2) The on-site validation confirmed that the projection system accurately displays mesh diagrams and that its distance measurement capability provides sufficient precision for practical use.

(3) Trial inspections using the developed technology showed that the inspection process can be significantly streamlined.

The projection system is mounted on a lightweight trolley designed for on-foot inspections We are currently working on improvements to support future inspections using work vehicles and elevated platforms, such as reducing the projector's weight, enabling split projection, and enhancing the distance measurement system.

Acknowledgment

This research was conducted with support from the Ministry of Land, Infrastructure, Transport and Tourism under the Transportation Technology Development Promotion Program (JP002223).

References

[1] Railway Technical Research Institute,"*Maintenance Standards for Railway Structures and Commentary (Tunnel)*," Maruzen publishing, 2007.

[2] Railway Statistics Annual Report, Railway Bureau, Ministry of Land, Infrastructure, "*Transport and Tourism (MLIT) (FY2021 Edition)*," 2022 (in Japanese).

[3] Ministry of Health, "*Labor and Welfare: Analysis of the Labor Economy — Toward a Society Where Everyone Can Thrive Amid Population Decline*," 2016 (in Japanese).

[4] Ministry of Land, Infrastructure, Transport and Tourism (MLIT), "*Initiatives Toward a Sustainable Society Through the Use of Technology*," MLIT, 2023 (in Japanese).

[5] Pang-jo CHUN, Atsushi IGO, “Crack detection from image using random forest,”*Japanese Journal of JSCE F3(Civil Engineering Informatics)*, Vol. 71, No. 2, pp. I_1-I_8, 2015 (in Japanese).
[6] KAISE Shinobu, ITO Tetsuo, MAEDA Yashikatsu, YAGI Hiroshi, MAEDA Kouki, SHINJI Masato, “Possibility on substitution close visual inspection for imaging technology to tunnel lining health monitoring,” *Japanese Journal of JSCE F1(Tunnel Engineering)*, pp. 62-78, 2020 (in Japanese).

Authors

Yudai YAMASHITA
Researcher, Tunnel Engineering
Laboratory, Structures Technology Division
Research Areas: Tunnel Engineering

Kazuhide YASHIRO, Dr.Eng.
Manager, Tunnel Engineering
Laboratory, Structures Technology Division
Research Areas: Tunnel Engineering

Takashi NAKAYAMA, Dr.Eng.
Senior Chief Researcher, Head of Tunnel
Laboratory, Structures Technology Division
Research Areas: Tunnel Engineering

Development of a Baseplate with Elastic Support Structure for Rigid Crossings in Direct Fixation Turnout with Composite Sleepers

Saki SHIMIZU **Shingo TAMAGAWA**
Track Structures and Components Laboratory, Track Technology Division

Ryosuke OTAKA **Tadashi DESHIMARU**
Track Structures and Components Laboratory, Track Technology Division (Former)

Shingo MATSUTANI
Track Structures and Components Laboratory, Track Technology Division

Turnouts fixed directly to composite sleepers for the shinkansen have large dents on the nose rails, compared to those of ballasted turnouts. To solve this issue, focusing on the dynamic load difference under different support conditions, the authors developed the new baseplate for rigid crossings with elastic support. The developed baseplate can make the depth of dents on nose rails of turnout fixed directly to composite sleepers equal to that of a ballasted turnout. In addition, it is compatible and replaceable with conventional baseplates.

***Key words*:** *turnout, crossing, fastening, elastic support, analysis, performance verification*

1. Introduction

As illustrated in Fig. 1, a structure that separates railway tracks into two or more directions is known as a turnout. This structure comprises points, leads, crossings, and guards [1]. The crossing illustrated in the figure is classified as a rigid crossing. Rigid crossings (hereinafter referred to as "crossings") contain gaps in gauge lines, which can cause structural impacts as train wheels transition from the nose rail to the wing rail (or vice versa). This transition often results in plastic deformation or rolling contact fatigue (RCF) damage to the rails at the transfer points, and such damage is a significant factor in the replacement of crossings [2]. Additionally, direct fixation turnouts with composite sleepers (hereinafter referred to as "direct fixed turnouts") are utilized as a labor-saving solution for turnouts [3]. As shown in Fig. 2, these turnouts feature a design in which composite sleepers (hereinafter, "sleepers") are directly supported on the concrete roadbed using synthetic resin.

This study focuses on rigid crossings for direct fixed turnouts installed on shinkansen lines. Compared to ballasted turnouts, these crossings exhibit greater deformation of the nose rail head per unit of passing tonnage, often leading to shorter replacement cycles. Consequently, measures are needed to mitigate this deformation. One reason for this issue is that direct fixed turnouts have a structure in which composite sleepers are directly supported by the concrete roadbed and synthetic resin, resulting in a more rigid support system than that of ballasted turnouts.

In previous field surveys, we reported that direct fixed turnouts exhibit greater track support rigidity (Fig. 3) and larger deformation size per passing tonnage (Fig. 4) than ballasted turnouts. We also reported that the deformation shape of nose rails (Fig. 5) shows localized deformation compared to ballasted turnouts. We developed a vehicle running analysis model using FEM solid elements to simulate the crossing, and confirmed its validity [4]. In Fig. 5, the reference position indicates the fastening point near the nose rail tip. In this paper, we describe the nose rail position along the rail's longitudinal axis as the distance from this reference point.

This study examined the impact of support stiffness on acting load and introduced a new baseplate featuring an elastic support structure (hereinafter referred to as the "developed product"). The

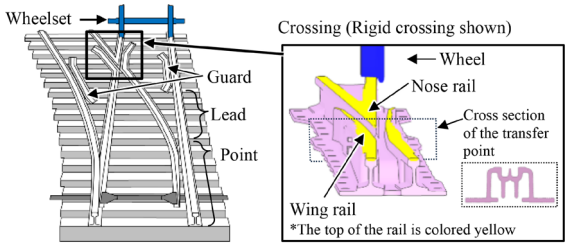

Fig. 1 Crossing of a turnout and part names

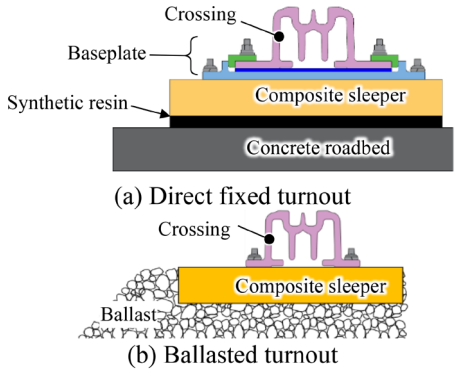

Fig. 2 Comparison of turnout structures

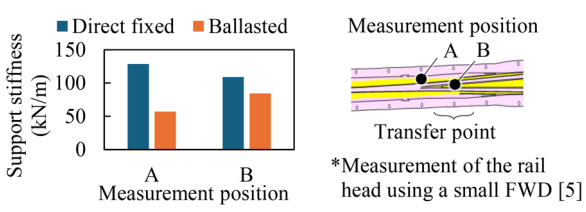

Fig. 3 Measurement results of track support stiffness at transfer points [4]

objective was to ensure that the deformation of the nose rail head at direct fixed turnouts matches that at ballasted turnouts. This paper presents the performance verification and test installation of the developed product.

This paper focuses on crossings with a crossing angle of approximately 6.24×10^{-2} rad, which is the most common installation in Japan. The speed limit for trains passing through a rigid crossing on a shinkansen turnout is 130 km/h on main lines and 75 km/h on branch lines. Based on previous surveys of train speeds at turnouts, this study was conducted within a running speed range of 65 to 130 km/h.

2. Outline of elastic support structure

2.1 Current baseplate

The current baseplate for direct track (referred to as the "current product") has the structure shown in Fig. 6 to enable vertical and lateral adjustment, since sleepers are fixed to the concrete roadbed. As illustrated in Fig. 6, an adjustment plate is installed between the crossing and the baseplate body to facilitate vertical adjustments. Additionally, the baseplate body features a shoulder that slopes along the rail longitudinal direction, enabling lateral adjustment by moving a clip plate in that direction.

2.2 Structural design of developed product [6]

The developed product was designed as per the following criteria:

(1) Must elastically support the crossing.
(2) Must allows replacement of current product without need to modify sleepers.
(3) Must not compromise up/down and left/right adjustment functions of existing product.

Figure 7 illustrates the developed product, designed and prototyped in accordance with the conditions outlined above. Here are the key features:

(1) Double elastic fastening structure is achieved by placing rail pad beneath crossing and securing clip plate with plate spring.
(2) Rail pad is designed to ensure variation of wheel load during crossing operations is equivalent to that experienced in a ballasted turnout. Explained in next section.
(3) Baseplate body is divided into two sections referred to as "lateral support blocks" to align height of crossing with current product.
(4) Vertical adjustments made using an adjustment plate (for the crossing) installed between rail pad under crossing and floor plate, similar to existing product. Additionally, adjustment plate (for the clip plate) is positioned under the clip plate to ensure its position remains stable.
(5) When replacing current product, screw hole positions of current and developed products are separated by more than 50 mm, allow-

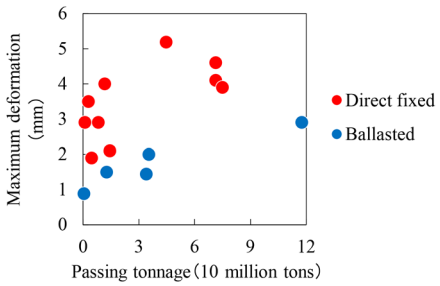

Fig. 4 Deformation measurement results [4]

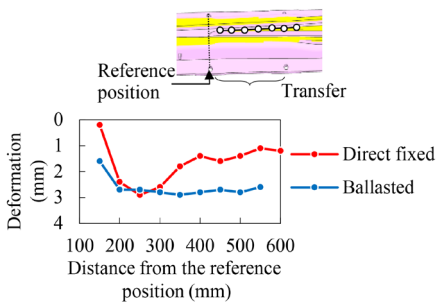

Fig. 5 Measurement results of nose rail deformation shape [4]

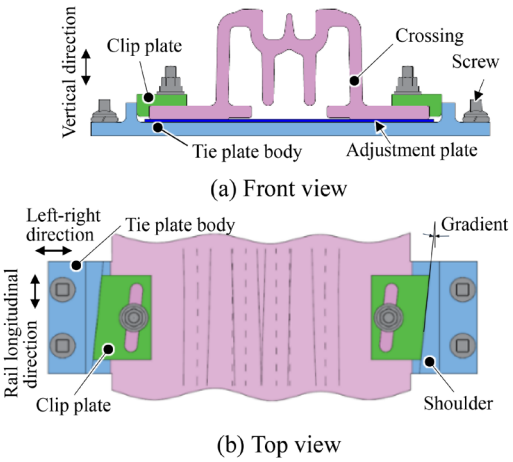

Fig. 6 Current baseplate

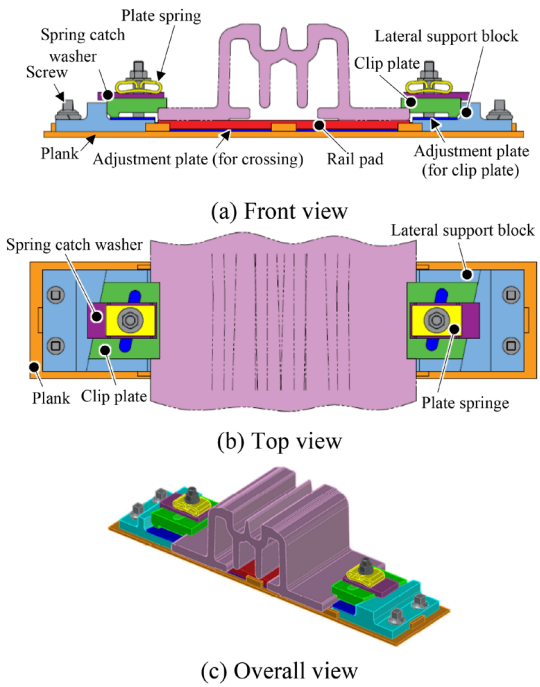

Fig. 7 Structure of developed product

ing for screw hole replacement without the need for repairs [7].

2.3 Design of rail pads

2.3.1 Specifying cause of deformation

To estimate the factors contributing to differences in deformation between direct-fixed and ballasted turnouts, we first analyzed the effects of trains passing over a deformed crossing. The deformation shape of the nose rail, as shown in Fig. 5, was applied to the running analysis model depicted in Fig. 8(a) [4] and a running analysis was performed. Figure 8(b) illustrates the calculated maximum fluctuations in wheel load caused by the impact of transfer loads (hereafter referred to as "transfer impact loads"). The deformation shape shown in Fig. 5 indicates that ballasted turnouts exhibit a gradual change from the nose rail tip to the rear. In contrast, direct fixed turnouts tend to show larger, localized deformations. This result suggests that, even with similar maximum deformation levels, direct fixed turnouts generate greater impact loads due to the transfer effect compared to ballasted turnouts. Moreover, for direct fixed turnouts, greater deformation tended to increase impact loads, which may further worsen deformation.

To estimate the factors that cause differences in deformation shapes, an analysis was conducted assuming that trains travel through a crossing with a design shape that reflects the early stages of installation. Figure 9 illustrates the variation in wheel load during the transfer process. The lateral axis is consistent with that of Fig. 5.

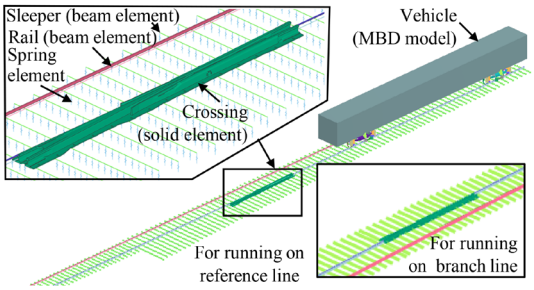

(a) Overview of driving analysis model [4]

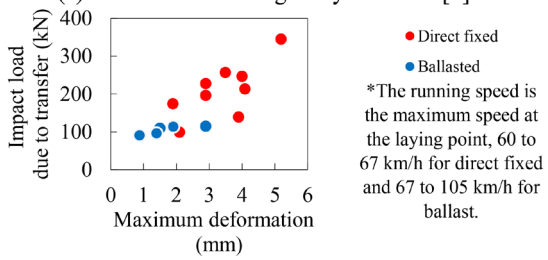

(b) Relationship between maximum deformation and impact load

Fig. 8 Analysis of crossing traffic over time

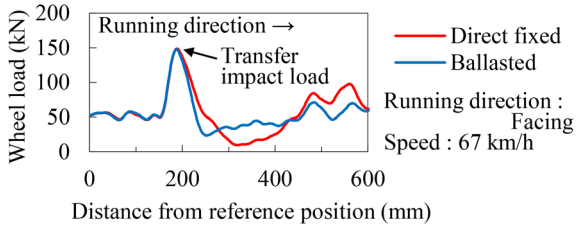

Fig. 9 Results of runing analysis

The results indicate that, while the impact load due to the transfer is similar in both cases, the wheel load waveforms following the impact differ. Moreover, Fig. 10 presents the results of calculating the nose rail deformation caused by the wheel load during the early stages of use after installation (as shown in Fig. 9). This calculation is based on the wheel load contact area at the transfer point and the plastic deformation characteristics of the high manganese steel [8] used in the crossing. The results confirmed that, due to the nose rail's structure, the contact area with the wheel is small, leading to deformation even under low loads. Furthermore, although the maximum deformation tended to be similar, noticeable differences in deformation shape were observed, with larger localized deformation in the direct fixed turnout.

Based on the analysis above, the following factors are believed to contribute to the differences in deformation observed between direct fixed and ballasted turnouts:

(1) Variations in the support structure of the crossing lead to differences in the variation of wheel load following the impact of transfer.
(2) Due to these differences in variation in wheel load, direct fixed turnouts experience more localized deformation compared to ballasted turnouts.
(3) This localized deformation amplifies the impact load generated during vehicle travel after a transfer.
(4) Consequently, significant impact loads are exerted on the nose rail, further exacerbating the deformation.

2.3.2 Elastic material design and preparation

The elastic material was designed based on the following criteria, focusing on the causes of deformation:

(1) Reduce the decrease in wheel load due to impact.
(2) Limit the increase in wheel load following an impact.

Since the increase in wheel load is believed to be a reaction to the loss of wheel load, we first calculated the physical properties of the rail pad that can mitigate this loss. A running analysis was performed to determine the spring constant, damping coefficient, and minimum wheel load of the rail pad, and target values were established (Fig. 11). It is important to note that the spring constant and damping coefficient values presented in this paper are per fastening.

Consequently, material IV was selected based on its spring constants and damping coefficients, which closely matched our target values among the five types of materials, as illustrated in the figure. To accurately replicate dynamic behavior, the spring constant and damping coefficient were derived from dynamic loading tests focused on the frequency range of vibrations produced by the transfer impact.

Using material IV, we manufactured material A, which had the same groove shape as material IV but matched the rail pad size used in the developed product. Additionally, we created material B, which had a lower spring constant due to its groove design. The groove

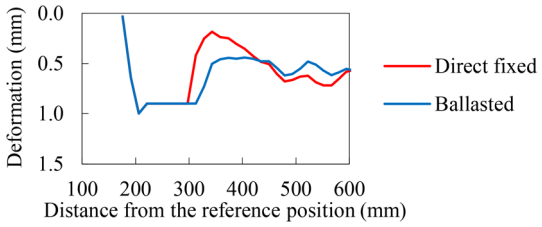

Fig. 10 Deformation of nose rail

shape, the pattern carved into the rail pad's surface, significantly influences both the spring constant and the damping coefficient. Figure 12 presents the wheel load results from a running analysis that accounts for the physical properties of materials A and B. The results indicated that material B, which effectively reduced the decrease in wheel load and minimized subsequent variation in wheel load, was ultimately selected as the rail pad for the developed product.

2.4 Position for installing developed product

The developed product was installed in six fastenings located near the crossing transfer point, as illustrated in Fig. 13. This decision was based on a running analysis, shown in Fig. 14, which compared three scenarios: the product installed at all crossing fastenings, and at either four or six fastenings near the transfer point.

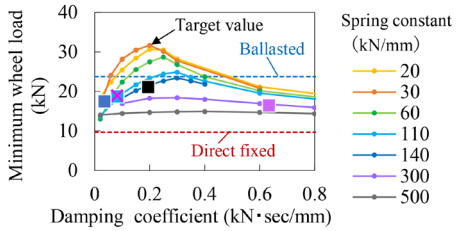

Legend	【Rail pad specimen】※1 Soft←Hardness→Hard					Dynamic spring constant※2 (kN/mm)	Damping coefficient※2 (kN・sec/mm)
	I	II	III	IV	V		
■	○					44	0.04
×		○				92	0.08
■			○			96	0.08
■				○		160	0.20
■					○	347	0.63

※1 SBR used in general railway pads.
※2 Target frequency is 45 Hz.

Fig. 11 Spring constant and damping coefficient of each material

	Dynamic Spring Constant* (kN/mm)	Damping Coefficient* (kN・sec/mm)	Static Spring Constant (kN/mm)
A	184	0.214	115
B	100	0.138	54

* Target frequency is 45 Hz

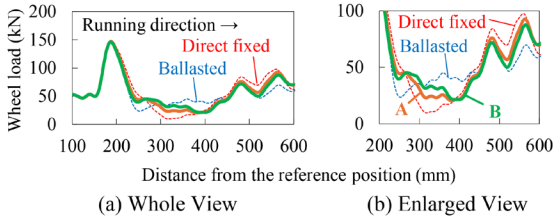

Fig. 12 Wheel load results for rail pads A and B

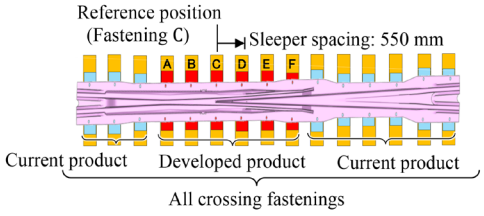

Fig. 13 Position for installing of developed product

The analysis confirmed that the variation in wheel load in the six fastenings was more comparable to that observed when the product was installed across all crossing fastenings.

3. Performance verification [7]

The developed Baseplate underwent a safety review for fatigue fracture, in accordance with section "5.5 Rail Fastening Devices" of the Design Standard for Railway Structures and Commentary—Track Structure (hereinafter referred to as the "Design Standard") [9].

3.1 Performance verification method, performance requirements, and verification items

Table 1 presents the performance requirements and related items as outlined in the design standard, while Table 2 lists the tests and verification indices conducted to confirm safety against fatigue fractures.

Two types of design actions were utilized in the verification process:

Pattern 1: This pattern considered the effects of transfer and represented the design action for the rail fastening device at the rail joint.

Pattern 2: This pattern calculated the maximum wheel load and lateral force during crossing travel using a Finite Element Method (FEM) analysis model [4]. The calculation conditions are detailed in Table 3, and the corresponding calculated design actions are presented in Table 4.

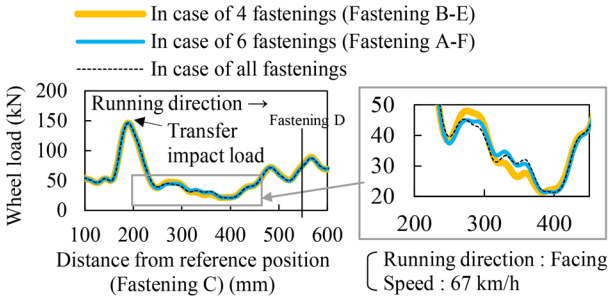

Fig. 14 Wheel load results from driving analysis

Table 1 Performance requirements and items

Performance requirements	Performance items
Safety	Fatigue fracture

Table 2 Test items and verification indices

Test items	Verification indices
Two-directional static loading test	Plate spring stress Rail head lateral displacement
Dynamic two-axial loading test	Appearance of components

Table 3 Calculation Conditions

Design axle load (kN)	Running speed (km/h)	
	Reference line	Branch line
170	130	75

Table 4 Design action

Design Action Patterns	Load Type	Load A (Exceptionally large load rarely encountered)	Load B (maximum load frequently encountered)
1	Wheel load	140.3 kN	97.8 kN
	Lateral force	86.3 kN	34.0 kN
2	Wheel load	177 kN	
	Lateral force	44 kN	

Safety verification regarding fatigue fracture was conducted using the following verification formula.

$$\gamma_i \cdot \frac{I_{Rd}}{I_{Ld}} \leq 1.0 \quad (1)$$

In this context, I_{Rd} represents the design response value, I_{Ld} stands for the design limit value, and γ_i is the track structural coefficient. The design response value I_{Rd} is determined by multiplying the response value I_R by the structural analysis coefficient γ_a. The response value I_R refers to the lateral displacement of the rail head and the stress experienced by the plate spring, which are measured through a two-directional static loading test.

The design limit value I_{Ld} was calculated by dividing the limit value I_L by the track material coefficient γ_b. For the shinkansen line, the railhead lateral displacement was set at a design limit of 5.2 mm. Additionally, the plate spring stress was established based on the second fracture limit and the second settling limit found in the endurance limit diagram for spring steel (SUP9) [8]. In this verification process, the track structure coefficient γ_i, the structural analysis coefficient γ_a, and the track material coefficient γ_b were all set to 1.0.

Among the verification items listed in Table 2, the appearance of the components was assessed through a dynamic two-axial loading test. This test aimed to ensure that there were no abnormalities in the components' appearance afterwards.

Both the static and dynamic two-axial loading tests were conducted using the "load test method for one set of rail fastening devices" as outlined in the design standard [4].

3.2 Two-directional static loading test

3.2.1 Calculation of fastening position at which plate spring generates maximum stress

In the applicable range of the developed product, the fastening position that is expected to experience the largest deflection angle and the maximum stress in the plate spring was determined using a finite element method (FEM) analysis model. Figure 15 illustrates the analysis model, while Table 5 provides the spring constants. Figure 16 shows the maximum deflection angle at fastening positions A to B when the design actions listed in Table 4 are applied. It is important to note that the deflection angle is considered positive when the rail deflects outward toward the gauge. The analysis revealed that for all design actions, fastening position C exhibited the largest deflection angle and the highest stress in the plate spring.

3.2.2 Determination of loading condition

The test load and loading height for experiments involving a single fastening are determined by evaluating the rail pressure, the lateral rail pressure, and the rail tilting moment. Table 6 presents the rail pressure and the lateral rail pressure for the design action ap-

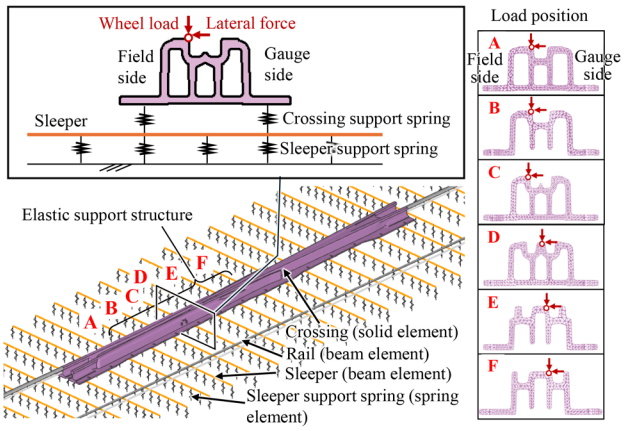

Fig. 15 Overview of analysis model

Table 5 Spring constant (kN/mm)

Direction	Crossing support spring		Sleeper support spring
	Elastic support structure	Current product	
Vertical	53※	Rigid connection	Equivalent to direct track [4]
Lateral	67※	200	Rigid connection
Front and rear	67	200	31

※Calculated from the results of static load tests on a single fastening

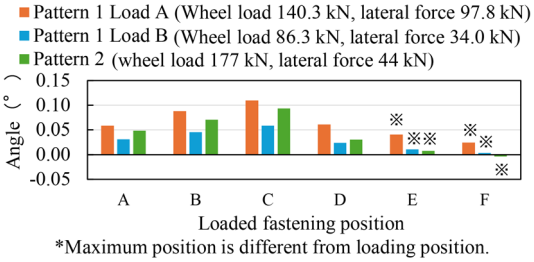

*Maximum position is different from loading position.

Fig. 16 Maximum deflection angle when design loads are applied to A through F

Table 6 Rail pressure and lateral rail pressure

	Pattern 1		Pattern 2 (kN)
	Load A (kN)	Load B (kN)	
Rail pressure	35.4	24.4	44.8
Lateral rail pressure	10.7	2.9	2.1
Increased lateral rail pressure	18.2 (+7.5)	9.9 (+7.0)	17.4 (+15.3)

( ) represent the load increase

plied at fastening position C, which exhibited the largest lateral deflection angle in previous analyses. When calculating the loading height to balance the rail tilting moment obtained from the analysis, the rail pressure and the lateral rail pressure from Table 6 were applied to a test rail that simulates a crossing, as illustrated in Fig. 17. This calculation showed that the required test rail height (H) was approximately 400 mm, exceeding the testing machine's loading height limit. Consequently, the test rail height was adjusted to 220 mm, the maximum height compatible with the testing machine. To ensure that the rail tilting moment matched the earlier analysis, the lateral test load was set higher than the lateral rail pressure specified in Table 6. Specifically, the lateral test load is up to 15 kN greater than the lateral rail pressure, as noted in the bottom row of Table 6. Although this results in a more rigorous condition for assessing lateral force strength—such as the potential for lateral slippage of the lateral force-bearing metal fittings—the test results are considered to be inclusive of those obtained at a height of 400 mm.

The vertical and lateral loads, denoted as P1 and P2, are applied to a specific set of Baseplates based on the results of the previous study. The maximum values, P1max and P2max, for P1 and P2 are presented in Tables 7 and 8. During testing, P1 is applied to the test rail from the angle θ1, while P2 is applied from the angle θ2, as illustrated in Fig. 17.

3.2.3 Test and verification results

A two-directional static loading test was conducted following the procedure outlined in Table 9. The stress generated in the plate springs during this test was plotted on an endurance limit diagram, as shown in Fig. 18. From this figure, it is evident that the stresses in the plate springs for patterns 1 and 2 were within the second fracture limit and second settling limit. The maximum lateral displacements of the rail head were 0.50 mm for pattern 1 and 0.42 mm for pattern 2. Table 10 presents the results of verifying these measurements using equation (1). The data in Table 10 confirm that both the stress in the plate springs and the lateral displacement of the rail head satisfied the validation criteria.

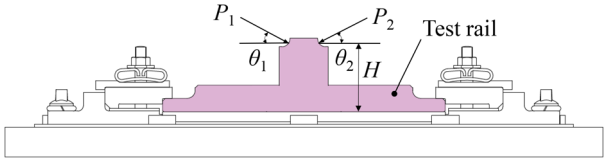

Fig. 17 Loading method

Table 7 Vertical and lateral loads for pattern 1

	Vertical load (kN)	Lateral load (kN)	Test load (kN)	Angle (°)
P_{1max}	35.4	18.2	37.4	θ_1=56.2
P_{2max}	24.4	9.9	23.9	θ_2=57.9

Table 8 Vertical and lateral loads for pattern 2

	Vertical load (kN)	Lateral load (kN)	Test load (kN)	Angle (°)
P_{1max}	44.8	17.4	44.8	θ_1=64.1
P_{2max}	44.8	17.4	44.8	θ_2=64.1

3.3 Dynamic two-Axial loading test

The purpose of this test was to assess any abnormalities in the components following a safety check for fatigue fractures.

A dynamic two-axial loading test was performed, as illustrated in Fig. 19, following the procedure outlined in Table 11. As a result, no cracks, significant wear, or other abnormalities were detected in components such as the plate springs, fastening bolts, and rail pads after enduring 1 million loads.

Based on these findings, the safety check for abnormalities in the components after the test was successful.

4. In-situ test measurement

To evaluate the workability and effectiveness of the developed

Table 9 Loading procedure for static two-axial loading test

Loading cycle	Test load (kN)
Preliminary loading	P_1: 0.0 → 5.0 P_2: 0.0 → 5.0
1st to 3rd sessions (Equivalent to A load: P1 load)	P_1: 5.0 → P_{1max} → 5.0 P_2: 5.0 (constant)
4th to 6th sessions (Equivalent to B load: P2 load)	P_1: 5.0 (constant) P_2: 5.0 → P_{2max} → 5.0

P_{1max}: Pattern 1 37.4 kN, Pattern 2 44.8 kN
P_{2max}: Pattern 1 23.9 kN, Pattern 2 44.8 kN

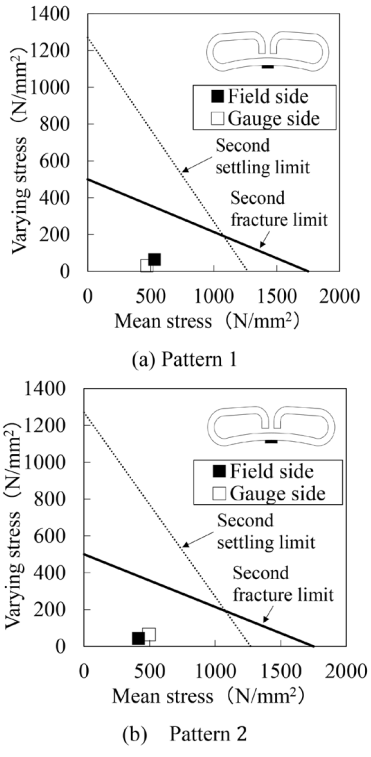

(a) Pattern 1

(b) Pattern 2

Fig. 18 Verification using durability limit diagram

Table 10 Verification results of plate spring stress and rail head lateral displacement

Verification indicators		Plate spring Generated stress	Lateral displacement of rail head
Response value	I_R	Two-directional static loading test stress	Two-directional static loading test displacement
Design response value	I_{Rd}	1.0 I_R	1.0 I_R
Limit value	I_L	Second fracture limit and second settling limit	5.2 mm
Design limit value	I_{Ld}	I_L/ 1.0	I_L/ 1.0
Track structure coefficient	γ_i	1.0	1.0
Verification formula		$\gamma_i \cdot \frac{I_{Rd}}{I_{Ld}} \leqq 1.0$	
Verification results※	Pattern 1	○	○ (0.096)
	Pattern 2	○	○ (0.081)

※Verification results: ○: Meets required performance, ×: Does not meet required performance

Fig. 19 Dynamic two-axial loading test status

Table 11 Loading procedure for dynamic two-axial loading test

Item	Unit	Loading conditions
Load	kN	P_1: 5.0~P_{1max}(Angle: θ_1)
		P_2: 5.0~P_{2max}(Angle: θ_2)
Repetition frequency	Hz	5.5
Target repetitions	Times	1×10^6

P_{1max}: Pattern 1 37.4 kN, Pattern 2 44.8 kN
P_{2max}: Pattern 1 23.9 kN, Pattern 2 44.8 kN

product, a test installation was conducted on a standard turnout on a shinkansen track.

At the six-section fastening illustrated in Fig. 13, the existing baseplate was removed, and a baseplate with the newly developed elastic support structure was installed. The crossing itself was also replaced. It was confirmed that both the installation of the new baseplate and the crossing replacement could be completed without issue within the approximately three-and-a-half-hour overnight work window. The installation status is depicted in Fig. 20.

Figure 21 presents the deformation results for the developed product at 2 weeks, 1 month, and 6 months after installation. For

Fig. 20 Installation status

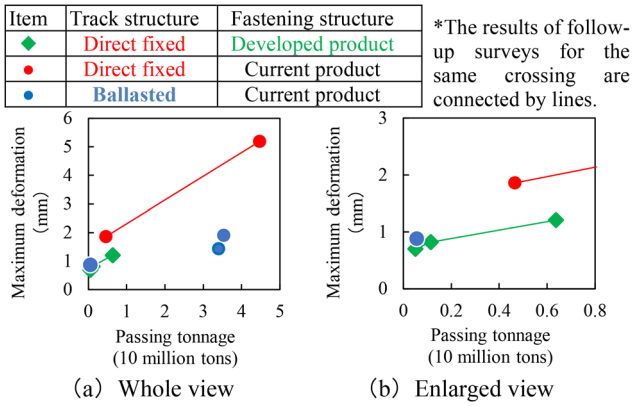

(a) Whole view (b) Enlarged view

Fig. 21 Changes in deformation size

comparison, results from a previous crossing installed at the same location, as well as from a ballasted turnout crossing at a different location, are also included.

Six months after installation, the developed product had experienced a total passing tonnage of 6.37 million tons, with a deformation measurement of 1.2 mm. Linear interpolation between the one-month and six-month data revealed a reduction of approximately 40% in deformation compared to the current product, which had a passing tonnage of about 4.66 million tons. Furthermore, two weeks post-installation, the developed product had a passing tonnage of 510,000 tons and a deformation of 0.7 mm. This result is similar to the 0.9 mm deformation observed in a ballasted turnout crossing with a passing tonnage of 560,000 tons.

These results confirm the effectiveness of the developed product in reducing deformation, particularly in the early stages of installation, when deformation tends to progress most rapidly.

5. Summary

We developed a Baseplate designed for crossings with an elastic support structure. The key findings are summarized as follows:

- Our Baseplate features a double-elastic fastening system. This design features a rail pad beneath the crossing, with the clip plate secured using the plate spring.
- The performance of this new product was evaluated according to design standards, and it successfully passed safety checks concerning fatigue fractures.
- We conducted a test installation of the developed product on a standard turnout for the shinkansen. The installation proceeded without issues. Additionally, six months after installation, we observed that the nose rail deformation was approximately 40% lower than that of the existing product, aligning more closely with levels observed in ballasted turnouts.

We will continue to monitor the deformation over time to vali-

date the effectiveness of the developed product during long-term installation. Furthermore, we plan to expand the application of this product to additional locations and various types of turnouts.

References

[1] Oikawa, Y., "Turnouts," *RRR*, Vol. 73, No. 9, pp. 28-31, 2016 (in Japanese).
[2] Sato, K. and Kozu, D., "Research on material condition management for crossings," *Japan Society of Civil Engineers 2011 Annual Meeting*, IV-122, pp. 243-244, 2011 (in Japanese).
[3] Suda, M., Nagato, A., Tokuoka, K. and Miura, S., "Atarasii Senro," pp. 466-468, 1997 (in Japanese).
[4] Shimizu, S., Shiota, K., Yamamoto, T., and Oikawa, Y., "Basic study on damage of rigid crossing in turnout laid on synthetic sleeper on direct fixation," *Journal of railway engineering*, No. 26, pp. 209-216, 2022 (in Japanese).
[5] Itou, K., Nakamura, T. and Sano, T., "Study on evaluation of track support state using FWD," *The Journal of Japan Railway Civil Engineering Association*, pp. 60-63, 2014 (in Japanese).
[6] Otaka, R., Shimizu, S., Tamagawa, S., Deshimaru, M., "Development of baseplate for rigid crossings with elastic support," *J-RAIL2024*, 2024 (in Japanese).
[7] Sato, Y., "Bungiki no kozo to hosyu- enlarged and revised edition –," p. 339, 2017 (in Japanese).
[8] Otaka, R., Shimizu, S., Sato, H., Ueda, M., "Weight drop tests on the dents of rigid crossings made of high manganese steel," *Japan Society of Civil Engineers 2024 Annual Meeting*, 2024, (in Japanese).
[9] Supervised by the Ministry of Land, Infrastructure, Transport and Tourism, "Design Standards for Railway Structures and Commentary (Track Structures)," pp. 52-60, 2012 (in Japanese).
[10] Tamagawa, S., Deshimaru, T. and Yamamoto, T., "Test method for loading tracks composed of a set of rail fastening systems for rail joints," *RTRI Report*, Vol. 37, No. 2, pp. 25-31, 2023 (in Japanese).

Authors

Saki SHIMIZU
Senior Researcher, Track Structures and Components Laboratory, Track Technology Division
Research Areas: Turnout Structure

Ryosuke OTAKA
Senior Researcher, Track Structures and Components Laboratory, Track Technology Division
Research Areas: Turnout Structure

Shingo TAMAGAWA, Ph.D.
Senior Researcher, Track Structures and Components Laboratory, Track Technology Division
Research Areas: Rail Fastening, Continuous Welded Rail

Tadashi DESHIMARU, Ph.D.
Senior Researcher, Track Structures and Components Laboratory, Track Technology Division
Research Areas: Railway Rails, Rail Fastening Systems

Shingo MATSUTANI
Researcher, Track Structures and Components Laboratory, Track Technology Division
Research Areas: Track Structure

Fundamental Study on Crack Detection Method for Prestressed Concrete Sleepers Using Deep Learning Model

Shintaro MINOURA **Tsutomu WATANABE**
Track Dynamics Laboratory, Railway Dynamics Division

Prestressed concrete sleepers are an important component of railway tracks, contributing to the speed and safety of train operations. Cracks appearing in the longitudinal direction of some prestressed concrete sleepers in recent years due to alkali–silica reactions have raised concerns about the efficiency of their maintenance. Therefore, this study proposes the use of a deep learning model to estimate the position and length of cracks on top surface images of prestressed concrete sleepers, as captured by a camera mounted on a maintenance vehicle. The applicability test confirmed that the method can accurately estimate the position and length of cracks in prestressed concrete sleepers, while minimizing the likelihood of false detection of ballast and fastening devices. In addition, it was demonstrated that this method can be employed to identify areas with a high concentration of cracks and analyze crack patterns on commercial lines.

***Key words*:** *prestressed concrete sleepers, longitudinal crack, image analysis, semantic segmentation*

1. Introduction

Prestressed concrete sleepers are essential components of railway tracks, enabling higher train speeds and improving safety. Prestressed concrete sleepers are resistant to decay typically observed in wooden sleepers, and are highly durable. Additionally, they are significantly heavier than wooden sleepers, thereby improving track stability. For these reasons, the use of prestressed concrete sleepers has been promoted to reduce maintenance costs and suppress track displacement.

Some of the prestressed concrete sleepers that are currently in use have been in operation for over 50 years. Progressive wear has been observed in track environments with relatively high cumulative tonnage which is the total weight of trains passing through a given section [1]. In addition to wear, some cases of severe damage presumably caused by frost have resulted in a significant reduction in load-bearing capacity [2, 3]. As a result, demand for replacing existing prestressed concrete sleepers with new ones has increased in recent years, prompting investigations into their current condition and studies on replacement criteria [4, 5, 6].

Figure 1 shows examples of longitudinal cracks in prestressed concrete sleepers. Figure 1(b) shows a longitudinal crack on the gauge corner (GC) side (the inner side of the track gauge). Figure 1(c) shows a longitudinal crack on field corner (FC) side (the outer side of the track gauge). Longitudinal cracks along the sleeper are one of the representative damage modes in prestressed concrete sleepers and are often attributed to the alkali–silica reaction (ASR) [7]. In practice, these cracks are generally identified through visual inspection. Maintenance work, such as sleeper replacement, is carried out depending on the severity of the cracks. However, since a large number of sleepers have been installed, on-site inspections require considerable effort, and it remains challenging to quantitatively evaluate crack length. Automating and quantifying these processes would greatly improve maintenance efficiency, replacement planning, and overall safety.

In recent years, some railway operators have installed cameras on in-service trains or maintenance vehicles to capture images of the track. The captured images are used for track component maintenance, improving maintenance efficiency. If the image data obtained through these methods could be used to automatically and quantitatively identify longitudinal cracks in prestressed concrete sleepers installed in the field, maintenance could be significantly reduced. At present, systems can detect the presence or absence of cracks on the top surface of prestressed concrete sleepers. Nevertheless, for detailed inspections such as determining the location and length of cracks, it is still necessary for inspectors to manually review the images. As such, achieving full automation remains challenging.

In recent years, numerous studies have investigated methods for detecting cracks in concrete using image analysis, with a particular focus on approaches leveraging deep learning techniques [8, 9]. However, in the case of crack detection for prestressed concrete sleepers, other components such as rail fastening systems, rails, and ballast (crushed stone), may be present around the sleepers and could be falsely detected as cracks. Additionally, many sleepers exhibit deteriorated surface conditions due to aging, which also contributes to false detection. Consequently, it has been difficult to directly apply methods or models used for other structures.

Therefore, this study proposes a crack extraction method and a

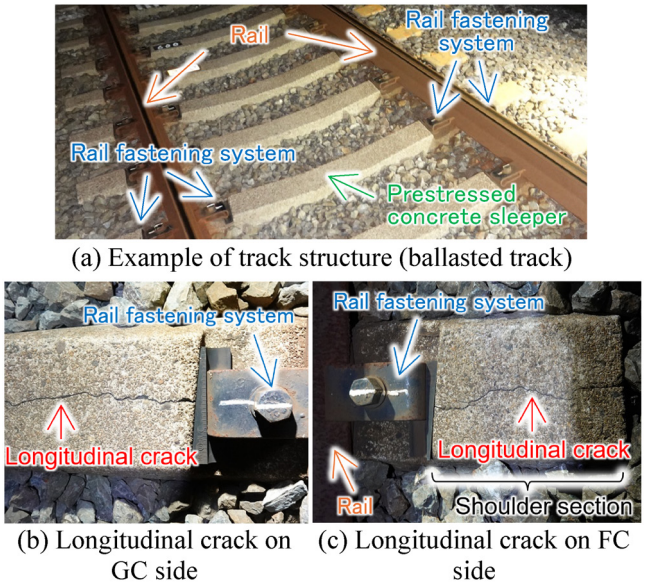

(a) Example of track structure (ballasted track)

(b) Longitudinal crack on GC side

(c) Longitudinal crack on FC side

Fig. 1 Example of track structure and longitudinal crack on prestressed concrete sleepers

crack length estimation method based on deep learning that can be applied to cracks occurring in prestressed concrete sleepers, and examines their applicability [10].

2. Overview of proposed image analysis method

2.1 Workflow of image analysis method

Figure 2 illustrates the workflow of the proposed image analysis method. The proposed approach targets image data captured from the top surface of prestressed concrete sleepers. First, a deep learning-based technique detects crack regions within the image data at the pixel level, and then an image indicating their positions (crack image) is generated. The next procedure is to apply the thinning process to the crack image to estimate its crack length. Finally, based on the dimensions of the object in the image, the estimated crack length is converted from pixels to the actual length in millimeters.

2.2 Images of prestressed concrete sleepers used in this study

Figure 3 shows an example of an image of the top surface of a prestressed concrete sleeper. In this study, we used images obtained from a system owned by a railway operator. This system uses cameras mounted on maintenance vehicles to capture images of the track from directly above. Five images are produced for each sleeper: two images on the field corner (FC) side, two near the gauge corner (GC) of the rail, and one at the center of the sleeper. For this investigation, only the images on the FC side were used. This is because images of the GC side and the center of the sleeper often include markings for maintenance purposes, such as sleeper numbers, as well as signal equipment. In that case, separate measures are required. The task of addressing these images is outside the scope of the present paper. Each image has a resolution of 400 × 340 pixels.

2.3 Deep learning-based crack detection method

The proposed image analysis method employs semantic segmentation to identify the location and length of cracks. Semantic segmentation is a deep learning algorithm that classifies objects at pixel-level within a target image [11]. It consists of an encoder that extracts features while downsampling the input image and a decoder that receives the extracted features and outputs classification results at the original image size. The encoder uses a technique called Fully Convolutional Networks (FCNs), an extension of Convolutional Neural Networks (CNNs), to extract features while downsampling. The decoder performs upsampling to the original pixel size by performing the reverse operation of the encoder, presenting the classification results at pixel-level.

Figure 4 shows an architecture of the crack detection model developed in this study. A model based on U-Net [12] was constructed for semantic segmentation. The U-Net is a semantic segmentation model characterized by skip connections that link feature maps from the encoder to those in the decoder (gray arrows in Fig. 4).

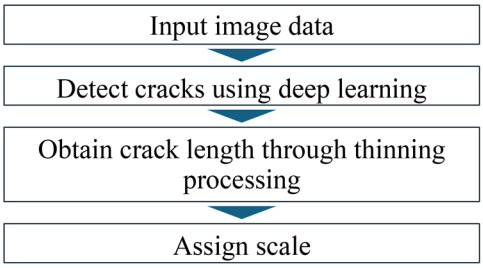

Fig. 2 Workflow of proposed image analysis method

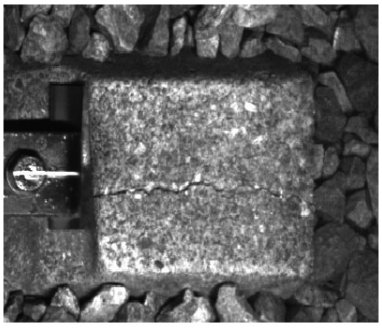

Fig. 3 Example image of the top surface of a prestressed concrete sleeper

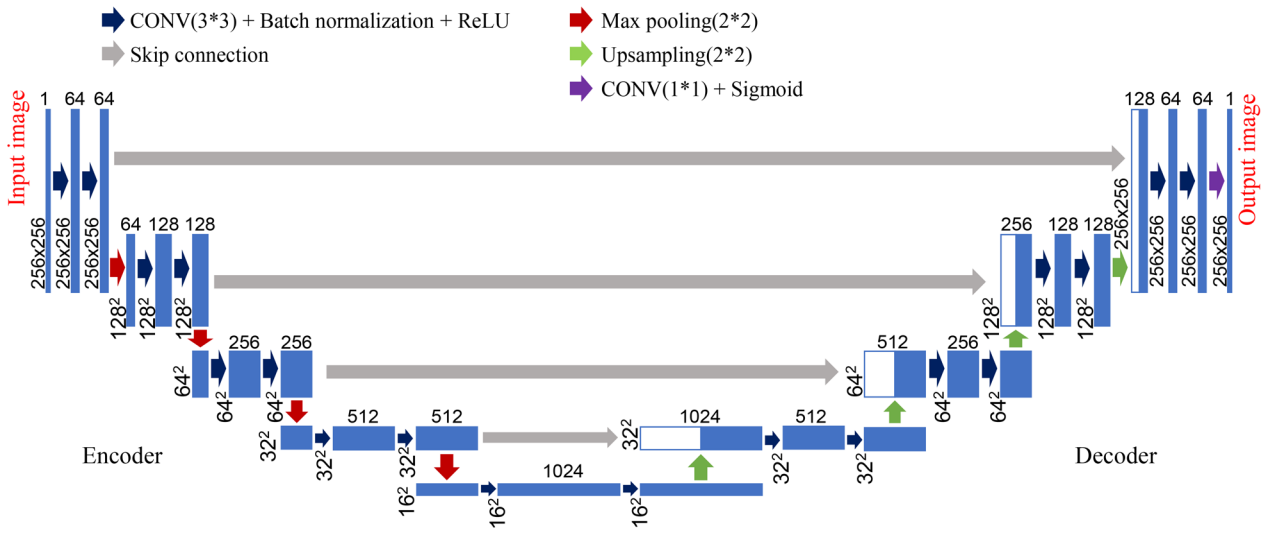

Fig. 4 Model architecture

These skip connections enable the decoder to receive local and spatial information lost in the encoder, allowing high-accuracy classification even after upsampling. This study involved developing a modified U-Net model by adding batch normalization layers to each convolutional layer. Batch normalization is expected to improve training efficiency and mitigate overfitting [13]. The final model performs binary classification at the pixel level to determine the presence or absence of cracks. The activation function in the output layer was set to the Sigmoid function, while the other layers used the ReLU function. The ReLU function outputs zero for input values less than zero and outputs the input value for values greater than or equal to zero. The Sigmoid function converts input values into a range between 0 and 1. In the output layer, the Sigmoid output for each pixel was divided into 256 levels to generate an image in which each pixel value represents the probability of a crack being present at that location.

Figure 5 shows an example of annotation. In the annotation process, only the pixels corresponding to a crack in the target image were filled in green. A total of 186 images were annotated. The identification of cracks was performed solely by examining the image data of prestressed concrete sleepers; the actual sleepers' surfaces were not inspected separately. Therefore, micro-cracks that cannot be distinguished from the image were excluded. Data augmentation was applied to the annotated images during training, involving random scaling, rotation, and horizontal translation. This resulted in a total of 1,000 annotated images. Of these, 900 were used for training and the remainder for accuracy validation. Regarding image size, the original images (400 × 340 pixels) were cropped by removing 30 pixels from both the left and right edges to create square images. These were then resized to 256 × 256 pixels. The number of epochs (iterations over the entire training dataset) was set to 100.

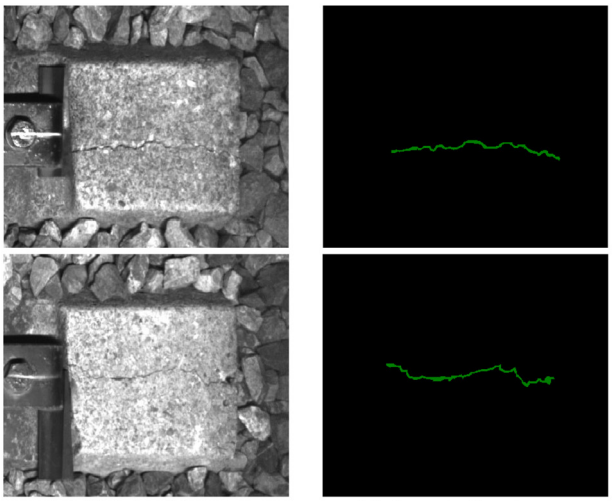

Fig. 5 Example of annotation

2.4 Crack length extraction using thinning process

Figure 6 illustrates an example of thinning applied to a crack image obtained by semantic segmentation to calculate crack length. As illustrated in Fig. 6(b), the crack image obtained by semantic segmentation, which extracts only the crack locations, varies with widths depending on the data. Therefore, calculating the area of these regions alone does not provide an accurate estimate of crack length. Moreover, ballast fragments or coarse aggregate edges may be falsely detected as small cracks in the crack image. To address this issue, the binarization of the image was first performed to retain only regions with pixel values above a certain threshold, thereby extracting the crack regions (Fig. 6(c)). Next, the binarized image was divided into connected regions (Fig. 6(d)), and the area of each region was calculated. Since cracks tend to occur continuously, regions below a certain threshold (pixels shown in light blue and blue in Fig. 6(d)) were considered likely to be noise or false detections caused by exposed aggregate edges and were removed (Fig. 6(e)). Subsequently, thinning was applied to the remaining regions (Fig. 6(f)). Thinning is the process of converting a binary image into a one-pixel-wide skeleton image. In this study, the Zhang–Suen thinning algorithm [14] was employed. Applying thinning enables crack locations to be represented as one-pixel-wide lines, allowing crack length to be estimated by counting the number of pixels. It should be noted that the calculated crack length may exceed the design longitudinal length of the prestressed concrete sleeper if the cracks are curved or if there are multiple cracks.

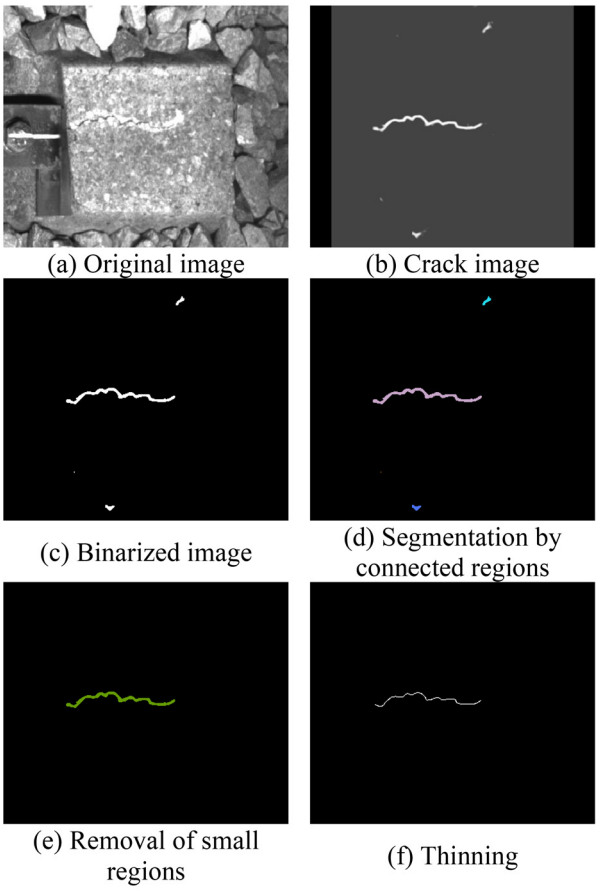

Fig. 6 Example of crack length calculation process

2.5 Scale assignment

Figure 7 illustrates the measurement locations used for scale calibration. Since the crack length obtained through thinning is expressed in pixels, it must be converted into the actual length in millimeters. To achieve this, 14 images of prestressed concrete sleepers were selected, and their pixel-based lengths were measured at the positions indicated in Fig. 7. The actual length per pixel (mm/pixel)

was calculated for each image using these measurements and the corresponding design dimensions, and then averaged. This average value was subsequently used to convert the crack length from pixels to millimeters. It should be noted that this approach assumes a fixed camera is mounted on a vehicle and captures images continuously while maintaining a constant distance from the sleeper. If the imaging conditions change, the actual length per pixel will also vary. Under the imaging conditions of this study, the conversion factor was approximately 1.0 mm per pixel.

3. Validation of proposed method

3.1 Accuracy evaluation procedure

The accuracy of the proposed method in detecting cracks was evaluated by comparing the estimated crack lengths obtained using the method with crack lengths measured through direct human visual observation. Specifically, 300 images capturing the shoulder areas of prestressed concrete sleepers on the field corner (FC) side were randomly selected, including images without cracks. The length of each crack was confirmed through direct human visual observation and then measured manually using a drawing tool. These visually measured lengths were treated as the "ground truth," while the lengths estimated by the proposed method were treated as the "predicted values." These two sets of values were then compared to assess the accuracy.

It should be noted that, due to the resolution of the target images, it was sometimes ambiguous to determine the exact endpoints of cracks by direct observation, and measurements were limited to a minimum unit of one pixel. Therefore, the visual measurements are assumed to include some degree of error. Furthermore, the method used to obtain the lengths of the manually drawn lines were consistent with that employed in the proposed method, namely thinning and pixel counting.

3.2 Validation results

Figure 8 presents the training process in terms of accuracy and loss. In Fig. 8, "Train" refers to the training dataset and "Val" refers to the validation dataset. As shown in the figure, the proposed model achieved over 99.3% accuracy in crack extraction for the validation dataset after approximately 30 epochs. However, it should be noted that the crack regions occupy a relatively small area compared to the non-crack regions; thus, even if all pixels were classified as non-crack, the accuracy would still be around 95%. After approximately 30 epochs, the accuracy of both the training and validation datasets stabilized at approximately 99.3%, with a loss of approximately 0.02, indicating sufficient learning without signs of overfitting.

Figure 9 to 11 show examples of the results of crack extraction. As illustrated in Fig. 9, cracks were extracted at positions generally consistent with those confirmed by direct human visual observation,

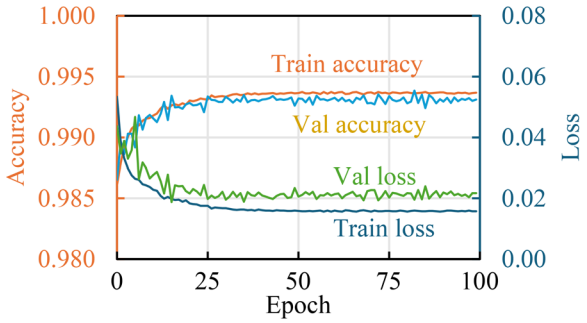

Fig. 8 Training process

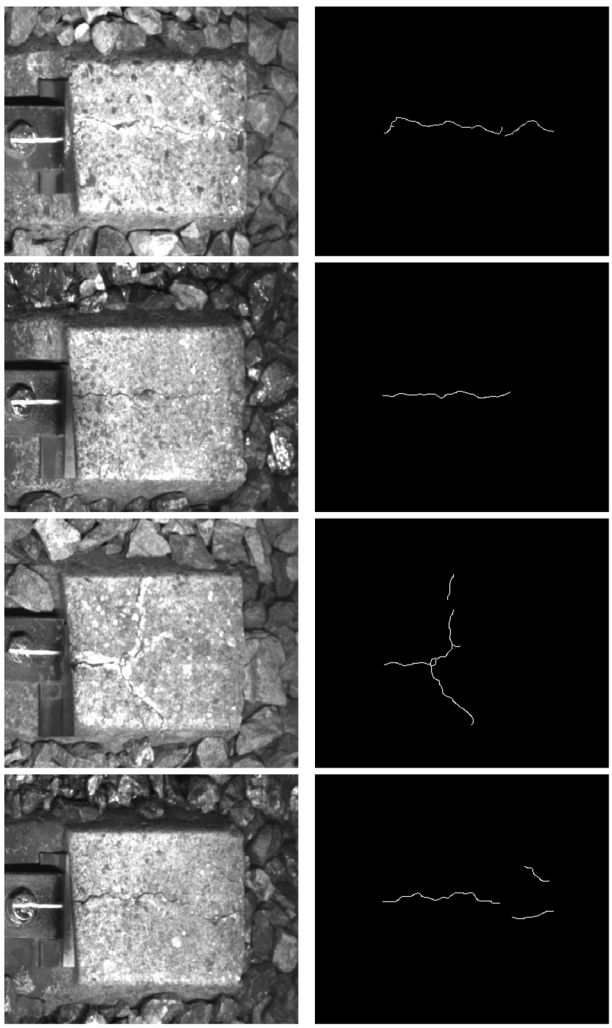

(a) Original image (b) Extraction result (Thinned result)

Fig. 9 Example of crack extraction result (successfully detected)

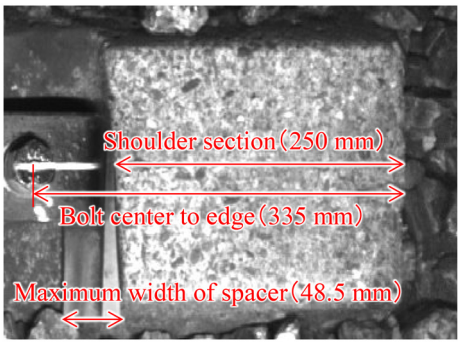

Fig. 7 Locations where reference lengths were measured for scale calibration

and no false detections were observed for rail fastening systems or ballast. On the other hand, as shown in Fig. 10, certain cracks were not detected (under-detection) in some cases where markers were applied in the field to facilitate crack identification or where lighting conditions were inadequate. Furthermore, as shown in Fig. 11, images containing equipment for cable protection or ballast scattered on the sleeper occasionally resulted in false detections of non-crack regions. Using alternative image processing techniques to identify such error-prone images and exclude them from crack detection could make the proposed method more practical.

Figure 12 shows a comparison of the estimated crack lengths obtained using the proposed method with the ground truth values obtained through direct human visual measurement. The black dashed line in the figure represents the ideal case, in which the estimated and ground truth values are the same. Points below this line indicate under-detection (estimated length shorter than ground truth), while points above the line indicate over-detection (estimated length longer than ground truth). The results demonstrate a strong correlation between the estimated and ground truth values, with most values closely matching. However, the estimated lengths tended to be slightly smaller than the ground truth. This discrepancy may be attributed to the inability to fully detect very fine cracks with small widths. The influence of crack width on detection accuracy remains a subject for future investigation. Among the 300 images evaluated in this study, 225 were identified as containing cracks based on ground truth measurements. Approximately 4.9% of these (11 out of 225) were completely undetected by the proposed method, resulting in an estimated length of 0 mm. For cases where the ground truth crack length exceeded 120 mm, the presence of cracks was consistently detected, although some variation in length estimation was observed. In images where the ground truth was 0 mm, over-detection occurred in some cases, with the maximum estimated crack length reaching approximately 100 mm. However, the average estimated length for these cases was 15.7 mm, and in about 63% of them (47 out of 75), the estimated length was also 0 mm. It should also be noted that in some sleepers, cracks extended beyond the design shoulder length (250 mm at the center), which is likely due to crack curvature or the presence of multiple cracks.

Figure 13 illustrates the frequency distribution of errors which is defined as the difference between estimated value and ground truth value. Figure 14 shows the cumulative frequency of the absolute error rate, which is defined as the absolute value of the difference between the estimated value and ground truth values divided

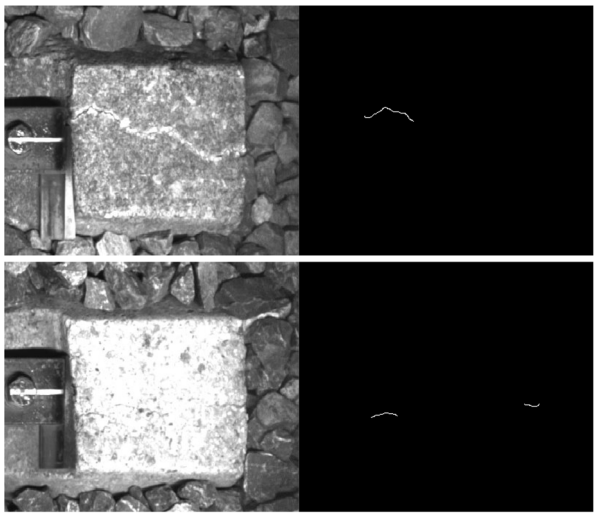

Fig.10 Example of crack extraction result (with under-detection)

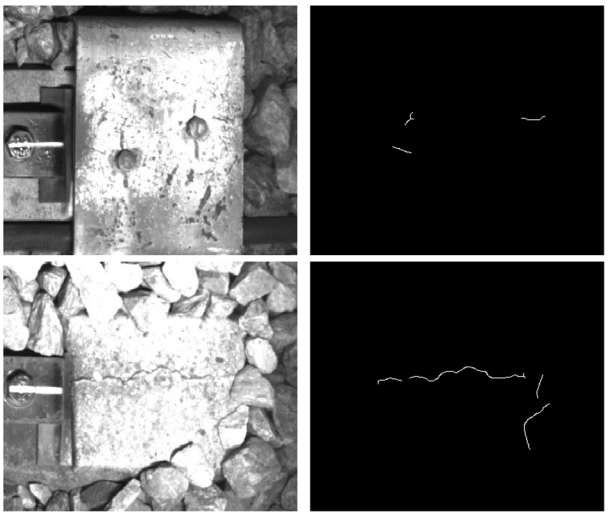

Fig. 11 Example of crack extraction result (with over-detection)

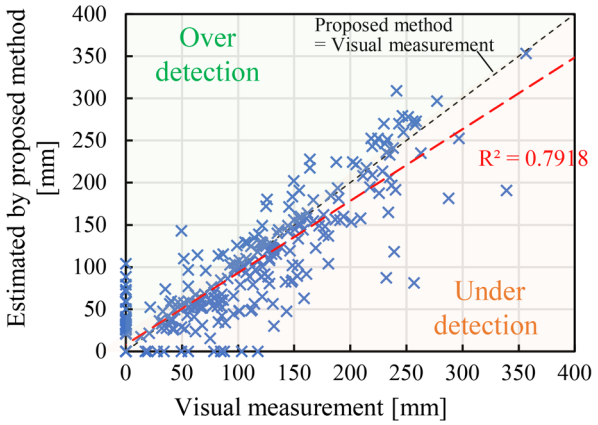

Fig. 12 Comparison of crack lengths estimated by proposed method and by visual measurement

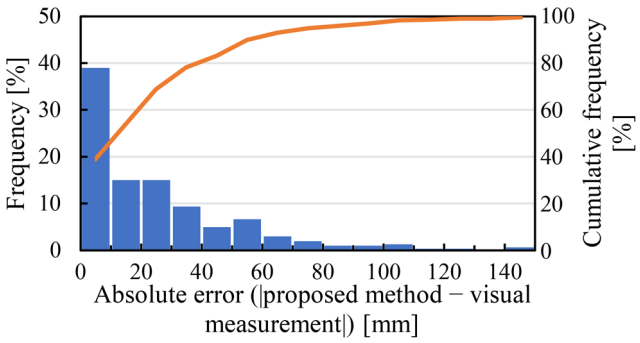

Fig. 13 Frequency distribution of errors between proposed method and visual measurement

by ground truth value. To prevent divergence, cases with ground truth crack lengths close to zero were excluded from the error rate calculation. Only cracks exceeding a certain length (between 50 and 200 mm) were considered. From these figures, it was found that approximately 39% of the validation data exhibited errors within ±10 mm, 54% within ±20 mm, and 69% within ±30 mm. Regarding the error rates, about 60% of cases with ground truth lengths of 50 mm or more and about 75% of cases with lengths of 200 mm or more fell within 20%. This suggests that the proposed method can accurately estimate crack lengths, particularly for longer cracks. Although some cases showed errors exceeding 100 mm, it should be noted that the loss of functionality in a single prestressed concrete sleeper does not compromise train running safety as long as adjacent sleepers remain intact. Therefore, the proposed method is considered suitable for practical applications such as screening sleepers requiring attention and verifying crack occurrence conditions in the field.

4. Examination of applicability of proposed method

4.1 Method of examination

As discussed in Chapter 3, the proposed method has the potential to confirm the presence of cracks in prestressed concrete sleepers. This chapter examines the applicability of the method by applying it to images taken on an actual operating line to verify the occurrence of cracks in prestressed concrete sleepers. The total length of the target line section is 37 km. While the target section is a double-track segment, this study focused on one of the tracks. Specifically, cracks that occurred on the right-side FC area (right shoulder section) of the prestressed concrete sleepers were investigated, and a survey was conducted regarding their occurrence locations and lengths.

4.2 Identification of crack occurrence locations on prestressed concrete sleepers

Figure 15 shows the locations and frequencies of crack occurrences. This study uses image data that include variations in the positions of the prestressed concrete sleepers within the captured images. To identify where cracks occurred on the sleepers, image alignment was first performed. Figure 15(a) shows the result of averaging all images after alignment. From this figure, the shapes of the prestressed concrete sleepers and the rail fastening systems can be clearly recognized even in the averaged image, indicating that the alignment was appropriately carried out. Figure 15(b) shows the image in Fig. 15(a) overlaid with a diagram representing the frequency of crack occurrences. In this figure, the frequency of crack occurrences per 5 × 5 pixels was normalized so that the maximum frequency of 11% corresponds to the upper limit, and the values were represented in 255 gradations. Areas with darker red indicate higher frequencies of crack occurrence.

Some cracks were detected on the ballast, which were false detections of either the ballast itself or the boundary between the ballast and the prestressed concrete sleeper. The detected cacks in the ballast considered to be false detections were negligible compared to the cracks on the top surface of the sleeper, suggesting that the likelihood of the ballast being falsely detected as cracks by this method is low. Additionally, cracks were found to occur frequently near the rail fastening systems around the center of the sleeper in the rail direction. Thus, under the conditions of the target line section and the imaging setup in this study, the proposed method made it possible to identify the tendency for cracks to occur in locations on the top surface of prestressed concrete sleepers.

4.3 Identification of crack occurrence conditions on an actual line section

Figure 16 shows the distribution of crack lengths and number of cracks that occurred on the right shoulder section of prestressed concrete sleepers in the target line section. Approximately half of the cracks in this section were 80 mm or shorter, while about 3.3% of the sleepers exhibited cracks of 240 mm or longer, which are considered to extend across almost the entire shoulder section.

Figure 17 shows the number of prestressed concrete sleepers with cracks per kilometer in the target line section. As can be seen in the figure, cracked sleepers were not distributed uniformly throughout the section but were concentrated in specific areas. In particular, many cracked sleepers were found around the kilometerage of 3 km

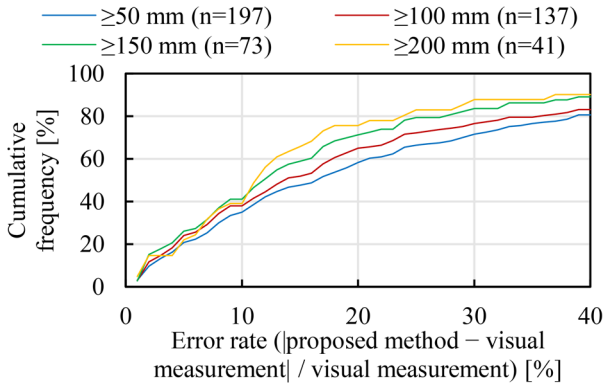

Fig. 14 Cumulative frequency distribution of error rates

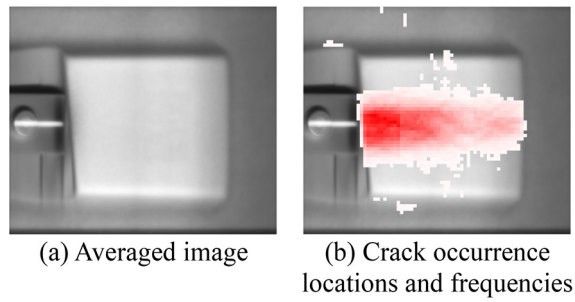

Fig. 15 Crack occurrence locations and frequencies

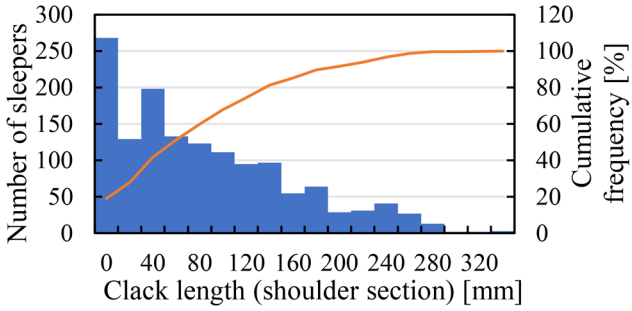

Fig. 16 Distribution of crack lengths and occurrence counts

to 4 km within the target line section. Note that the kilometer markers in the figure are displayed with the starting point of the target section set to 0 km, and they do not correspond to the actual kilometer markers used for line management.

Figure 18 shows the maximum and average crack lengths per kilometer. Unlike the number of cracked sleepers per kilometer, most sections with cracked sleepers exhibited a maximum crack length of approximately 250 mm. Similarly, the average crack length was approximately 80 mm. Overall, these examples show that the proposed method can capture trends in crack lengths on an actual line section.

5. Conclusions

This study proposed a method for detecting cracks in prestressed concrete sleepers and estimating their lengths using deep learning to improve the efficiency of maintenance for cracked sleepers. The applicability of the proposed method was also examined. The main findings are as follows:

1. Semantic segmentation was employed as a method for extracting cracks in prestressed concrete sleepers. Cracks were detected in images captured by maintenance vehicles and a technique was introduced to estimate crack positions and lengths. This was achieved by removing false detections through binarization and thinning processing.
2. It was confirmed that the proposed method can effectively reduce the number of false detections of ballast and rail fastening systems and accurately identify crack occurrence positions and lengths. Furthermore, the validation results showed that approximately 75% of cases where crack lengths exceeded 200 mm had an error rate of 20% or less. This indicates that the method can estimate crack lengths with reasonable accuracy, particularly for sleepers with long cracks.

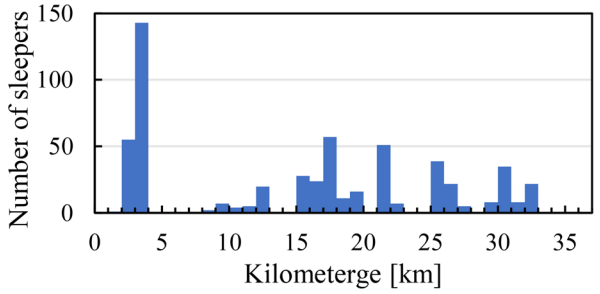

Fig. 17 Number of prestressed concrete sleepers with crack (per 1 km)

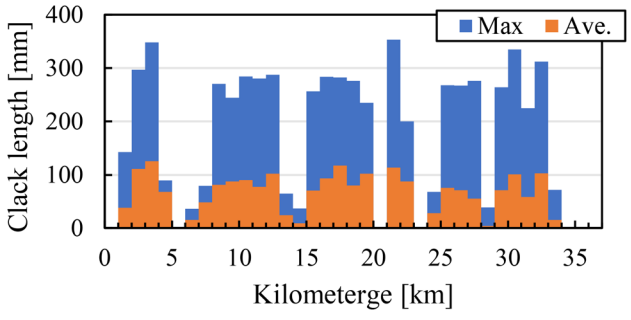

Fig. 18 Maximum and average crack length per 1 km

3. The applicability of the proposed method was examined using images obtained from an actual railway line with a total length of 37 km. The results showed that approximately half of the cracks were 80 mm or less in length, and that about 3.3% of sleepers had cracks that extended across the entire shoulder section. Additionally, cracks tended to occur in specific sections of the line rather than being uniformly distributed. Under the conditions of the target line section and imaging setup, the proposed method made it possible to identify trends in crack lengths and their occurrence positions, suggesting that it could be used to screen and assess the crack conditions of prestressed concrete sleepers.

In future work, we plan to improve the accuracy of detection by increasing training data and incorporating functions that remove error-prone data in advance. We also intend to examine applicability under different line sections and imaging conditions to those used in this study. Furthermore, we will also work on proposing more appropriate health assessment criteria and deepening our understanding of phenomena such as the relationship between crack length and factors like alkali–silica reaction. This will help us to address cases where multiple damage modes occur simultaneously.

References

[1] Minoura, S., Watanabe, T., Suzuki, D. and Uehan, F., "Study on wear characteristics of prestressed concrete sleepers in service and their influence on load-bearing capacity," *Proceedings of the Japan Concrete Institute*, Vol. 37, No. 2, pp. 1345-1350, 2015 (in Japanese).

[2] Minoura, S., Watanabe, T., Iijima, T. and Ishida, T., "Field survey and study on health assessment criteria for prestressed concrete sleepers damaged by frost," *Proceedings of the Japan Concrete Institute*, Vol. 42, No. 1, pp. 665-670, 2020 (in Japanese).

[3] Minoura, S., Watanabe, T., Matsuoka, K. and Goto, K., "Study on health assessment method focusing on vibration characteristics of prestressed concrete sleepers damaged by frost," *Proceedings of the Japan Concrete Institute*, Vol. 43, No. 1, pp. 616-621, 2021. (in Japanese).

[4] Watanabe, T., Goto, K., Minoura, S., and Ikeda, M., "Actual Condition Survey of the Effects of Aging and Accumulated Tonnage on the Load-bearing Capacity of PC Sleepers," *Quarterly Report of RTRI*, Vol. 65, pp. 55-60, 2024.

[5] Nakamura, T., and Tabuchi, T., "Current condition assessment of prestressed concrete sleepers," *Proceedings of the 68th Annual Conference of the Japan Society of Civil Engineers*, vol. 68, no. VI-521, pp. 1041-1042, 2013 (in Japanese).

[6] Sue, M., Okumura, Y. and Hori, Y., "Study on deterioration condition of existing prestressed concrete sleepers," *Jointed Railway Technology Symposium*, vol. 21, no. S2-4-6, 2014 (in Japanese).

[7] Minoura, S., Watanabe, T., Inoue, H. and Katayama, Y., "Health assessment of prestressed concrete sleepers with longitudinal cracks," *Proceedings of the Japan Concrete Institute*, vol. 38, no. 2, pp. 1585-1590, 2016 (in Japanese).

[8] Aoshima, W., Yamamoto, T., Nakano, S. and Nakamura, H., "Detection of Deterioration Area on Concrete Surface Using Segmentation Method by Deep Learning," *Intelligence, Informatics and Infrastructure*, Vol. 1, No. J1, pp. 481-490, 2020 (in Japanese).

[9] Fujita, Y., Kobayashi, K. and Hamamoto, Y., "Improvement of

Efficiency and Precision of Crack Extraction Method Using Deep Learning Models," *Journal of Japan Society of Civil Engineers, Ser. F3 (Civil Engineering Informatics)*, Vol. 77, No. 1, pp. 13-41, 2021 (in Japanese).
[10] Minoura, S. and Watanabe, T., "Fundamental Study on Crack Detection Method for PC Sleepers Using Deep Learning Model," *Intelligence, Informatics and Infrastructure*, Vol. 4, No. 3, pp. 285-292, Sept. 2023 (in Japanese).
[11] Badrinarayanan, V., Kendall, A. and Cipolla, R., "Segnet: A deep convolutional encoder-decoder architecture for image segmentation," *IEEE Transactions on Pattern Analysis and Machine Intelligence*, Vol. 39, No. 12, pp. 2481-2495, 2017.
[12] Ronneberger, O., Fischer, P. and Brox, T., "U-Net: Convolutional Networks for Biomedical Image Segmentation," *Medical Image Computing and Computer-Assisted Intervention* - MICCAI 2015, Vol. 9351, pp. 234-241, 2015.
[13] Ioffe, S. and Szegedy, C., "Batch normalization: accelerating deep network training by reducing internal covariate shift," *Proc. of the 32nd Int. Conf. on Machine Learning (ICML)*, Vol. 37, pp. 448-456, 2015.
[14] Zhang, T. Y. and Suen, C. Y., "A fast parallel algorithm for thinning digital patterns," *Communications of the ACM*, Vol. 27, No. 3, pp. 236-239, 1984.

Authors

Shintaro MINOURA, Dr.Eng.
Senior Researcher, Track Dynamics Laboratory, Railway Dynamics Division
Research Areas: Concrete Sleeper, Numerical Simulation, Image Analysis,

Tsutomu WATANABE, Dr.Eng.
Senior Chief Senior Chief Researcher, Track Dynamics Laboratory, Railway Dynamics Division
Research Areas: Structure-borne Noise, Vibration, Concrete Sleeper, Numerical Simulation

Validation of Natural Frequency Identification Method for Individual Bridges and Viaducts, Excluding the Effects of Adjacent Structures

Kazunori WADA **Kimitoshi SAKAI**
Structural Dynamics and Response Control Laboratory, Center for Railway Earthquake Engineering Research

The natural frequency of railway bridges and viaduct groups is used as an integrity assessment index for substructures. However, this may include the effects of vibrations of adjacent structures, and there is a possibility that the vibration characteristics cannot always be evaluated clearly. From this reason, the authors theoretically derived a method for identifying the natural frequency of individual bridges and viaducts, using the natural frequency and natural mode of the entire structure evaluated by microtremor observation. In this paper, we verified the applicability of the proposed method to railway bridges and viaducts by conducting a 3D dynamic analysis based on real structures and measurements. The result showed that the natural frequency of the substructure could be identified with an error of about 10%. Therefore, by identifying the natural frequency of the substructure using the proposed method, it is possible to improve the integrity assessment of structures after an earthquake.

***Key words*:** *individual structure, natural frequency, identification, railway bridges and viaducts*

1. Introduction

Railway bridges and viaducts are composed of multiple structural units connected in series via girders and bearings, so the vibration characteristics such as natural frequencies obtained from vibration measurements are values for the entire structural system, including the influence of the vibrations of adjacent structures. This is clear from research examples such as the comparison of actual measurement results between individual piers and entire structural systems on road bridges [1] and actual measurements and analytical studies on the interaction of groups of railway structures [2]. In this paper, the term "individual structure" refers to the pier and foundation structure of a bridge, and the slab, columns, and foundation structure of a rigid-frame viaduct (Fig. 1(a)).

To date, the structural soundness of an entire structure has been assessed using its vibration characteristics obtained through vibration measurements. In the railway industry in particular, impact vibration testing [3, 4] has been used for many years to assess the soundness of bridges and viaducts: applying impact vibration to the structure of interest and evaluating the natural frequency of the entire structure from the obtained waveform, enables assessment of the soundness of the foundation structure. Since damage or a decrease in stability of an individual structure leads to a decrease in the natural frequency of the entire structure, this method can be considered an effective nondestructive testing method. However, when the vibration characteristics of adjacent structures differ significantly, the coupling effect between the structures becomes dominant, and the impact of local damage to an individual structure on the change in the natural frequency of the entire structure is limited, making it impossible to clearly evaluate the characteristics of the individual structure. Based on the above background, the authors theoretically derived a method for identifying the natural frequency of an individual structure from the natural frequency and/or natural mode of the entire structure [5, 6]. This was done using a mass-spring model to represent bridges and viaducts, in which multiple structural units are connected via girders and bearings (Fig. 1). By establishing this method, when a deterioration in the soundness of a foundation structure is suspected due to, for example, an earthquake or scouring of a river bridge pier, the natural frequency of the individual structure may be used as a new indicator for determining the soundness of the foundation structure. This allows a more direct and accurate determination of the soundness of the foundation structure than the indicator used in impact vibration tests (the first-order natural frequency of the entire system).

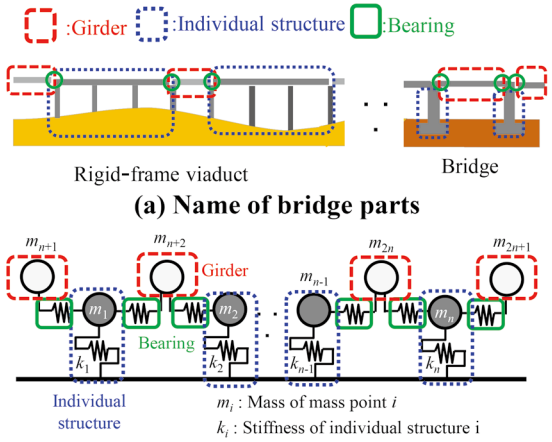

Fig. 1 Image of the target railway bridge/viaduct

Previous studies [5, 6] confirmed the validity of the proposed method using the spring-mass model shown in Fig. 1(b), but the validity of the method that takes into account the behavior of actual girders or rigid-frame viaducts with many degrees of freedom in the bridge axial direction has not been fully confirmed. In addition, there is a possibility that the modal parameters (natural frequencies and natural modes) of the entire structural system required for the proposed method can be calculated by conducting earthquake observations and microtremor observations using sensors placed at multiple points on railway bridges and viaducts, and applying the frequency domain decomposition (FDD) method [7] to the obtained response waveforms. However, no studies incorporating such actual measurements and actual structures have been conducted.

Therefore, as a basic study prior to verifying the applicability of the proposed method to actual structures, the authors analytically confirmed the validity of the proposed method under conditions

simulating actual measurements of actual structures [8]. In this paper, we conducted a dynamic analysis by inputting white noise simulating microtremors into a 3D frame model of a group of railway bridges and viaducts, and applied the FDD method [7] to the response waveforms obtained from the dynamic analysis to identify the natural frequencies of individual structures using the proposed method.

2. Overview of method for identifying natural frequency of an individual structure

This chapter overviews the natural frequency identification method proposed in references [5, 6]. The proposed method is based on the following assumptions:

- Bridges and viaducts behave elastically;
- Frequency dependence of stiffness is not considered;
- Damping is assumed to be proportional, such as Rayleigh damping.

The damped free vibration problem of the mass-spring model of n individual structures shown in Fig. 1(b) is considered. The equations of motion for this problem are as follows:

$$\boldsymbol{M}\ddot{\boldsymbol{X}}(t)+\boldsymbol{C}\dot{\boldsymbol{X}}(t)+\boldsymbol{K}\boldsymbol{X}(t)=0 \quad (1)$$

where $\boldsymbol{M}$ is the mass matrix, $\boldsymbol{C}$ is the damping matrix, $\boldsymbol{K}$ is the stiffness matrix, and $\boldsymbol{X}(t)$ is the displacement vector of each mass point. Assuming a harmonic vibration solution as the solution to the above equation, $\boldsymbol{X}(t)$ can be expressed in the following form.

$$\boldsymbol{X}(t)=\{r_1 \quad r_2 \quad \cdots \quad r_{2n+1}\}^T e^{\lambda t \pm j\phi},\ \lambda=-\sigma \pm j\omega_D \quad (2)$$

where j is an imaginary unit. λ is an eigenvalue, expressed as the damped natural circular frequency ωD of the entire structure and the modal damping constant σ. r_1 to r_{2n+1} are the displacement amplitudes. ϕ is the phase angle. If you substitute (2) into (1) and rearrange it, the following equation is obtained:

$$\sum_{i=1}^{n}(\lambda C_i+\Omega_i^2)M_iR_i=-\lambda^2\sum_{i=1}^{2n+1}M_iR_i \quad (3)$$

where the symbols represent the following:

$$C_i=\frac{c_i}{m_i},\ \Omega_i^2=\frac{k_i}{m_i},\ M_i=\frac{m_i}{m_l},\ R_i=\frac{r_i}{r_l} \quad (4)$$

where l is the subscript of the individual structure in question. Note that Ω_i corresponds to the natural circular frequency of the i-th structure. Substituting λ expressed in (2) into (3) gives a complex equation, and if the condition that the real part = imaginary part = 0, which is the condition for this equation to hold, is applied, the following equation holds for the j-th mode:

$$\sum_{i=1}^{n}\Omega_i^2M_iR_{ji}=\omega_j^2\sum_{i=1}^{2n+1}M_iR_{ji} \quad (5)$$

In rearranging the above equation, regarding the j-th order damped circular frequency ωD_j and modal damping constant σ_j, the following conversion using the undamped circular frequency ω_j and damping constant h_j is applied:

$$\sigma_j=h_j\omega_j,\ \omega_{Dj}=\omega_j\sqrt{1-h_j^2} \quad (6)$$

Looking at (5), there are n unknowns, $\Omega_i\,(i=1, 2, ..., n)$, and the mass ratio M_i can be calculated from design documents, etc. Therefore, if n pairs of undamped natural circular frequencies ω_j and natural modes R_{ji} can be evaluated in some way, the natural circular frequency Ω_i of structure unit i can be found. Note that, for the damping constants (a few percent) typically assumed for bridges and viaducts, it has been confirmed separately that replacing the undamped natural circular frequency with the damped natural circular frequency has little effect on identification accuracy [5].

3. Validation of the proposed method assuming a real structure

In this chapter, we analytically verify the validity of the proposed method under conditions simulating microtremor observations of an actual structure. First, we provide an overview of the analytical model and dynamic analysis, taking into account the correspondence between the actual structure and measurements. Next, we treat the analytical results as actual measurement data and evaluate the modal parameters required to apply the proposed method using the FDD method [7]. Finally, we identify the natural frequencies of the structure itself using the proposed method and compare them with the correct values.

3.1 Overview of the analysis model

Figure 2 shows the 3D framework model of the railway bridge and viaduct group used for validation. The group consisted of three spread-foundation rigid-frame viaducts (R1 to R3), one pier (P1), and three adjustable girders (Ct1 to Ct3). For convenience, the analytical model in this study did not consider the influence of the girders at the start of R1 and the end of P1, but they could also be considered as concentrated masses. Columns, beams, piers, and girders were all modeled using linear beam elements, while the ground resistance and the resistance of the bearings in the bridge axis direction and the direction perpendicular to bridge axis were modeled using linear spring elements. Here, ground resistance was calculated based on the "Design Standards for Railway Structures and Commentary (Foundation Structures)" [9] and assumed sand and gravel with a shear wave velocity of 400 m/s. The stiffness of the movable bearings was set to the shear stiffness of a typical rubber bearing, while the stiffness of the fixed bearings was set to a sufficiently large value. Note that while an actual structure includes the effects of the track structure (rails and track slabs) and stopper restraints, this effect is not taken into account in this analysis model.

The structural specifications of this model are shown in Tables 1 and 2. The natural frequencies, stimulation coefficients, and effective mass ratios of the entire structure obtained by eigenvalue analysis are shown in Table 3. The table also lists the mode orders in the bridge axis direction and the direction perpendicular to bridge axis determined from the stimulation coefficients. For this model, we attempt to identify the natural frequencies of each individual structure (Ω_i in (4) divided by 2π).

The correct values for the natural frequencies of each individual structure were calculated by constructing individual models from the model in Fig. 2, excluding the girders and bearings, and conducting eigenvalue analysis. As an example, the individual-structure

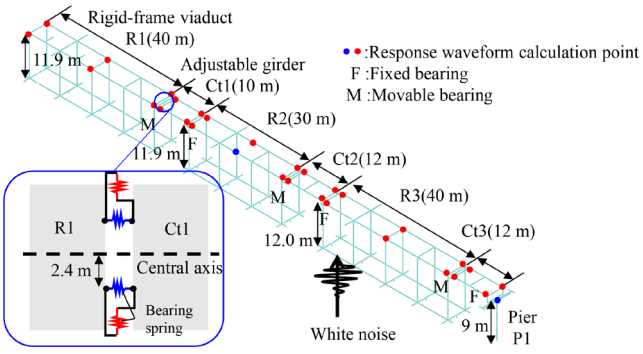

Fig. 2 Analysis of frame models simulating actual measurements

model of rigid-frame viaduct R1 is shown in Fig. 3, with the results of the eigenvalue analysis shown in Table 4 and the first modes in the bridge axis direction and the direction perpendicular to bridge axis shown in Fig. 4. These figures show that in the individual-structure model, there is only one mode with significant values for the stimulation coefficient and effective mass ratio in each of the bridge axis direction and the direction perpendicular to bridge axis. The natural frequency corresponding to this mode was considered to be the natural frequency of the individual structure to be identified using the proposed method. The natural frequencies of each individual structure in the bridge axis direction and the direction perpendicular to bridge axis calculated using the same procedure are shown in Table 5.

3.2 Overview of dynamic analysis

To simulate microtremors, a dynamic analysis was conducted using white noise with a constant Fourier amplitude characteristic. The input was provided as an acceleration waveform to the base where the soil spring of the spread foundation is connected. The input direction was either perpendicular to bridge axis or along the bridge axis.

The output points of the response acceleration waveform are the red and blue dots in Fig. 2. These correspond to the locations where microtremor meters are expected to be installed in an actual structure, but for rigid-frame viaducts and adjustable girders, as will be described later, the response changes in the bridge axis direction due to the influence of rotation around the vertical direction at the bearing, so it is necessary to install microtremor meters at the end points, and evaluation points were set accordingly.

The FDD method [7] is applied to the obtained response acceleration waveform to evaluate the modal parameters (natural frequencies and natural modes) of the entire structure, and these are used to identify the natural frequencies of each individual structure using (5). Note that since this model has four individual structures, four sets of modal parameters are required from (5). These correspond to the first to fourth modes in the bridge axis direction and the direction perpendicular to bridge axis shown in Table 3.

Figure 5 shows examples of results obtained from dynamic analysis. These figures show the Fourier amplitude ratios (Fourier amplitude of response waveform/Fourier amplitude of input wave) of accelerations at the midpoints of each rigid-frame viaduct and at the tops of the piers (blue dots in Fig. 2) when white noise is applied perpendicular to the bridge axis. In the figures, the frequency bands corresponding to the natural frequencies of the individual structures listed in Table 5 are indicated by black dotted lines. Looking at these figures, it is clear that there is no clear change in the Fourier amplitude ratio, particularly for R2 and P1, near the natural frequencies of the individual structures. This is inferred to be because there are R1 and R3, which have larger masses than R2, at the start and end points of R2, and there is R3, which has a larger mass than P1 at the start point of P1, suggesting that R2 and P1 are particularly strongly affected by the coupling effect with adjacent structures. This demonstrates the difficulty of evaluating the natural frequencies of individual structures by analyzing only the response waveforms, providing confirmation of the validity of the proposed method for such problems.

Table 1 List of structural specifications

Parts	Dimensions, rigidity
Rahmen column (L×C)	0.9 m×0.9 m
Upper longitudinal beam (width×thickness / w×t)	0.8 m×1.3 m
Upper horizontal beam (w×t)	1.0 m×1.4 m
Underground longitudinal beam (w×t)	0.6 m×1.4 m
Underground horizontal beam (w×t)	3.0 m×1.4 m
Adjustable beam (w×t)	1.4 m×1.0 m
Pier column (L×C×H)	1.9 m×4.5 m×7.0 m
Pier beam (L×C×H)	1.9 m×9.2 m×2.2 m
Pier footing (L×C×H)	6.5 m×8.0 m×1.9 m
Fixed bearing stiffness	1.0×10^{8} kN/m
Moveable bearing stiffness	6.1×10^{3} kN/m

Table 2 Weight of each structure

Structure	R1	R2	R3	P1	Ct1	Ct2	Ct3
Weight (kN)	9,287	6,875	9,287	1,382	1,666	2,002	2,125

Table 3 List of eigenvalue analysis results for bridges/viaducts

Order	Natural frequency (Hz)	Excitation coefficient			Effective mass ratio			Remarks
		Bridge axis	Bridge axis perp	Vertical	Bridge axis	Bridge axis perp	Vertical	
1	1.71	0.00	1.39	0.00	0.00	0.48	0.00	Bridge axis perp 1st
2	1.76	0.03	−0.38	0.00	0.00	0.02	0.00	
3	1.79	0.01	0.87	0.00	0.00	0.16	0.00	Bridge axis perp 2nd
4	1.85	1.24	0.00	0.00	0.61	0.00	0.00	Bridge axis 1st
5	1.99	0.28	−0.01	0.00	0.05	0.00	0.00	Bridge axis 2nd
6	2.05	−0.01	0.74	0.00	0.00	0.04	0.00	Bridge axis perp 3rd
7	2.14	0.35	0.01	0.00	0.04	0.00	0.00	Bridge axis 3rd
8	2.93	0.96	0.01	0.05	0.07	0.00	0.00	Bridge axis 4th
9	4.66	−0.01	1.19	0.01	0.00	0.07	0.00	Bridge axis perp 4th
10	5.76	0.00	0.04	0.00	0.00	0.00	0.00	

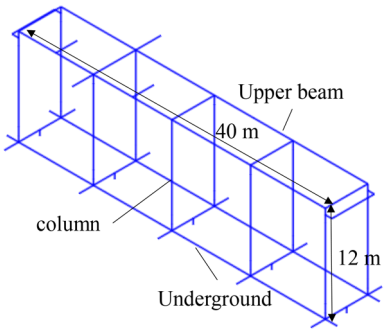

Fig. 3 3D frame model of rigid-frame viaduct R1

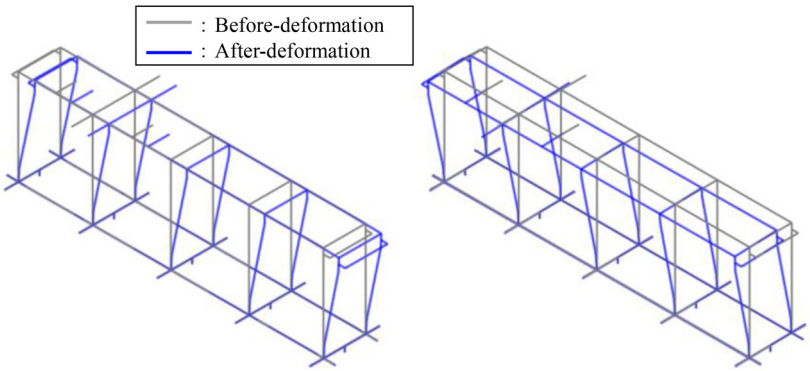

(a) Bridge axis direction 1st **(b) Bridge axis perp direction 1st**

Fig. 4 Natural modes of rigid-frame viaduct R1 (3D frame model)

Table 4 List of eigenvalue analysis results for rigid-frame viaduct R1 (3D frame model)

Order	Natural frequency (Hz)	Excitation coefficient			Effective mass ratio			Remarks
		Bridge axis	Bridge axis perp	Vertical	Bridge axis	Bridge axis perp	Vertical	
1	1.91	0.00	1.05	0.00	0.00	0.73	0.00	Bridge axis perp 1st
2	1.99	1.02	0.00	0.00	0.74	0.00	0.00	Bridge axis 1st
3	2.24	0.04	0.06	0.00	0.00	0.00	0.00	
4	14.16	0.00	0.02	0.01	0.00	0.00	0.00	
5	15.00	0.01	0.00	1.77	0.00	0.00	0.59	Vertical 1st

Table 5 List of natural frequencies of each structure

Structure	Viaduct R1		Viaduct R2		Viaduct R3		Pier P1	
Direction	Bridge axis perp	Bridge axis	Bridge axis perp	Bridge axis	Bridge axis perp	Bridge axis	Bridge axis perp	Bridge axis
Natural frequency	1.91 Hz	1.99 Hz	2.22 Hz	2.29 Hz	1.89 Hz	1.96 Hz	6.46 Hz	4.82 Hz

3.3 Evaluation of modal parameters using FDD method

Figure 6 shows the frequency distribution of the first-order singular value calculated by applying the FDD method to the response acceleration waveform obtained from the dynamic analysis described in Section 3.2. Several peaks can be seen in this figure in each direction. Figure 7 shows the results of comparing these dominant frequencies with the natural frequencies of the first to fourth modes of the overall structure in the bridge axis direction and the direction perpendicular to bridge axis shown in Table 3. As shown in this figure, it can be confirmed that the frequencies calculated using the FDD method [7] match the natural frequencies of each major mode of the overall structure.

Figure 8 shows the first and second modes in the bridge axis direction and the direction perpendicular to bridge axis as examples of eigenmodes evaluated at each predominant frequency. This figure also shows the eigenmode shapes obtained by eigenvalue analysis. It also shows that the mode shapes evaluated using the FDD method [7] generally match well with the mode shapes obtained from eigenvalue analysis. However, there is some deviation between the two, for example, around 80 m along the bridge axis for the second mode in the direction perpendicular to bridge axis. This is inferred to be because bridges and viaducts have complex mode shapes that rotate around the vertical axis at their movable bearings, and this is the area where the impact of this rotation is particularly large.

From the above, we were able to roughly evaluate the modal parameters (natural frequencies and eigenmodes) by processing the results of dynamic analysis assuming microtremor observations.

3.4 Identification of natural frequencies of an individual structure using the proposed method

Figure 9 shows the results of identifying the natural frequencies of each individual structure using (5) of the proposed method from the natural frequencies and natural modes estimated by the FDD method [7]. In this figure, the results of eigenvalue analysis of each individual structure are compared to the true value. This figure also shows that the natural frequencies of each individual structure in the direction of the bridge axis and the direction perpendicular to bridge axis were estimated with an error of about 10%. One possible cause of the error is inferred to be the influence of the estimation error of the natural modes mentioned in Fig. 8 and the influence of ignoring the rotational behavior around the vertical axis in the model shown in Fig. 1.

In addition, in conventional structural integrity assessment methods a structural integrity is deemed to be at its lowest when the natural frequency obtained through actual measurements is more than 30% lower than the standard natural frequency [3]. Therefore,

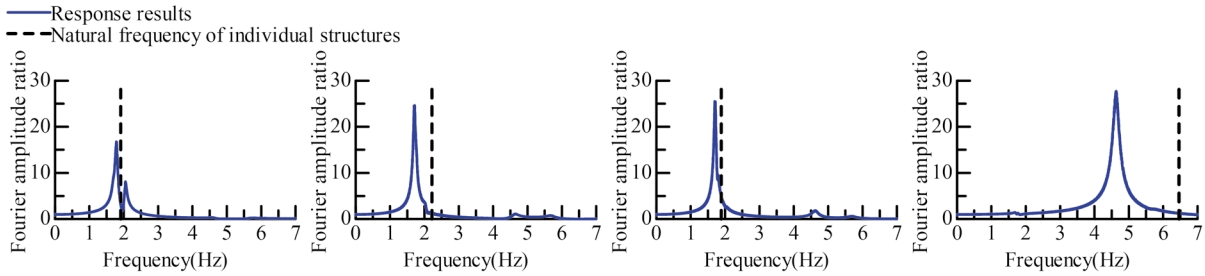

(a) Rigid-frame viaduct R1 (b) Rigid-frame viaduct R2 (c) Rigid-frame viaduct R3 (d) Pier P1

Fig. 5 Fourier amplitude ratio at top of structure based on dynamic analysis results

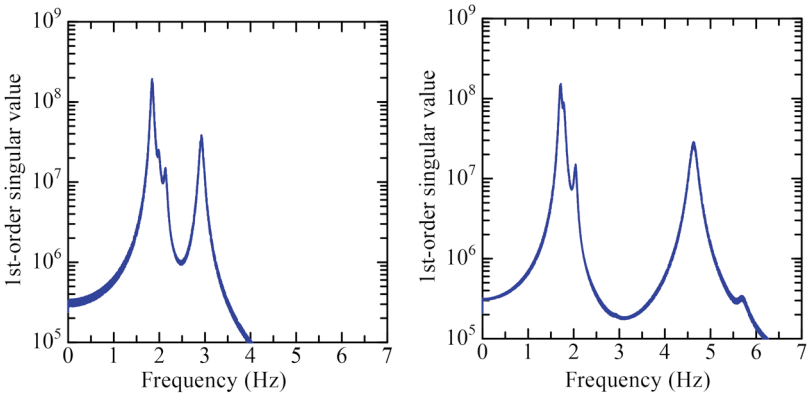

(a) Bridge axis (b) Perpendicular to bridge axis

Fig. 6 1st-order singular value distribution

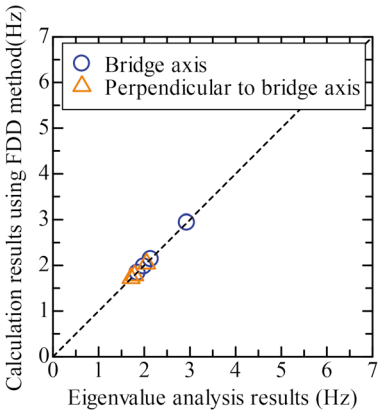

Fig. 7 Natural frequency evaluation results of the entire structure system

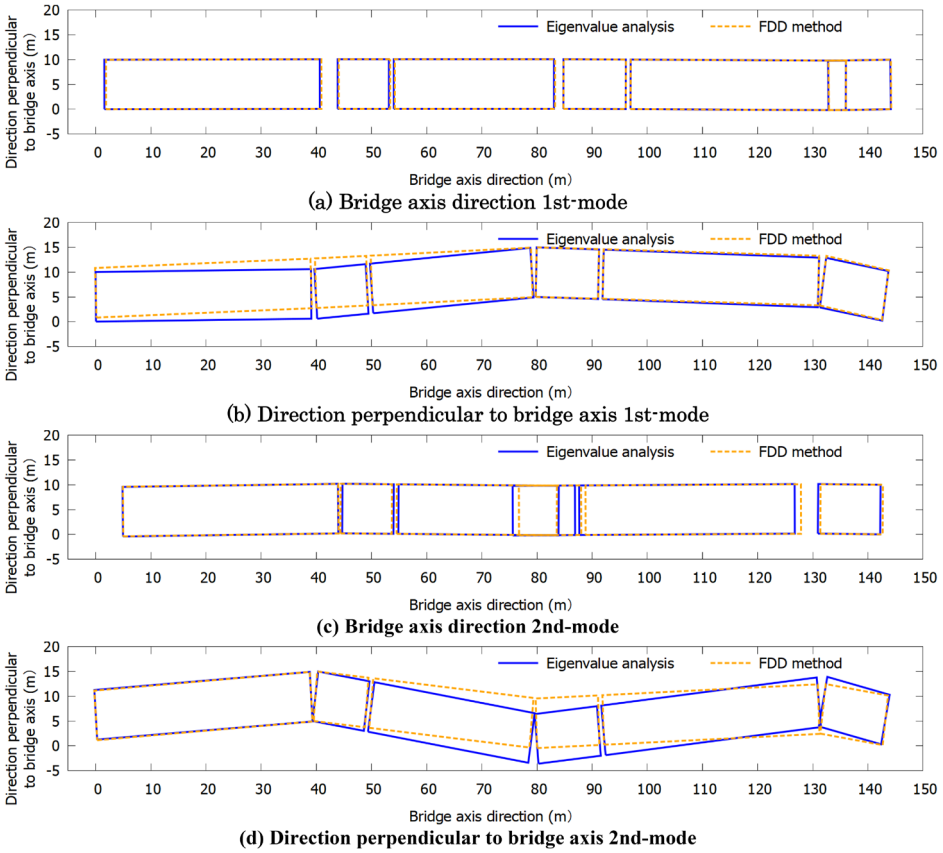

(a) Bridge axis direction 1st-mode

(b) Direction perpendicular to bridge axis 1st-mode

(c) Bridge axis direction 2nd-mode

(d) Direction perpendicular to bridge axis 2nd-mode

Fig. 8 Natural mode evaluation results

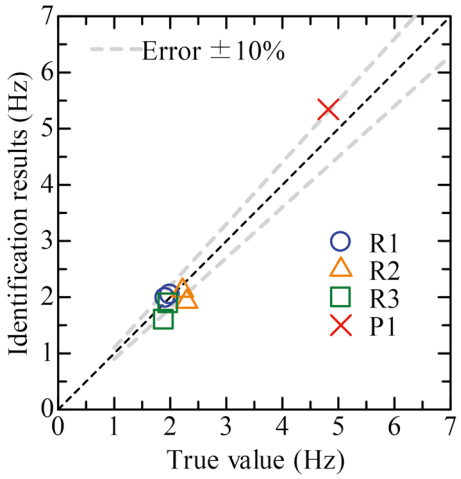

Fig. 9 Natural frequency identification results of individual structures

even if the influence of the error (10%) of the proposed method identified in this paper is taken into account, we consider that the proposed method would be fully applicable. Furthermore, in terms of maintenance, it is important to understand the change in natural frequency over time. From this perspective as well, the proposed method is likely to be applicable regardless of the error mentioned above.

4. Conclusion

In this paper, we conducted linear dynamic analysis of a 3D frame model of a group of railway bridges and viaducts of spread foundation type, in which white noise simulating microtremors was applied as input. We then applied the FDD method [7] to the response acceleration waveforms obtained from this analysis to evaluate the modal parameters and attempted to identify the natural frequencies of the individual structures using the proposed method [5, 6]. The findings are as follows:

- The natural frequencies and modal parameters of natural modes evaluated by applying the FDD method to the dynamic analysis results of a 3D frame model can generally reproduce the correct values evaluated by eigenvalue analysis.
- Based on the evaluated modal parameters, the proposed method can identify the natural frequencies of the individual structures with an error of approximately 10% relative to the true values.

We plan to further verify the applicability of the proposed method by analyzing actual measurement data. Since the applicability and accuracy of the results may vary depending on factors such as ground conditions, foundation type, bearing conditions, and the number of consecutive bridges and viaducts, it is also important to understand the scope of application. For example, this paper focuses on structures of spread foundation type. However, structures of pile foundation type on soft ground may experience significant displacement of the foundation structure, and applicability of this method under such conditions remains to be confirmed. Furthermore, practical application of this method requires microtremor observations of a group of bridges and viaducts. However, microtremor meters are small and highly portable, making them easier to use than impact vibration tests, which are cumbersome to transport and set up, with a striking weight of approximately 30 kg. Therefore, once this method is established, it will become possible to assess the integrity of foundation structures more directly and accurately using a simpler method than impact vibration tests.

References

[1] Nakajima, A., Nakano, K. and Nakamura, S., "Vibrational property of independent piers and completed bridge by using microtremor measurement," *Journal of Structural Engineering*, Vol. 56A, pp. 305-314, 2010 (in Japanese).
[2] Tokunaga, M., Sogabe, M., Tanimura, H. and Ono, K., "Method for evaluating equivalent natural period with microtremor measurement," *Proceedings of JSCE* A1, Vol. 71, No. 1, pp. 72-86, 2015 (in Japanese).
[3] Nishimura, A. and Tanamura, S., "A study on integrity assessment of railway bridge foundation," *RTRI Report*, Vol. 3, No. 8, pp. 41-49, 1989 (in Japanese).
[4] Nishimura, A., "A study on integrity assessment of railway rigid frame bridge," *RTRI Report*, Vol. 4, No. 9, pp. 14-21, 1990 (in Japanese).
[5] Wada, K. and Sakai, K., "Natural frequency identification method for a substructure in bridges and viaducts," *Proceedings of JSCE* A2, Vol. 77, No. 2, I_25-I_34, 2021 (in Japanese).
[6] Wada, K. and Sakai, K., "Natural frequency identification method for a substructure in railway bridges and viaducts," *RTRI report*, Vol. 37, No. 5, pp.19-27, 2023 (in Japanese).
[7] Brincker, R., Zhang, L. and Anderson, P., "Modal identification from ambient response using frequency domain decomposition," *Proceedings of 18th International Modal Analysis Conference*, San Antonio, Texas, pp. 625-630, 2000.
[8] Wada, K. and Sakai, K., "Verification of natural frequency identification method for a substructure in railway bridges and viaducts," *Journal of railway engineering*, *JSCE*, Vol. 27, 2023 (in Japanese).
[9] Railway Technical Research Institute, *Design Standards for Railway Structures and Commentary (Foundation Structures)*, Maruzen, 2012 (in Japanese).

Authors

Kazunori WADA, M.Eng.
Senior Researcher, Structural Dynamics and Response Control Laboratory, Center for Railway Earthquake Engineering Research
Research Areas: Earthquake Engineering

Kimitoshi SAKAI, Dr.Eng.
Senior Chief Researcher, Head of Structural Dynamics and Response Control Laboratory, Center for Railway Earthquake Engineering Research
Research Areas: Earthquake Engineering

Implementation and Verification of a Model for Predicting Train Congestion Levels during Disruptions

Hiroto UEDA **Kosuke NAKABASAMI** **Taketoshi KUNIMATSU**
Transport Operation Systems Laboratory, Signalling and Operation Systems Technology Division

Service disruptions significantly alter train congestion patterns, reducing the usefulness of standard real-time congestion information for passenger decision-making. To address this issue, this study proposes a model for predicting train congestion levels during disruptions. The model was evaluated using actual disruption data and achieved approximately 75% accuracy. The results indicate that features such as headway and congestion levels of the same train at one to three stations prior to the prediction target station are effective for congestion prediction during disruptions.

Key words**:** *congestion prediction, machine learning, gradient boosting tree, schedule disruption*

1. Introduction

Train operators have started providing real-time information about train congestion to improve customer satisfaction. However, congestion during disruptions such as train service cancellations or schedule changes differs from normal congestion. Consequently, standard congestion information currently provided does not help passengers make informed decisions about which train to take during a disruption. Consequently, it is thought that inconvenience to passengers could be alleviated if there was a service that could predict congestion in case of disruption and provide suitably relevant information, because passengers could modify their behavior, for example, by delaying their departure or choosing a less crowded train.

To address this problem, we developed a model to predict congestion levels for each train on each station-to-station segment during disruptions, using a machine-learning framework employing the Gradient Boosting Decision Tree (GBDT). The severity of congestion is divided into several levels based on occupancy rate (hereafter referred to as "congestion level"). Specifically, we developed a prediction model using features that are associated with congestion, including elapsed time since service resumption, headway, congestion level of preceding train, and congestion levels of the same train at one to three stations prior to the prediction target station. We then evaluated the performance of this model.

The structure of this paper is as follows: Section 2 describes previous studies concerning congestion prediction in public transportation. Section 3 explains the dataset and features that were created and used for constructing the prediction model. Section 4 presents the test data and prediction results, which are then discussed. Section 5 provides a conclusion and future work.

2. Previous studies

Many studies have investigated ways of predicting congestion levels in public transportation. In recent years, a large number of studies have employed machine learning techniques. Studies using neural networks include those by El Maazouzi et al. [1] and Nakabasami et al. [2]. Yang et al. [3] which employed a support vector machine, while Wang et al. [4], Jamar et al. [5], Gallo et al. [6], and Yamashiro et al. [7] used gradient boosting decision trees.

Most of these studies focus on normal operating conditions, and only a few address the prediction of congestion levels during disruptions. For example, Yamashiro et al. [7] examined major disruptions lasting 30 minutes or more and developed a method to predict passenger flow waves 15 minutes in advance. Yamashiro's model, which used past traffic rescheduling timetable and passenger counts as training data, achieved an accuracy of approximately 75%. However, their method predicts cross-sectional passenger volumes between stations at 15-minute intervals for up to two hours after a disruption occurs. It does not predict congestion levels for individual trains for each station-to-station segment. Consequently, it is difficult to provide train-specific information, for cases where for example, one train is extremely crowded while the following train is relatively empty.

The objective of this study is therefore to develop a model that can predict congestion levels for each train on each station-to-station segment during disruptions. Based on our understanding of the characteristics of the training data, we employ machine learning techniques commonly used in literature and select frameworks that are expected to perform effectively.

3. Development of the prediction model

In this section, we describe the development of a model that predicts congestion levels during disruptions. The model comprises two components: the machine learning framework adopted, and the set of features used for prediction. Section 3.1 introduces the training data used in this study, including details of its preprocessing, and key characteristics. Section 3.2 outlines the machine-learning framework, and Section 3.3 gives a detailed description of the feature set. Finally, Section 3.4 presents the evaluation metrics used to assess the performance of the prediction model.

3.1 Training data and congestion level derivation

This study analyzes a railway line located in a major metropolitan area, consisting of 24 stations, from Station A to Station X. This line operates multiple types of train services including local and rapid trains, and through services to other lines are also provided. The actual arrival and departure times of each train at each station, as well as the occupancy rate at departure, are recorded daily. These records enable us to construct a dataset comprising the indicators listed in Table 1.

For this study, we constructed training data for the target line by selecting four weekdays on which major disruptions occurred and

54 weekdays on which they did not. This resulted in 590,376 records. It should be noted that weekends and public holidays, when train timetables and passenger flow patterns differ significantly, were excluded from the training data.

To predict congestion levels, we defined these levels based on the congestion rate. Figure 1 illustrates the congestion levels and corresponding on-board crowding conditions for each level. We assigned Level 1 to congestion rates from 0% to 25% (inclusive), and defined Levels 2 through 9 in increments of 25 percentage points. Congestion rates of 225% or more were grouped into Level 9.

Examining the training data revealed that records belonging to Levels 8 and 9 accounted for less than 1% of all samples. Consequently, the training data are highly imbalanced, with significant disparities in sample counts across congestion levels. Therefore, a machine-learning framework capable of handling imbalanced data is required.

3.2 Machine learning framework adopted

As described in Section 3.1, the training data used in this study are imbalanced across congestion levels. Furthermore, a computationally efficient method is desirable so that the model can handle larger training data in the future. For these reasons, we have adopted LightGBM as our machine-learning framework. LightGBM [8] is computationally efficient and demonstrates strong predictive performance, even when data are imbalanced.

Gradient boosting decision trees belong to the family of ensemble learning methods. Ensemble learning is a technique that combines multiple simple prediction models to make more accurate predictions. Various ensemble approaches exist depending on the types of simple prediction models used and the way they are aggregated.

Gradient boosting decision trees use decision trees as simple prediction models. The first tree provides an initial prediction, after which subsequent trees are trained to predict the residual errors of the preceding trees. The model's final prediction is computed as the sum of the contributions from all trees.

Table 1 Names and data types of indicators included in the dataset

Indicator Name	Data Type
Date	String
Direction (In-bound / Out-bound)	Categorical
Train Number	Categorical
Train Order of Stations (Number of stations from origin)	Integer
Pass-Through Flag	Boolean
Station Name	String
Next Station Name	String
Scheduled Arrival Time at Station	Integer
Actual Arrival Time at Station	Integer
Scheduled Departure Time from Station	Integer
Actual Departure Time from Station	Integer
Congestion Rate at Departure	Float

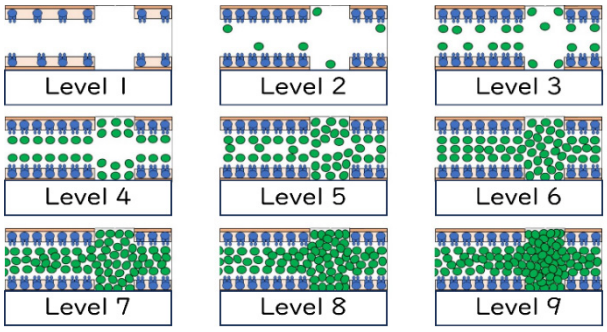

Fig. 1 Congestion levels and corresponding on-board crowding conditions

3.3 Features

In order to predict congestion levels accurately, it is important not only to use the indicators listed in Table 1, but also to extract informative indicators and to construct additional ones by combining multiple variables. Table 2 summarizes the list of features and their data types, referencing each metric and related study in the dataset.

The "Origin-Destination Pair" in Table 2 represents the pair of stations at which a train starts and terminates. To construct this feature, we assigned a unique integer to each origin-destination pair. For example, trains running from Station A to Station X were assigned 0, while trains running from Station X to Station A were assigned 1. A categorical feature that is created by assigning such integer labels is known as a label-encoded feature. Another approach is to give one binary feature for each direction. For example, assigning 1 to trains running from Station A to Station X and 0 otherwise, and similarly assigning 1 to trains running from Station X to Station A and 0 otherwise. This process produces one-hot-encoded features. Since LightGBM is known to achieve better predictive performance with label-encoded features than with one-hot-encoded ones [9], we adopted label encoding for this study.

"Hours of the Day" refers to the time period during which a train is in operation. For example, if a train departs from a station at 7:42, its feature value is set to 7, and if it departs at 8:15, its value is set to 8. This is because trains operating during the same hour, such as during the morning rush hour, tend to have similar congestion levels. This feature was therefore introduced to group trains operating under similar temporal conditions. "Station-to-Station Segment" represents the track section between two stations on which a train travels. We created this feature using the same procedure as for the origin-destination pair feature. We applied label encoding and assigned a unique integer to each station-to-station segment.

"Arrival Delay" and "Departure Delay" represent the differenc-

Table 2 Created features and their data types

Feature Name	Data Type
Direction (In-bound / Out-bound)	Categorical
Origin-Destination Pair	Categorical
Hours of the Day	Categorical
Station-to-Station Segment	Categorical
Arrival Delay	Integer
Departure Delay	Integer
Headway	Integer
Elapsed Time Since Service Resumption	Integer
Congestion Level of Preceding Train	Categorical
Congestion Level at N Stations Before (N = 1, 2, 3)	Categorical
Alternative Route Available Flag	Boolean

es, measured in seconds, between the scheduled and actual arrival (or departure) times of a train at a given station. Although these delays can be treated as categorical features, larger arrival (or departure) delays generally correspond to higher congestion levels. Therefore, the numerical values of the delays themselves are of primary interest. For this reason, both arrival delay and departure delay were kept as integer-valued features to preserve the meaning of their magnitudes.

"Headway" represents the time interval, measured in seconds, between the departure time of two consecutive trains. Larger headways generally imply that more passengers accumulate at the station, resulting in an increased number of passengers boarding the train. For this reason, following the same rationale as for arrival delay, headway is treated as an integer-valued feature.

"Elapsed Time Since Service Resumption" represents, in seconds, the difference between the departure time of a train from a given station and the time at which train operations resumed. Large numbers of passengers waiting at station are expected to board trains at once immediately after service resumes following a disruption, causing severe congestion. As time passes, congestion levels tend to return gradually to normal conditions. In order to capture this effect, we introduced this feature to indicate how many seconds each train operated after service resumption. As with arrival delay, this feature is treated as an integer-valued feature to preserve the meaning of its magnitude.

"Congestion Level at *N* Stations Before" refers to the congestion level of the same train located at *N* stations prior to the prediction target station. For example, Fig. 2 shows the sets of trains and stations for which congestion levels are used in the prediction.

Another railway line runs in parallel with the target line in some segments. To distinguish between station-to-station segments for where two or more routes are available, we applied the overlap feature concept proposed in Jamar et al. [5] and created the "Alternative Route Availability Flag." This feature returns a value of True if an alternative route is available from the current station to the next one, and False if not. This feature indicates whether another line operates on the corresponding station-to-station segment.

3.4 Evaluation metrics

To quantitatively evaluate the performance of the prediction model, we employ evaluation metrics that measure the accuracy of the model's outputs. Although various methods for measuring prediction performance have been proposed, this study uses Accuracy and the Macro F1-score. Accuracy is a standard metric defined as the proportion of correct predictions relative to the total number of predictions and is generally easy to interpret. However, if there are significant differences in the number of samples across classes, Accuracy is dominated by the majority class and may fail to reflect the model's performance in minority classes. Our training data show a highly imbalanced distribution of congestion levels. Due to this imbalance, relying solely on Accuracy is insufficient for evaluating the model performance.

Therefore, in addition to Accuracy, we also employ the Macro F1-score, a metric commonly used for evaluating model performance on imbalanced data. Even if the model achieves high Accuracy for congestion levels that occur frequently during operations (e.g., levels 1 through 6), the Macro F1-score will remain low if it performs poorly in rare but highly congested situations (e.g., levels 8 or 9). For this reason, the Macro F1-score is an effective metric for assessing the model's ability to accurately predict not only typical conditions but also severe congestion.

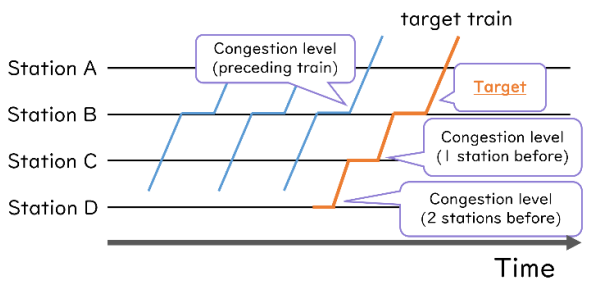

Fig. 2 Congestion levels of the preceding train and the target train

4. Case study

In this section, we present the prediction results of the model developed in Section 3 for a real-world case study. We then discuss its prediction performance, feature importance, and prediction error patterns in prediction errors. Section 4.1 describes the test data, followed by Section 4.2, which presents the prediction results.

4.1 Test data

The study aims to predict congestion levels during disruptions. Therefore, for the test data, we selected a day on which a large-scale disruption occurred that was not included in the training data described in Section 3.1. Figure 3 visualizes the situation on this day, showing a portion of the timetable (in-bound trains departing between 6:00 and 10:00), colored by congestion level. In the figure, the horizontal axis denotes time; the vertical axis, stations; and each slanted line, an individual train. On this day, an accident involving a person on the track occurred at Station Q at 6:32, and operations resumed at 7:27. Trains with higher congestion levels are represented by warmer colors, while missing values are indicated in gray.

Looking at Fig. 3, we observe the following situations at Station M:

- Severe crowding makes boarding difficult for more than 30 minutes, starting from the first train after service resumption.
- A severely crowded train arrives, followed by a relatively uncrowded one.

These observations indicate that congestion levels can vary significantly even between consecutive trains.

This study assumes that passengers focus on congestion changes approximately 15 minutes ahead, which corresponds to a distance five stations in this case study.

Based on these considerations, we defined the test target as in-bound trains running from Station M to Station H (five stations downstream) between 7:35 and 10:35. This period covers the interval from service resumption until delays were nearly cleared, as indicated in Fig. 3 by the area enclosed by the gray dashed line. The dataset for this period consists of 212 records. To construct the test data, we preprocessed these records and generated features according to the procedures described in Section 3.1 and 3.3, respectively.

4.2 Prediction results

On the test data described in Section 4.1, the model achieved an Accuracy of 75% and a Macro F1-score of 75%.

Figure 4(a) presents the confusion matrix, where the vertical axis corresponds to the predicted congestion levels and the horizon-

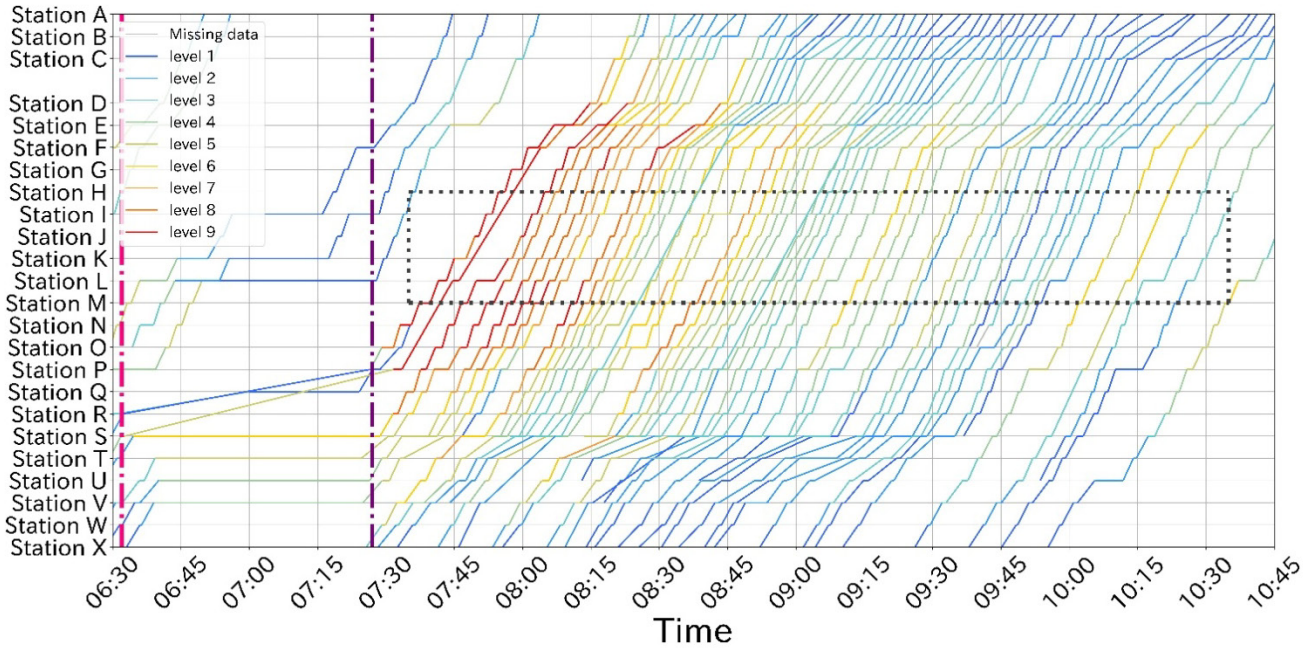

Fig. 3 Actual timetable color-coded by congestion level (area enclosed by gray dashed line represents test data)

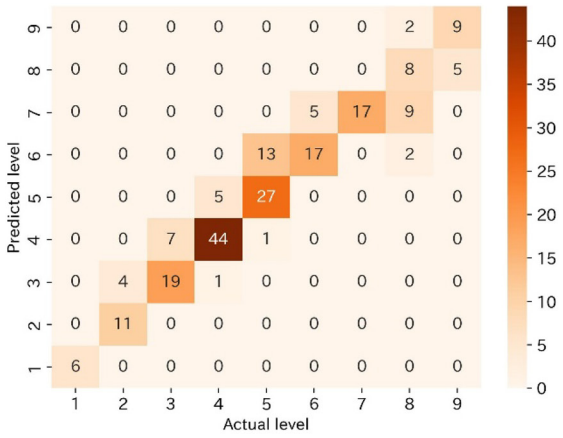

(a) Confusion matrix

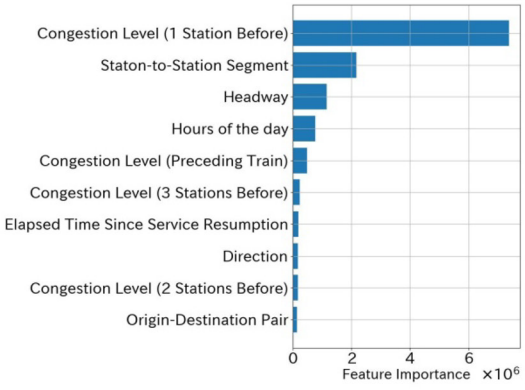

(b) Feature importance

Fig. 4 Prediction results from model

tal axis represents the actual congestion levels. The confusion matrix indicates that for actual congestion levels between 1 and 6, the model generally predicts the correct level, although there is a slight tendency to overpredict by one level. For actual congestion levels of 7 or higher, the discrepancy between the actual and predicted congestion levels remains within one level in most cases. However, for an actual level of 8, the model occasionally underpredicts by two levels. A tendency to underpredict congestion levels when the actual congestion level is high is consistent with findings reported by Gallo et al. [6]. One possible reason is that the training data contained very few instances comparable to the extreme congestion conditions observed in the test data. As shown in Fig. 3, the test data includes a roughly 30-minute period during which all trains running on a specific section between two stations exhibit congestion levels of 8 or 9. Since no comparable patterns exist in the training data, the model likely could not learn such congestion conditions sufficiently.

Figure 4(b) presents the feature importance values, which are calculated using a metric called gain. In the decision trees employed by LightGBM, classification is performed by recursively splitting the data based on specific conditions. For example, the data may be partitioned into two groups depending on whether the value of feature X meets or exceeds a threshold of 10. Gain represents the improvement in the objective function resulting from a split on a particular feature, relative to the state before the split. During training, the gain value produced by each split is recorded for the corresponding feature; the final feature importance is then determined by summing these gain values for each feature across all trees. For more details on the computation of feature importance, see the XGBoost tutorial [11].

The congestion level at the previous station was identified as the most significant feature, followed by the station-to-station segment and the headway. In particular, the congestion level at the previous station made a significant contribution, whereas congestion levels at two or three stations prior had a negligible effect on improving Accuracy.

These results can be explained by both the characteristics of the target line and the definition of the congestion level. During the

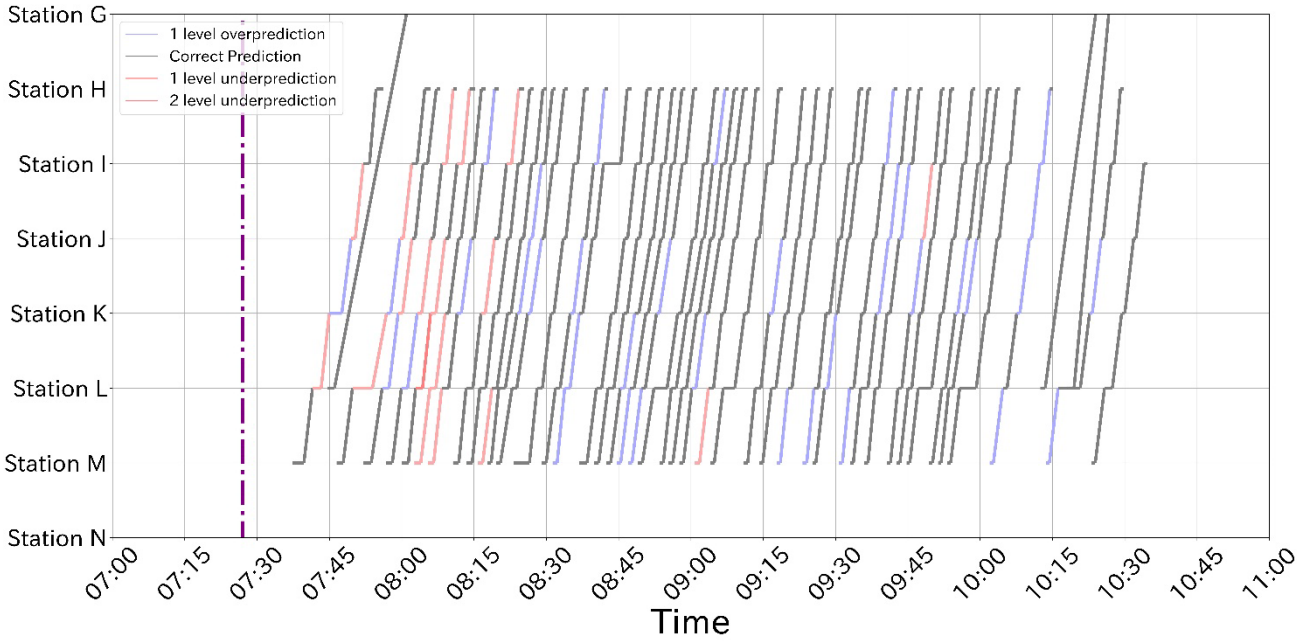

Fig. 5 Difference between actual and predicted congestion levels

morning rush hour on this line, most passengers travel from Stations X-L toward Stations E-A. Under normal conditions, congestion on board gradually increases from Station X and then decreases at Stations E and D. During disruptions, however, passengers who have been waiting on the platforms at Stations X-S board all at once, causing the congestion level to remain at 8 or 9 on the section between Stations O and E. As a result, rather than learning a pattern of gradual congestion increase starting from two or three stations prior, the model assigns greater importance to the congestion data from the immediate previous station.

Finally, Fig. 5 visualizes the differences between the actual and predicted congestion levels on the timetable. In this figure, lines are shaded in red or blue according to the absolute difference between the actual and predicted congestion levels; red indicates underprediction, whereas blue represents overprediction. Lines for which the predicted congestion levels match the actual values are shown in gray. Figure 5 illustrates that the model tends to underpredict congestion levels for trains running immediately following the service resumption. In contrast, trains operating approximately two hours after resumption, when congestion has relatively eased, the model tends to overpredict the congestion level by one step. This behavior is also likely due to the lack of similar situations in the training data. To improve prediction performance, it may be necessary to enhance the dataset by incorporating more diverse congestion pattern data.

5. Conclusions

This study proposed a model for predicting congestion levels during service disruptions. Evaluating the proposed model confirmed that it could predict the level of congestion with around 75% accuracy by using features such as headway and congestion levels of the same train at one to three stations prior to the prediction target station.

Future work will focus on two main areas: validating the model with other case studies and developing a model capable of long-term prediction of congestion. During disruptions, the key information for passengers is about when congestion subsides. Providing this information requires prediction further into the future. However, the current model relies on real-time congestion data from the target train, which limits its effectiveness for long-term prediction. Therefore, we plan to focus on developing a predictive model that does not require immediate congestion data.

References

[1] El Maazouzi, Q., Retbi, A. and Bennani, S., "Automatisation hyperparameters tuning process for times series forecasting: application to passenger's flow prediction on a railway network," presented at the *7th International Conference on Smart City Applications*, XLVIII-4W3-2022, pp. 53-60, 2022.

[2] Nakabasami, K., Tatsui, D. and Kunimatsu, T., "Prediction Method for Train Delay and Congestion Rate Using a Neural Network," *Journal of Information Processing*, Vol. 60, No. 4, pp. 1129-1140, 2019 (in Japanese).

[3] Yang, Q., Ma M., "Research on Prediction Method of the Train Occupancy rate Based on Machine Learning," presented at the *7th Annual International Conference on Network and Information Systems for Computers*, pp. 685-691. 2021.

[4] Wang, B., Wu, P., Chen, Q. and Ni, S., "Prediction and analysis of train passenger load factor of high-speed railway based on LightGBM algorithm," *Journal of Advanced Transportation*, Vol. 2021, pp. 1-10, 2021.

[5] Jamar, L., Büchel, B. and Corman, F., "A network-wide approach to predicting urban public transport passenger numbers at a stop-to-stop level," M.S. Thesis, ETH Zurich, Zurich, Switzerland, 2020.

[6] Gallo, F., Sacco, N. and Corman, F., Network-wide public transport occupancy prediction framework with multiple line interactions, *IEEE Open Journal of Intelligent Transportation report*, Vol. 26, No. 3, pp. 32-37, 2023.

[7] Yamashiro, M., Otsuka, R., Sahara, T., Kawasaki, K. and Sakairi, S., "Development of a passenger flow prediction model

during train service disruption," *Proceedings of TRANSLOG 2021*, Vol. 2021, No. 30, 2021.
[8] Ke, G., Meng, Q., Finely, T., Wang, T., Chen, W., Ma, W., Ye, Q. and Liu, T. -Y., "LightGBM: A highly efficient gradient boosting decision tree," *Advances in neural information processing systems*, Vol. 30, 2017.
[9] LightGBM's documentation: Advanced Topics, LightGBM (online), available from <https://lightgbm.readthedocs.io/en/latest/Advanced-Topics.html> (accessed 2025-01-16).
[10] Grandini, M., Bagli, E. and Visani, G., "Metrics for multi-class classification: an overview," arXiv (online), available from <https://arxiv.org/abs/2008.05756> (accessed 2025-01-16).
[11] XGBoost: Introduction to Boosted Trees, DMLC (online), available from <https://xgboost.readthedocs.io/en/latest/tutorials/model.html> (accessed 2025-01-16).

Authors

Hiroto UEDA
Researcher, Transport Operation Systems Laboratory, Signalling and Operation Systems Technology Division
Research Areas: Transportation Planning, Mathematical Optimization

Kosuke NAKABASAMI, Ph.D.
Senior Researcher, Transport Operation Systems Laboratory, Signalling and Operation Systems Technology Division
Research Areas: Big Data Analysis, Train Timetabling, Passenger Flow, Simulation

Taketoshi KUNIMATSU, Ph.D.
Senior Chief Researcher, Transport Operation Systems Laboratory, Signalling and Operation Systems Technology Division
Research Areas: Timetabling, Passenger Flow, Delay analysis, Train Operation Management

Estimation of Wheel/Rail Contact Conditions Based on State Space Model Using Data Acquired from Instrumented Wheelset

Shoya KUNIYUKI
Vehicle Mechanics Laboratory, Railway Dynamics Division

Takatoshi HONDO
Vehicle Mechanics Laboratory, Railway Dynamics Division (Former)

Mitsugi SUZUKI
Vehicle Mechanics Laboratory, Railway Dynamics Division

Takefumi MIYAMOTO
Meisei University

Kimihiko NAKANO
The University of Tokyo

This paper describes a practical method for estimating wheel/rail contact conditions using measurement data from an instrumented wheelset. The aim is to enhance the accuracy of running safety evaluations without significantly increasing measurement costs. This method estimates contact conditions, such as wheelset angle of attack, contact position, and friction coefficient by employing state-space theory and a Kalman filter-based state estimator. Vehicle dynamics simulations demonstrate that the proposed method reliably estimates contact conditions in curved track sections with radii under 600 m. Running test data validated the feasibility of the method and showed that the method provides an efficient solution for estimating contact conditions.

***Key words*:** *running safety, state estimation, instrumented wheelset, wheel/rail contact, wheelset angle of attack, Kalman filter*

1. Introduction

The running safety of railway vehicles in operation against flange-climb derailment is usually assessed using the derailment quotient, which is defined as the ratio of the lateral force Y to the wheel load Q acting between the wheel and rail. In Japan, train operation is considered safe from flange-climb derailment when the following condition (1), derived from Nadal's formula [1], is satisfied [2]:

$$\frac{Y}{Q} < \frac{\lambda}{S}, \tag{1}$$

where

$$\lambda := \frac{\tan\alpha_F - \mu}{1 + \mu\tan\alpha_F}. \tag{2}$$

Here, S denotes a safety factor, and λ, termed the critical derailment quotient, represents the mechanical limit at which the wheel flange comes into contact with the rail. The parameters α_F and μ denote the flange angle and the wheel/rail friction coefficient, respectively.

Y and Q can be measured by equipping vehicles with either an instrumented wheelset (IW) [3] or a monitoring bogie [4]. During standard running tests, the IW is used as a load cell with strain gauges attached to the wheel, as illustrated in Fig. 1. When the continuous measurement method [3] is used, the longitudinal tangential force T can also be obtained.

Although the derailment quotient Y/Q is widely used in practical safety evaluations, previous research has identified several ways to improve its accuracy. Some studies refined λ by incorporating realistic wheel/rail contact conditions [5-9], while others considered dynamic factors that affect derailment behavior [10, 11]. Furthermore, integrated evaluation methods that combine auxiliary indicators such as the inner wheel ratio [12], wheel rise [13], contact position [14], climbing time [15], and climbing distance [5] have been proposed to achieve more comprehensive safety evaluations. Among these efforts, understanding the wheel/rail contact conditions is especially important. However, in running tests using the IW, there remains no low-cost efficient method for monitoring these conditions.

This study therefore proposes a practical state-estimation approach to identify wheel/rail contact conditions such as the wheelset angle of attack, contact position, and friction coefficient. The proposed method uses data from an IW equipped with the continuous measurement technique [3] and applies state-space theory to estimate these state variables. The validity and performance of this method have been verified through vehicle dynamics simulations and running tests.

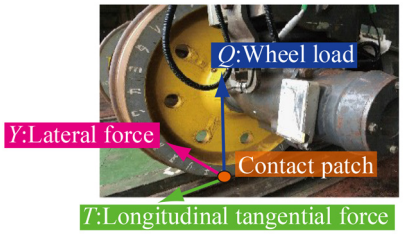

Fig. 1 Instrumented wheelset (IW)

2. Overview of estimation methods

2.1 Estimation method based on state-space theory

The identification of wheel/rail contact conditions is solved as an inverse problem. A state estimator based on state-space theory is derived and used to estimate the wheel/rail contact conditions from observable data. This state-space representation consists of two fundamental equations, expressed in (3) and (4):

$$\boldsymbol{x}(k)=\boldsymbol{f}(\boldsymbol{x}(k-1),\boldsymbol{u}(k-1)), \tag{3}$$

$$\boldsymbol{y}(k)=\boldsymbol{h}(\boldsymbol{x}(k),\boldsymbol{u}(k)). \tag{4}$$

Here, $\boldsymbol{x}$, $\boldsymbol{u}$, and $\boldsymbol{y}$ represent the state vector, the input vector, and the output vector, respectively. The function $\boldsymbol{f}(\cdot)$ describes a prediction model that defines the time evolution of $\boldsymbol{x}$. The function $\boldsymbol{h}(\cdot)$ represents an observation model that defines the relationship between $\boldsymbol{x}$ and $\boldsymbol{y}$. The discrete time step is denoted by k.

A Kalman filter framework is used to account for process and measurement noise. The *a posteriori* estimate $\hat{\boldsymbol{x}}$ of $\boldsymbol{x}$ is calculated using a linear predictor that accounts for plausibility of two models as expressed in (5):

$$\hat{\boldsymbol{x}}(k)=\hat{\boldsymbol{x}}^{-}(k)+\boldsymbol{G}(k)\{\boldsymbol{y}(k)-\hat{\boldsymbol{y}}^{-}(k)\}. \tag{5}$$

Here, $\hat{\boldsymbol{x}}^{-}$ and $\hat{\boldsymbol{y}}^{-}$ are the *a priori* estimates of $\boldsymbol{x}$ and $\boldsymbol{y}$, respectively, and $\boldsymbol{G}$ is the Kalman gain, which optimally balances the reliability of $\boldsymbol{f}(\cdot)$ and $\boldsymbol{h}(\cdot)$.

2.2 Plant model

The motion of the instrumented wheelset (IW) traveling along a track at a given longitudinal velocity ${}^{x}V_w$ is first considered, as illustrated in Fig. 2. In Fig. 2(a), the coordinate system O_w-$x_w y_w z_w$ is fixed at the center of gravity of the wheelset. At each wheel/rail contact patch, a local coordinate system O_i-$x_i y_i z_i$ (with i = 1 for the right wheel and i = 2 for the left) is defined parallel to the wheelset coordinates. The wheelset angle of attack and roll angle are denoted by ψ_w and ϕ_w, respectively. The contact phase θ_i represents the angular displacement of the contact patch from its lowest position [16]. The local friction coefficient μ_i and track curvature ρ are also taken into account. The distance between the right and left contact patches is 2b. For simplicity, both wheels are assumed to have an identical friction coefficient ($\mu_1 = \mu_2 = \mu$). The contact geometry, including the lateral contact position s_i, contact angle α_i, and rolling radius r_i of the contact patch, is summarized in Fig. 2(b). In the figure, quantities shown in blue indicate measured or known variables, whereas quantities shown in red denote estimated states.

2.2.1 Prediction model

The prediction model is derived mechanically by considering three relationships (R1, R2, and R3) at the contact patch:

- R1: Between creep forces and creepage
- R2: Between creepage and motion variables
- R3: Between measured forces and contact forces

Regarding R1, wheel/rail slip (creep) generates a longitudinal creep force ${}^{x}F_i$ and a transverse creep force ${}^{y}F_i$ as depicted in Fig. 3. Their dependence on creepage $\boldsymbol{v}_i$ is modeled using Kalker's linear theory [17] and the Lévi-Chartet nonlinear saturation model [18] in Fig. 4. Using the normal force N_i, the resultant relationship is expressed as:

$$[{}^{x}F_i, {}^{y}F_i]^T=\boldsymbol{F}_i(\boldsymbol{v}_i,\mu,N_i). \tag{6}$$

Regarding R2, the creepage $\boldsymbol{v}_i$ is expressed as a function of wheel/rail motion parameters, which include wheelset lateral displacement y_w, angle of attack ψ_w, roll angle ϕ_w, wheel rolling radius r_i, contact angle α_i, track curvature ρ, and running speed ${}^{x}V_w$. Considering the contact geometry and assuming a local proportional relationship between the wheelset lateral velocity $\dot{y}_w$ and the contact velocity $\dot{s}_i$ (satisfying $\dot{y}_w=a_i\dot{s}_i$, where the coefficient a_i is time-varying), some of the variables related to contact can be made dependent variables. Accordingly, $\boldsymbol{v}_i$ can be expressed as a function of the vector $\boldsymbol{x}_i:=[\psi_w, s_i, a_i]^T\in\mathbb{R}^3$ by (7):

$$\boldsymbol{v}_i=\boldsymbol{v}_i(\boldsymbol{x}_i,\dot{\boldsymbol{x}}_i,\rho,{}^{x}V_w). \tag{7}$$

Regarding R3, the contact forces $[{}^{x}F_i, {}^{y}F_i, N_i]^T$ can be expressed using the measured forces $[T_i, Y_i, Q_i]^T$ through a coordinate transformation $\boldsymbol{T}(\cdot)$, expressed as (8):

$$[{}^{x}F_i, {}^{y}F_i, N_i]^T=\boldsymbol{T}(\alpha_i,\psi_w,\phi_w,T_i,Y_i,Q_i). \tag{8}$$

By combining (6) - (8), a differential form for each wheel can be derived as (9):

$$\dot{\boldsymbol{x}}_i=\boldsymbol{v}_i^{-1}(\boldsymbol{F}_i^{-1}(\boldsymbol{T}(\boldsymbol{x}_i,T_i,Q_i,P_i),\mu),\boldsymbol{x}_i,\rho,{}^{x}V_w). \tag{9}$$

Unlike conventional prediction models based on the equation of motion that require dynamic interaction between the wheelset and the bogie, this formulation enables the contact condition to be estimated using data from a single IW.

Additionally, assuming that μ and a_i are locally constant around the estimation time t as expressed in (10):

$$\exists\Delta t>0,\ \forall\tau\in(t-\Delta t,\ t+\Delta t),\quad \frac{\mathrm{d}}{\mathrm{d}\tau}\begin{bmatrix}\mu(\tau)\\ a_i(\tau)\end{bmatrix}=0. \tag{10}$$

2.2.2 Observation model

The observation model incorporates measurement data from

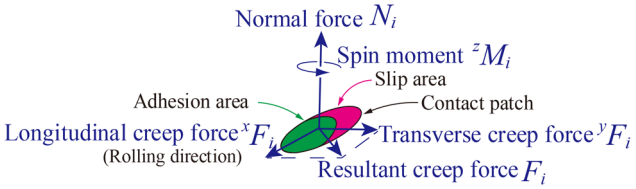

Fig. 3 Contact patch and creep forces

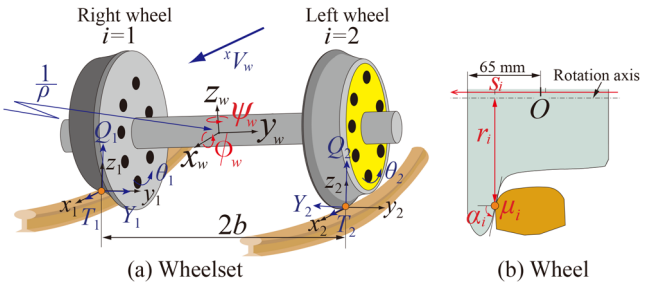

Fig. 2 Coordinates and coordinate systems

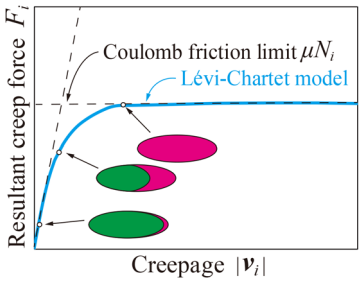

Fig. 4 Relationship between creep forces and creepage

the IW. The correspondence between the measured forces $[T_i, Y_i, Q_i]^T$ and the contact conditions is described by the functional form of (11) for each wheel:

$$[T_i, Y_i]^T = \boldsymbol{T}^{-1}(\alpha_i, \psi_w, \phi_w, N_i, Q_i). \quad (11)$$

Moreover, since a method has been proposed [16] to calculate the contact phase difference $\Delta\theta$: = $\theta_1 - \theta_2$ from strain signals measured by the IW, $\Delta\theta$ is treated as an observable. $\Delta\theta$ is approximated using other contact conditions as (12):

$$\Delta\theta \simeq \psi_w(\tan\alpha_1 - \tan\alpha_2). \quad (12)$$

2.3 Estimation system

The overall configuration of the proposed wheel/rail contact estimation system is shown in Fig. 5. Measurement data obtained from the IW include the longitudinal tangential forces T_i, lateral forces Y_i, wheel loads Q_i, contact phase difference $\Delta\theta$, and running velocity ${}^xV_w$ (i = 1 for the right and i = 2 for the left wheel). The model parameters include Kalker's creep coefficients κ_{11}, κ_{22}, κ_{23} [17], the saturation parameter β from the Lévi-Chartet model [18], the neutral rolling radius r_0, the contact patch spacing $2b$, and the wheel profile r as a function of lateral contact position s_i ($r_i = r(s_i)$). Track data include the curvature ρ referenced from registered geometry information. Information regarding slack, superelevation, and rail profile, however, is unnecessary.

To deal with model nonlinearity, an Unscented Kalman Filter (UKF) [19] is employed. The covariance matrices $\boldsymbol{V}$ and $\boldsymbol{W}$ for system noise $\boldsymbol{v}$ and measurement noise $\boldsymbol{w}$, the UKF weighing parameter κ_{KF} , and the measurement scaling factor Q_0 are adjusted to optimize estimation performance. The components of the state vector $\boldsymbol{x}$, the observed vector $\boldsymbol{y}$, and the input vector $\boldsymbol{u}$ are defined as (13) – (15):

$$\boldsymbol{x} = [\dot{\psi}_w, \psi_w, \dot{y}_w, s_1, s_2, a_1, a_2, \mu]^T \in \mathbb{R}^8, \quad (13)$$

$$\boldsymbol{y} = 1/Q_0[T_1, T_2, Y_1, Y_2, Q_0\Delta\theta]^T \in \mathbb{R}^5, \quad (14)$$

$$\boldsymbol{u} = [P_1, P_2, \rho, {}^xV_w]^T \in \mathbb{R}^4. \quad (15)$$

The estimated values are the wheelset angle of attack ψ_w, the lateral contact position s_i, and the friction coefficient μ, which represent the wheel/rail contact conditions to be estimated.

3. Verification of estimated performance using vehicle dynamics simulations

To evaluate the performance of the proposed method, numerical analyses were conducted using vehicle dynamics simulations. These simulations allow various track geometries and running conditions to be analyzed efficiently, while providing physical quantities that are difficult to obtain experimentally. The multibody simulation software Simpack ver. 2021.5 (Dassault Systèmes) was used in this study.

3.1 Simulation conditions

3.1.1 Vehicle model

The vehicle model was created for a typical Japanese narrow-gauge railway system with a track gauge of 1067 mm. It consists of a car-body, two bogie frames, and four wheelsets modeled as rigid bodies, as illustrated in Fig. 6. Each rigid body (shown in blue) has six degrees of freedom, and the connections between them include spring and damper elements (shown in red), which represent the primary and secondary suspension characteristics. The wheel profile adopts a modified-arc tread shape, which is commonly used in current Japanese commuter trains.

3.1.2 Track model

The simulated track geometry, shown in Fig. 7, comprises a single left-hand curve composed of five consecutive sections: a straight section, an entrance transition curve, a circular curve, an exit transition curve, and a terminal straight section. The circular curve radius R was varied from 100 m to 1,000 m in increments of 100 m for each simulation case. The superelevation and slack were set to 0 mm for all cases. As shown in Fig. 8, the curvature ρ along each transition curve varies linearly with the longitudinal distance from its starting point. Each section is 100 m long, with 3.0 m (1.5 m at each boundary) of smoothing distance applied to ensure geo-

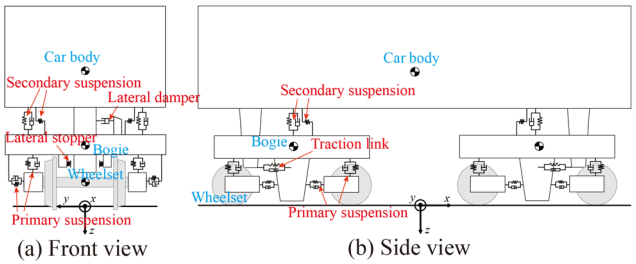

Fig. 6 Vehicle model used in simulation

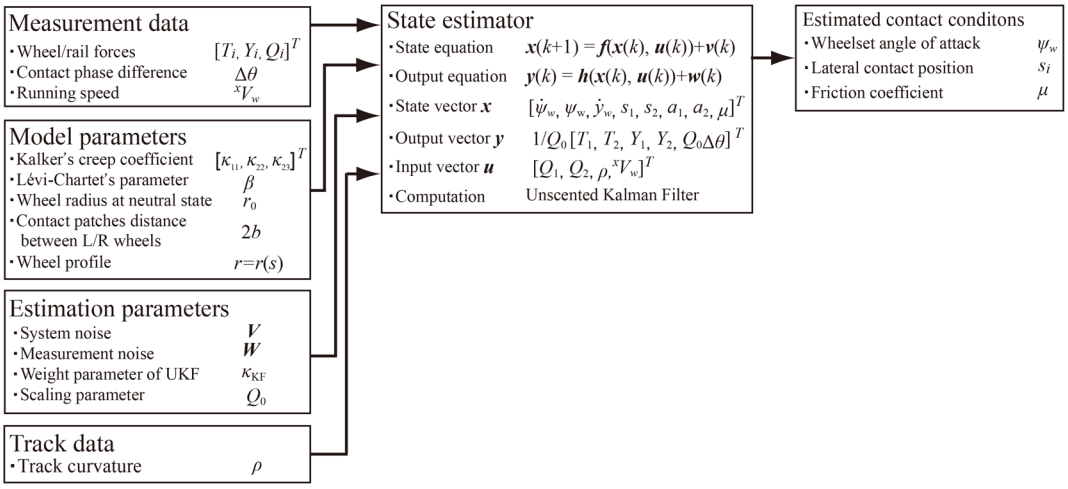

Fig. 5 Overview of estimation system

metric continuity between segments.

The rail profile follows the JIS 50 kgN shape, with a rail inclination of 1/40 that conforms to the standard tie-plate installation angle. The wheel/rail friction coefficient μ was varied from 0.05 to 0.70 in increments of 0.05, using identical values for both rails. Creep forces were computed using the FASTSIM algorithm [17].

3.2 Estimation results

3.2.1 Example of estimation results

Representative estimation results when R is equal to 100 m and μ is equal to 0.4 are shown in Fig. 9. In Fig. 9, the notation "^" denotes the estimated value, shown as a blue line, while the superscript "S" indicates the simulation reference, shown as a pink line. Additionally, the second axis represents the track curvature ρ, shown as a green dotted line. The results are summarized as follows:

・Friction coefficient μ (Fig. 9(a)):

On average, $\hat{\mu}$ closely matched ${}^{S}\mu$ throughout most of the curved sections, including the transitions. In contrast, $\hat{\mu}$ approached zero in straight sections and junctions between straight and transition curves, resulting in steady-state error. This is because the creepage $|\boldsymbol{v}_i|$ is minimal under straight-running conditions, which diminishes the effect of μ on the generation of creep forces. Once the wheelset enters a curve and creepage occurs, the impact of μ increases, leading to a more accurate estimation.

・Wheelset angle of attack ψ_w (Fig. 9(b)):

$\hat{\psi}_w$ was close to ${}^{S}\psi_w$ for most of the curved sections, including the transition curves. Conversely, the estimated values changed sharply at the junctions between the straight and transition curves, where the estimation was less accurate. This was likely due to variations in creepage $|\boldsymbol{v}_i|$ at the connection points, causing abrupt changes in $\hat{\mu}$. Consequently, the covariance matrix and Kalman gain which are calculated by the Kalman filter during the estimation process, could have been affected.

・Lateral contact position s_i (Fig. 9(c)):

The analysis focuses on the outer-rail contact position s_1, which is a key variable for running safety. An increase in s_1 indicates a shift of the contact patch toward the wheel flange. Like the above results, $\hat{s}_i$ and ${}^{S}s_i$ agreed well through most of the curve section, while substantial differences appeared in the straight section. This is because the sensitivity of the plant model decreases when the contact patch moves to the wheel tread region [20]. Conversely, in curves where the contact angle α_1 and rolling radius r_1 vary rapidly with s_1, the Kalman gain effectively updates the state, resulting in better accuracy.

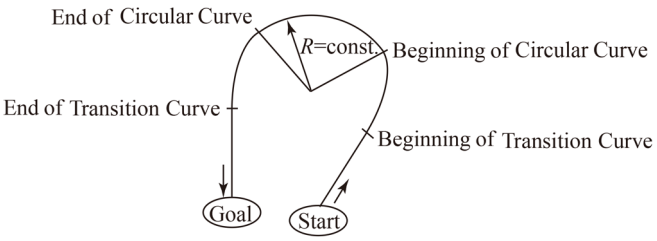

Fig. 7 Track layout

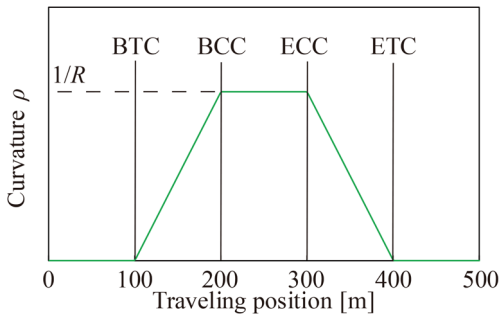

Fig. 8 Track curvature

3.2.2 Summary of all estimation results

Figure 10 shows diagrams summarizing the estimation accuracy across circular curve sections of various radii, created to examine the applicable range of the proposed method. In this figure, the horizontal axis represents the friction coefficient ${}^{S}\mu$ set in the simulation, and the vertical axis represents the circular curve radius R. The color contours show the average difference between the simulation and estimated values for μ (Fig. 10(a)) and ψ_w (Fig. 10(b)) across the circular curve sections. Red regions indicate underestimation, whereas blue regions represent overestimation. Color intensity reflects the magnitude of deviation.

As can be seen in Fig. 10, when $R \leq 600$ m, the estimation er-

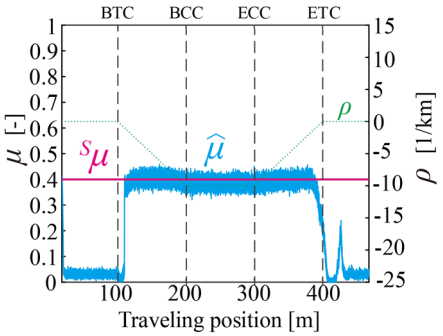

(a) Friction coefficient μ

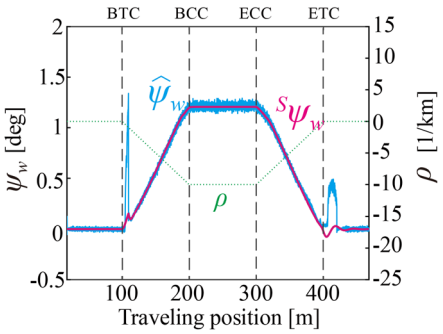

(b) Wheelset angle of attack ψ_w

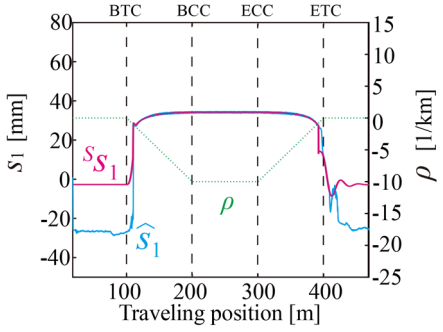

(c) Outer side contact position s_1

Fig. 9 Estimation results (R = 100 m and μ = 0.4)

rors remain small, typically $|\hat{\mu}-{}^{S}\mu|<0.1$ and $|\hat{\psi}_w-{}^{S}\psi_w|<0.06$ deg, demonstrating reliable estimation accuracy. Conversely, for $R>600$ m, the errors increase, particularly in the high friction coefficient region, the effects of creepage reduce, leading to a tendency for the observability of contact conditions to decrease.

These results indicate that the proposed method is most effective under sharp curves, where creep forces reach saturation or approach to the Coulomb friction limit. Under such conditions, the contact states are sufficiently constrained, enabling the Kalman filter-based estimation to converge with high accuracy.

4. Validation using actual measurement data

To verify the applicability of the proposed estimation method to real operating conditions, estimations were made using running test data acquired at the Railway Technical Research Institute (RTRI). In this running test, the contact conditions to be estimated were not directly measured. Therefore, a direct comparison between the measured and estimated values was not possible. To address this issue, vehicle dynamics simulations were conducted under conditions that matched the running test data. Simulation results were then compared with the estimation outputs to evaluate consistency, as illustrated in Fig. 11.

First, the measured running test data were used for state estimation (Step ① in Fig. 11). Secondly, vehicle dynamics simulations were conducted under the matching conditions (Step ②), in which the friction coefficient μ was tuned to reproduce the measured force components. The same simulation software as described in the previous section was employed. Finally, the estimated values obtained from the field data were compared the simulated reference values to assess the validity and accuracy of the proposed method (Step ③).

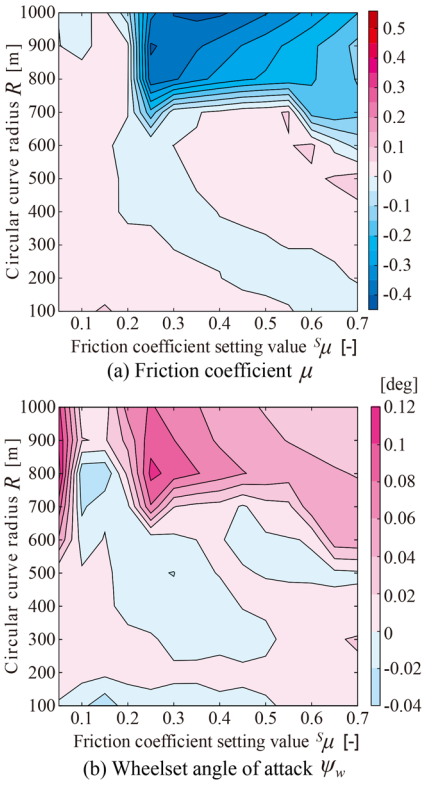

Fig. 10 Estimation error in circular-curve sections

4.1 Overview of running tests

Running tests were carried out on a dedicated test track at RTRI, using a commuter-type test car equipped with an instrumented wheelset (IW). As shown in Fig. 12, the test car was hauled by a locomotive during the measurement runs. The IW was installed on the leading wheelset of the car to acquire the necessary data for estimation, including wheel/rail forces and contact phase difference signals. Measurements were sampled at intervals of 1 ms. The test track consists of a leftward curve composed of four circular curves, denoted as C_1 to C_4, each having different combinations of curve radius R, superelevation C, and slack S, as listed in Fig. 13. The target running speed was set at 20 km/h. Among the available data, the results obtained running through these four circular curves were used in this validation analysis.

4.2 Estimation results

State estimation was attempted using the measured running test data. The focus of this evaluation was not on the local consistency of the estimated values, but rather on determining whether the proposed method yielded reasonable average responses when applied to circular-curve sections.

The contact phase difference $\Delta\theta$ which is an observed quantity, has a significant influence on the estimation results [20]. Therefore, sections where the difference between the measured value ${}^{M}\Delta\theta$ and the simulated value ${}^{S}\Delta\theta$ was large were unsuitable for evaluation. The average values of ${}^{M}\Delta\theta$ and ${}^{S}\Delta\theta$ were compared across the four circular-curve sections, and the results are shown in Fig. 14. The figure indicates that the differences between ${}^{M}\Delta\theta$ and ${}^{S}\Delta\theta$ were large

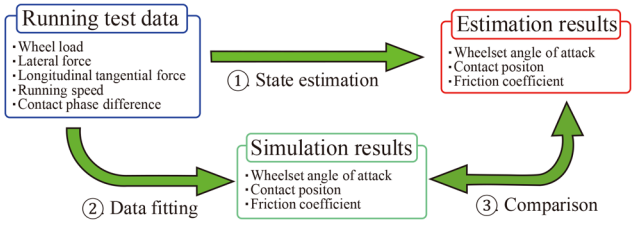

Fig. 11 Flow of validation procedure

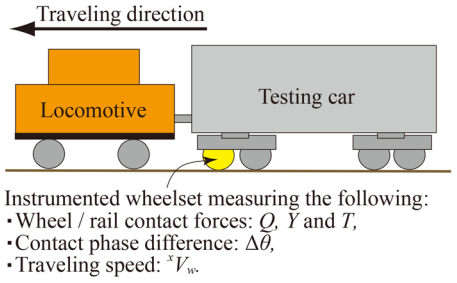

Fig. 12 Testing car and measurement data items

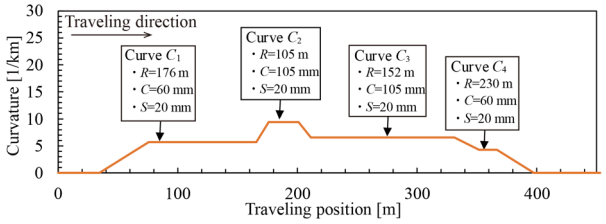

Fig. 13 Track geometry

for curves C_1 and C_4, while relatively small for curves C_2 and C_3. Consequently, the analysis focused on curves C_2 and C_3, which are considered representative examples for performance evaluation. The differences between ${}^{M}\Delta\theta$ and ${}^{S}\Delta\theta$ results are thought to be partly due to the use of ideal rail cross-section data for the designed profile in the simulation, without accounting for actual rail wear.

The estimation results are shown in Fig. 15, and the findings are summarized below. The notation "^" and the superscript "S" denote the estimated value and the simulation reference.

・Friction coefficient μ (Fig. 15(a)):

The value of ${}^{S}\mu$ used to reproduce the measured contact forces was set relatively high at ${}^{S}\mu = 0.55$. This is probably because the running test data were obtained under dry conditions, with the test vehicle operated repeatedly on the same section within short intervals, resulting in increased rail surface adhesion. $\hat{\mu}$ was close to ${}^{S}\mu$, indicating that the proposed method provided a reasonable and physically consistent estimation on average.

・Wheelset angle of attack ψ_w (Fig. 15(b)):

Even in cases with relatively large error, the difference between $\hat{\psi}_w$ and ${}^{S}\psi_w$ remained within approximately 0.06 deg, suggesting that the proposed method achieved reasonable estimation accuracy for the angle of attack on average.

・Outer-rail-side lateral contact position s_1 (Fig. 15(c)):

In Curve C_2, a small difference of about 2 mm was observed between $\hat{s}_1$ and ${}^{S}s_1$, but in both surveyed curves $\hat{s}_1$ followed ${}^{S}s_1$ closely. This demonstrates that the proposed method captures the general behavior of lateral contact positions in curved sections.

These comparisons show that the proposed method produces consistent and reasonable results, even when applied to actual measurement data. The findings confirm the feasibility of using the proposed method in practical field testing, enabling the estimation of wheel/rail contact conditions based solely on signals from an IW without additional specialized sensors or complex equipment.

5. Conclusions

This study proposed a method based on state-space theory for estimating wheel/rail contact conditions. The aim is to improve the accuracy of running safety evaluation against flange-climb derailment without increasing the measurement cost of present running tests. The effectiveness of the proposed method was verified through numerical simulations and actual running test data, as summarized below.

・Verification using vehicle dynamics simulations

Simulations were conducted using a vehicle model representative of Japanese narrow-gauge commuter rolling stock. The proposed method accurately estimated the wheelset angle of attack, wheel/rail outer contact position, and friction coefficient in curved sections with radii of up to approximately 600 m. In contrast, estimation accuracy decreased in sections with larger radii or on straight tracks. This trend is attributed to the low wheel/rail creepage under such conditions, which reduces the influence of the friction coefficient on creep forces and makes the contact conditions less observable.

・Validation using actual measurement data

The method was applied to field measurement data obtained from running tests at the Railway Technical Research Institute. Although the true values of contact conditions could not be directly measured, comparing the estimated results with vehicle dynamics simulations that were tuned to actual running conditions confirmed that the proposed estimator provides physically reasonable and consistent outputs for the actual measurement data.

These findings demonstrate that the proposed approach can be used to estimate wheel/rail contact conditions such as the friction coefficient, angle of attack, and contact position, using signals acquired from a single instrumented wheelset only, with no need for additional sensors or measurement systems. The method therefore offers a practical and cost-effective tool for enhancing safety assessment and understanding the dynamics of wheel/rail interactions in curved track sections.

Future work will focus on the following three aspects, with the aim of further enhancing the proposed method:

(1) Improving estimation performance when the friction coefficients of the inner and outer rails are estimated individually, or when

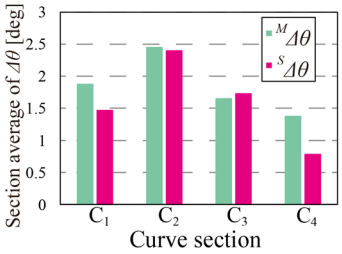

Fig. 14 Comparison results between ${}^{M}\Delta\theta$ and ${}^{S}\Delta\theta$

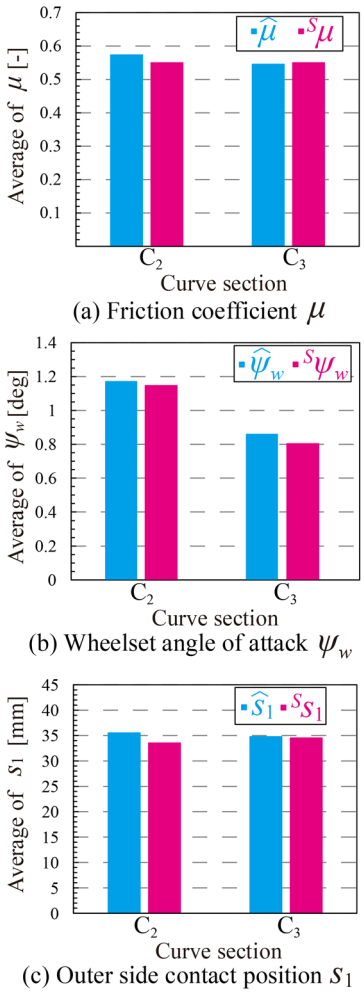

Fig. 15 Comparison between simulated and estimated results

these coefficients fluctuate.
(2) Verifying estimation performance taking dynamic system response into account.
(3) Investigating applicability to vehicle and track conditions differing from those assumed in this study.

Through these efforts, the proposed framework is expected to evolve into an integrated estimation system applicable to diverse railway environments, thereby contributing to advanced monitoring and safety management of running vehicles.

References

[1] Nadal, J., "*Locomotives á Vapeur, Collection Encyclopédie Scientifique*," Bibliotéque de Mécanique Appliquée et Génie, pp. 185-197, 1908.
[2] Railway Technical Research Institute ed., "*Manual on running tests for speed-up on Japanese meter gauge train*," Railway Technical Research Institute, pp. 80-92. 1993 (in Japanese).
[3] Ishida, H. et al., "A New Continuous Measuring Method of Wheel/Rail Contact Forces," *Quarterly Report of RTRI*, Vol. 35, No. 2, pp. 105-111, 1994.
[4] Matsumoto, A. et al., "A new measuring method of wheel-rail contact forces and related considerations," *Wear*, Vol. 265, No. 9-10, pp. 1518-1525, 2008.
[5] Elkins, J. and Wu, H., "New criteria for flange climb derailment," *Proceedings of the 2000 ASME/IEEE Joint Railroad Conference*, pp. 1-7, 2000.
[6] Matsumoto, A. et al., "Safety measures against flange-climb derailment in sharp curve-considering friction coefficient between wheel and rail-," *Wear*, Vol. 432-433, pp. 1-10, 2019.
[7] Santamaria, J. et al., "Influence of creep forces on the risk of derailment of railway vehicles," *Vehicle System Dynamics*, Vol. 47, No. 6, pp. 721-752, 2009.
[8] Barbosa, R. S., "A 3D contact force safety criterion for flange climb derailment of a railway wheel," *Vehicle System Dynamics*, Vol. 42, No. 5, pp. 289-300, 2004.
[9] Zeng, J. and Guan, Q. H., "Study on flange climb derailment criteria of a railway wheelset," *Vehicle System Dynamics*, Vol. 46, No. 3, pp. 239-251, 2008.
[10] Koo, J. S. and Oh, H. S., "A new derailment coefficient considering dynamic and geometrical effects of a single wheelset," *Journal of Mechanical Science and Technology*, Vol. 28, No. 9, pp. 3483-3498, 2014.
[11] Shabana, A. A. and Ling, H., "Spatial dynamic formulation of the L/V ratio and mechanics of wheel climb," *Nonlinear Dynamics*, Vol. 111, pp. 14731-14750, 2023.
[12] Weinstock, H., "Wheel climb derailment criteria for evaluation of rail vehicle safety," *Proceedings of the ASME Winter Annual Meeting*, Paper. 84-WA/RT-1, 1984.
[13] Nakahashi, J. et al., "Evaluation Method of the Flange Climb Derailment Considering the Wheel Rise," *RTRI REPORT*, Vol. 33, No. 3, pp. 5-10, 2019 (in Japanese).
[14] Zeng, Y. et al., "Geometric criterion for flange climb derailment and IWS-based implementation," *Proceedings of the 27th Symposium of the International Association of Vehicle System Dynamics*, pp. 237-246, 2021.
[15] Ishida, H. and Matsuo, M., "Safety criteria for evaluation of railway vehicle derailment," *Quarterly Report of RTRI*, Vol. 40, No. 1, pp. 18-25, 1999.
[16] Hondo. T. and Noguchi, Y., "Measurement method for longitudinal displacement of wheel/rail contact point using strain gauges put on wheels," *Mechanical Engineering Journal*, Vol. 7, No. 3, 2020.
[17] Kalker, J. J., "*Three-Dimensional Elastic Bodies in Rolling Contact*," Kluwer Academic Publishers, 1990.
[18] Yamamoto, D., "Wheel-rail Tangential Contact Force Model for Analyzing Vehicle Dynamics under Running in Rainy Conditions," *Quarterly Report of RTRI*, Vol. 66, No. 2, pp. 116-122, 2025.
[19] Wan, E. A. and Merwe, R. V. D., "The unscented Kalman filter for nonlinear estimation," *Proceedings of the IEEE 2000 Adaptive Systems for Signal Processing, Communications, and Control Symposium*, pp. 153-158, 2000.
[20] Kuniyuki, S. et al., "Improvement of estimation accuracy for wheelset angle of attack using a single-wheel creep-force model by taking into account contact phase difference and lateral contact position," *Proceedings of the Fifth International Conference on Railway Technology: Research, Development and Maintenance*, Paper. 31.22, 2022.

Authors

Shoya KUNIYUKI, Dr.Eng.
Senior Researcher, Vehicle Mechanics Laboratory, Railway Dynamics Division
Research Areas: Vehicle Dynamics, Running Safety, State Estimation

Takatoshi HONDO, Ph.D.
Senior Researcher, Vehicle Mechanics Laboratory, Railway Dynamics Division (Former)
Research Areas: Vehicle Dynamics, Running Safety, Measurement Technology

Mitsugi SUZUKI
Senior Researcher, Vehicle Mechanics Laboratory, Railway Dynamics Division
Research Areas: Vehicle Dynamics, Running Safety, Measurement Technology

Takefumi MIYAMOTO, Dr.Eng.
Professor, Vehicle Dynamics Laboratory, Faculty of Science and Engineering, Meisei University
Research Areas: Vehicle Dynamics, Rolling stock, Running Safety

Kimihiko NAKANO, Dr.Eng.
Professor, Nakano Laboratory, Institute of Industrial Science, the University of Tokyo
Research Areas: Vehicle Dynamics & Control, Driver Assistance, Automated Driving, Human Machine Interface, Energy Harvesting

Development of a Tri-axial Magneto-optical Probe for Measuring Magnetic Fields in the Low-frequency Bands

Yoshihito KATO
Electrical Machines Laboratory, Maglev Systems Technology Division

Masateru IKEHATA
Comfort Science and Engineering Laboratory, Human Science Division

When measuring low-frequency magnetic fields related to rolling stock, multiple sensors are needed. Therefore, we have developed a system that uses a tri-axial magneto-optical probe for this purpose. This probe is capable of wideband measurement, meaning only one device is required. A mechanism incorporating optical elements was constructed to detect magnetic fields at a 90-degree angle to those detected by conventional single-axial magneto-optical probes. These were then combined to create a tri-axial probe. Performance verification tests confirmed that the use of a low-noise laser significantly improves noise characteristics in the frequency range below 100 Hz.

Key words**:** *magneto-optical probe, Faraday effect, low-frequency magnetic fields, environmental magnetic fields, magnetic field measurement*

1. Introduction

The international standard IEC 62597 [1] was published in 2019 to provide measurement methods for magnetic fields generated by electronic and electrical equipment used in railway environments. In Japan, the Japanese Industrial Standard JIS E 0201, based on IEC 62597:2019, was published in March 2024. IEC 62597 specifies measurement methods for magnetic fields in the frequency range from DC to 20 kHz. It not only covers DC magnetic fields, traditionally considered in railway vehicles, but also defines methods for measuring and evaluating AC magnetic fields.

In response to this background, a magnetic field measurement system utilizing a magneto-optical probe (MO probe) was developed to streamline the measurement of magnetic fields in low-frequency in railway environments. This report describes the principle and configuration of the developed magneto-optical probe and then presents the results of performance verification experiments.

2. Challenges in conventional magnetic fields measurements and previous research

The establishment of measurement standards, both domestically in Japan and internationally, has increased the need for accurate measurement of low frequency magnetic fields. Meanwhile, a wide variety of sensors exist for measuring magnetic fields. Each sensor has different measurable frequency bands and intensity ranges, so selection must be based on the measurement objective. However, it is difficult for a single sensor to cover the entire frequency range specified by the standards, including the intensity ranges conceivable for railway vehicles. Traditionally, measurements have generally been performed using multiple sensors, such as employing search-coil type sensors for AC magnetic fields and different types of sensors for DC magnetic fields. Furthermore, fluxgate sensors capable of measuring magnetic fields from DC to AC have been developed. However, their maximum measurable intensity is only a few mT, so separate sensors are required for fields exceeding this level. Consequently, conventional low-frequency magnetic field measurements for railway vehicles require multiple sensor types, which presents a challenge for measurement efficiency.

Therefore, to address this challenge, prior research prototyped a single-axis magnetic field measurement system using a magneto-optical sensor. This sensor has a broader frequency band and intensity range than the aforementioned sensors, and its basic performance was confirmed [2].

In environments with multiple magnetic field sources, such as railway vehicles, it is inefficient to first locate the direction of maximum magnetic field and then measure it with a single-axial probe. Furthermore, magnetic fields associated with railway vehicles can change in magnitude and direction moment by moment due to the operation of the sources and surrounding environmental conditions. This makes it difficult to measure such fields with a single-axial probe. Therefore, this research aimed to enable three-axis measurement without enlarging the probe to enhance practicality.

Moreover, in the magnetic field measurement system using the single-axial probe, the minimum measurable magnetic flux density is limited to 10 μT due to noise generated by the system itself. The international standard IEC 62597 specifies that the minimum magnetic flux density that a measurement sensor must meet is 5% of the applicable limit. The applicable limit here is the value specified by the ICNIRP guidelines [3], which is referenced by IEC 62597 as the international guideline for environmental magnetic fields. The reference level for the lowest magnetic flux density is 27 μT for frequencies between 3 kHz to 20 kHz. The 5% value of this is 1.35 μT. To meet the requirements of this international standard, the probe must be capable of measuring down to this value. Therefore, in developing the measurement system using the tri-axial MO probe, the goal was to meet this requirement by reducing noise and achieving for a measurable range of 1 μT to 5 mT for DC magnetic fields and 1 μT to 300 μT for AC magnetic fields to 20 kHz.

3. Results of experiments

3.1 Measurement principle of magneto-optical probes

MO probes are measurement instruments based on the Faraday effect. When linearly polarized light is incident on a material called

a Faraday rotator, the plane of polarization rotates due to a magnetic field component that is parallel to the direction of light propagation (Fig. 1). The angle by which the plane of polarization rotates is called the Faraday rotation angle. The Faraday rotation angle θ_F [rad] is expressed by equation (1) in terms of the Verdet constant V [rad/(T·m)] as the intrinsic coefficient of the material, the magnetic flux density $\vec{B}$ [T] applied to the Faraday rotator, the normal vector $\vec{n}$ parallel to the optical axis, and the thickness ℓ [m] of the Faraday element.

$$\theta_F = V(\vec{B}\cdot\vec{n})\ell \tag{1}$$

The fundamental mechanism of measurement systems utilizing MO probes is based on detecting magnetic field fluctuations through this rotation angle of the plane of polarization.

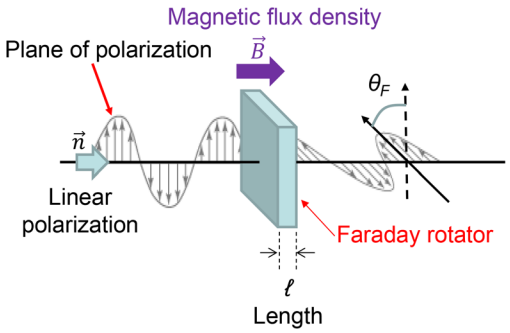

Fig. 1 Faraday effect

3.2 Three-axial magneto-optical probes

Figure 2 shows the configuration of the developed magnetic optical probe. Light input from an external source propagates through an optical fiber cable inside the probe housing and becomes linearly polarized when it passes through the polarizer. The linearly polarized light passes through an optical circulator and enters the Faraday rotator, where the plane of polarization rotates by an angle proportional to the magnitude of the magnetic flux density in the same direction as the light propagation. The light returning to the optical circulator then passes through the analyzer, where the amount of rotation of the plane is detected as a change in light intensity. This is converted into an electrical signal by the photodetector and output externally. While optical fiber cables are used for transmission between each optical element, it has been confirmed that the output fluctuates when these cables are bent. Therefore, they are physically fixed within this housing to prevent bending or other deformation.

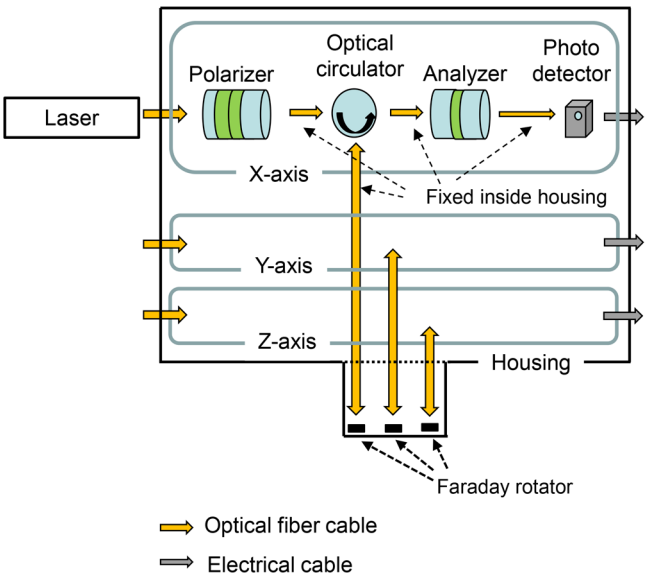

Fig. 2 Configuration of developed magneto-optical probe

In the previously developed single-axial probe, the polarizer, analyzer, and optical circulator are within the housing, and the optical fiber cables connecting them are fixed within the housing to prevent bending. In the newly developed probe, a compact photodetector has been incorporated into the housing. Consequently, the optical fiber cable connecting the analyzer to the photodetector is fixed within the housing in the same way as the other cables. This is expected to suppress output fluctuations caused by vibrations and other influences on this optical fiber cable. The above describes the configuration for one axis of the tri-axial probe. Three such axes are combined to form the main probe body.

To measure three orthogonal directions, Faraday rotators must be arranged along three axes. However, considering the need to use this probe in various locations in the field, the mechanism for incident light onto the Faraday rotators must be as small as possible.

Figure 3(a) shows the structure for detecting magnetic fields in the optical path direction (probe longitudinal direction). A magneto-optic crystal (bismuth-substituted magnetic garnet crystal [4]), which is a Faraday rotator measuring 0.3 mm × 0.3 mm × 0.3 mm, is mounted at the tip of the probe. Its end face is coated with a reflective film. When incident light passes through the magneto-optic crystal, its polarization plane rotates. The light is reflected in the direction of incidence by the reflective film and is processed outside the probe. Figure 3(b) shows the structure of the axis that detects magnetic fields at a 90-degree angle to this one. A right-angle prism is attached in the vicinity of the magneto-optical crystal. This changes the direction of the transmitted light by 90 degrees, enabling magnetic fields perpendicular to the original optical path direction to be detected.

A single axis is formed using the structure shown in Fig. 3(a). By mounting Faraday rotators at different 90-degree orientations with the structure shown in Fig. 3(b), two axes are formed, creating

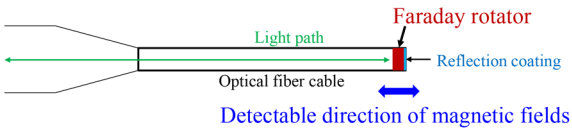

(a) Detection of magnetic fields parallel to direction of original light path

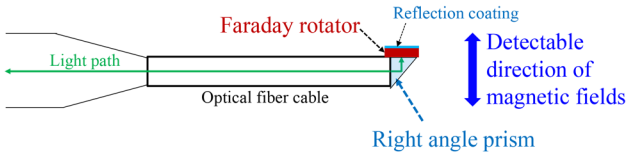

(b) Detection of magnetic fields perpendicular to direction of original light path

Fig. 3 Detection of magnetic fields using Tri-axial magneto-optical probe

a tri-axial MO probe. Furthermore, by placing these three Faraday rotators in proximity within the same case, a compact configuration is realized. The configuration of the sensing section of the probe is shown in Fig. 4, the overall view in Fig. 5, and the main specifications in Table 1. Inside the housing, a polarizer, an optical circulator, an analyzer, and a photodetector are stored for each of the three axes. Optical fiber cables for input and SMA connectors for output are installed at the end of the housing.

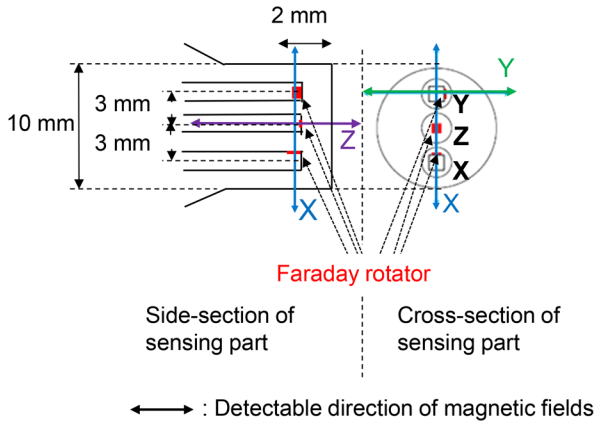

Fig. 4 Structure of sensing unit

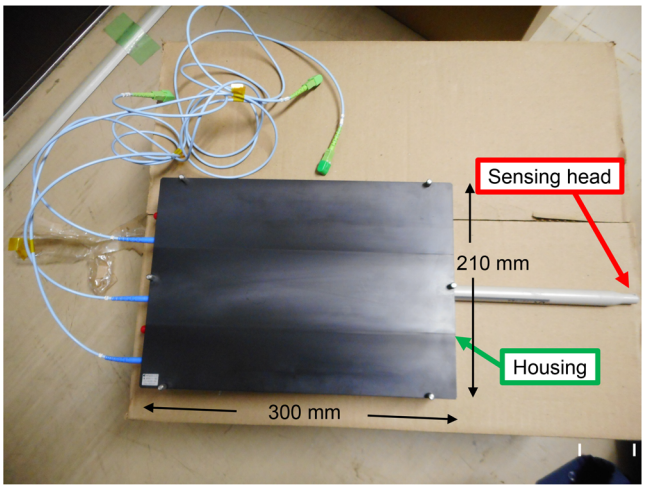

(a) From the top

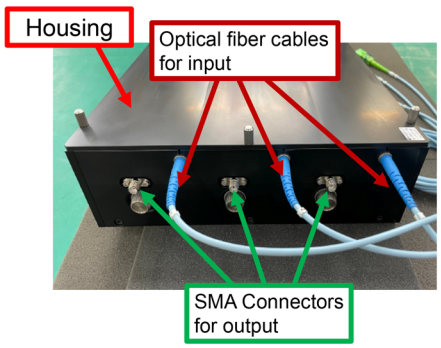

(b) Side view

Fig. 5 Tri-axial magneto-optical probe

Table 1 Main specifications of tri-axial magneto-optical probe

External dimensions	Overall Length: 500 mm (Sensor Head Section: 200 mm) Housing: 300(W) × 210(D) × 65(H) mm
Weight	2.0 kg or less
Housing material	ABS Resin (Plastic)

3.3 Measures to reduce noise originating from laser light source

A semiconductor laser is used as the light source to supply light to the MO probe. In the measurement system using the single-axial MO probe, a wavelength-tunable polarized laser commonly used in optical communications was employed as the light source. However, it was confirmed that this wavelength-tunable mechanism primarily generates noise in the ultra-low frequency band below 100 Hz. Figure 6(a) shows the laser output waveform. Since this noise affects measurement sensitivity below 100 Hz, it was necessary to reduce the noise in the laser output.

During the performance evaluation tests of the single-axial MO probe, we tested the laser wavelength as a parameter to confirm output stability. However, since no significant differences were observed based on wavelength, we selected 1550 nm, which offers a wider choice of optical components. Therefore, we considered using a fixed-wavelength laser at 1550 nm as the light source. Figure 6(b) shows the output waveform of the fixed-wavelength laser adopted this time. Such verification tests confirmed that the noise intensity is

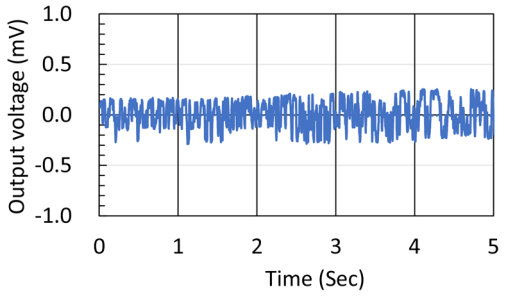

(a) Wavelength-tunable laser

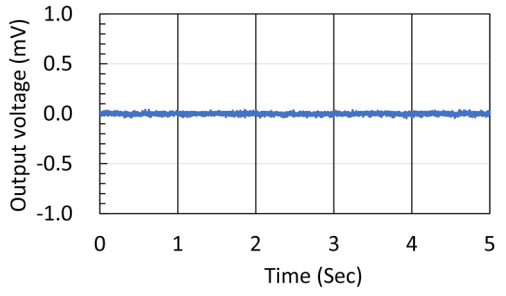

(b) Fixed-wavelength laser

Fig. 6 Comparison of laser outputs for measurement system light source (Wavelength λ = 1550 nm)

reduced to approximately one-tenth, primarily in the frequency band below 100 Hz.

From these results, it was decided to use this fixed-wavelength, non-polarized laser as the light source for this tri-axial magnetic field measurement system. Figure 7 shows the low-frequency magnetic field measurement system consisting of this laser and a tri-axial MO probe.

4. Verification tests

4.1 Time response verification test

Tests were conducted to confirm the time response characteristics of the fabricated tri-axial MO probe. Using the measurement system described earlier with a laser as the light source, tests were performed to measure the magnetic field generated by the Merritt coil [5] (Fig. 8).

Measurements were performed on 50 Hz sinusoidal magnetic fields as low-frequency magnetic fields as low-frequency magnetic fields, which are power frequency and used as the railway vehicle power supply frequency. Sinusoidal magnetic fields were generated by the Merritt coil, and the output at each axis of the MO probe was measured at that time. Figure 9 shows the output voltage waveforms for 50 Hz, 100 μT sinusoidal magnetic fields for each axis. Here, the center point of the output is set to 0 V. The current waveform flowing through the Merritt coil is also shown. These measurement results confirm that sinusoidal voltage waveforms corresponding to applied magnetic fields are output for each axis, verifying the time response.

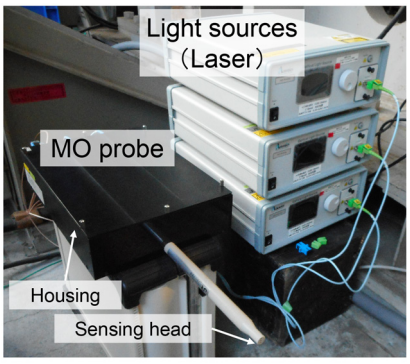

Fig. 7 Tri-axial magnetic fields measurement system using the magneto-optical probe

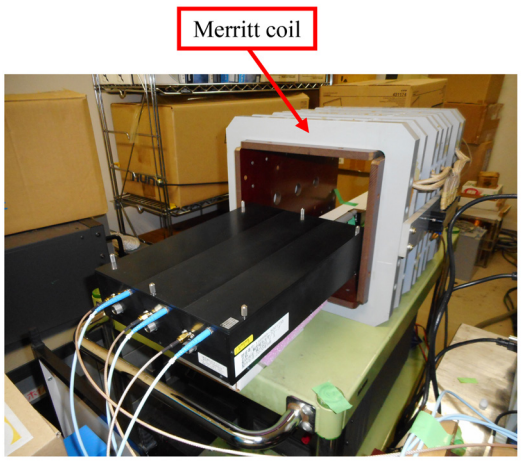

Fig. 8 Measurement experiments of measurements using Merritt coil generating magnetic fields

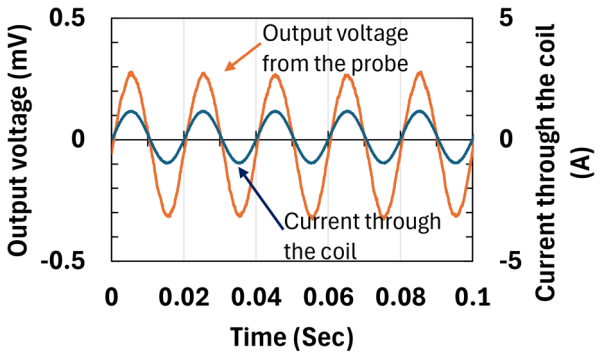

(a) X-axis

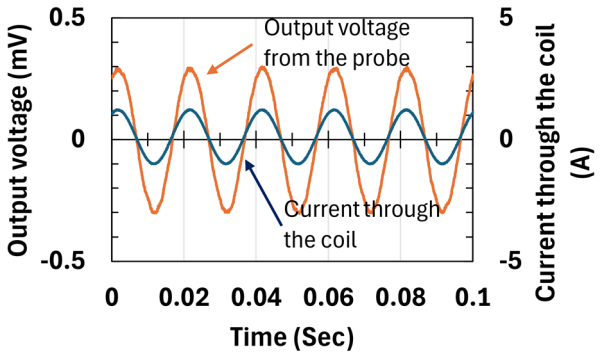

(b) Y-axis

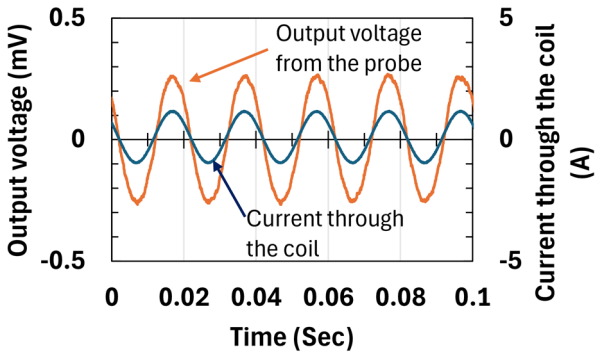

(c) Z-axis

Fig. 9 Time-series output waveforms for each axis (50 Hz, 100 μT)

4.2 Noise characteristics verification tests

The noise characteristics of the developed tri-axial magnetic field measurement system were verified. Magnetic fields from the Merritt coil were measured using this measurement system and the results were compared with those from the single-axial MO probe measurement system. Figure 10 shows the frequency analysis results for the three axes when measuring 50 Hz, 4 μT sine wave

magnetic fields generated by the Merit coil. Compared with the single-axial measurement system, the noise level in the frequency band below approximately 100 Hz was reduced to less than one-tenth at certain frequencies for all three axes. This confirmed that noise was sufficiently reduced for the measurement target signal at the minimum sensitivity level.

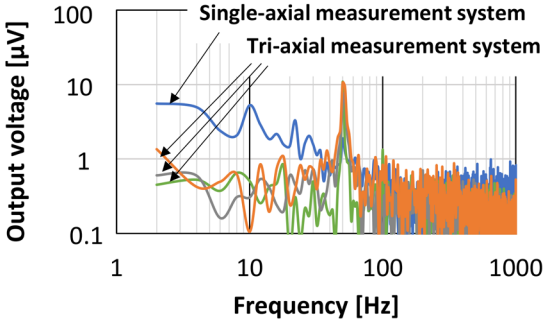

Fig. 10 Results of measuring sinusoidal magnetic fields (50 Hz) (Comparison with the single-axial measurement system)

4.3 Linearity verification tests

To verify the linearity of the measurement system, measurement tests were conducted to confirm the output of the MO probe when the magnetic flux density applied by the field-generating coil was varied at multiple frequencies. Figure 11 shows the output from the X-axis of the MO probe when DC, 50 Hz, and 20 kHz magnetic fields were applied. The applied magnetic flux density ranged from 1 μT to 5 mT for DC field, and from 1 μT to 300 μT for the 50 Hz and 20 kHz field. A Helmholtz coil was used to generate DC magnetic fields. These results confirmed that the maximum deviation for linearity was within 5% for each frequency. Similar results were obtained for the Y-axis and Z-axis.

It was confirmed that measurements from 1 μT—which could not be achieved with single-axial MO probe measurement systems—up to magnetic flux densities exceeding the ICNIRP guideline reference levels, can be performed with an accuracy within 20% as specified by the international standard IEC 62597, across frequencies up to 20 kHz.

4.4 Confirmation tests of measurement limits for DC magnetic fields

Measurement tests using the MO probe were conducted when DC magnetic fields varied from 0 to 5 mT. The results of the Z-axis measurement are shown in Fig. 12 (a). Figure 12 (b) shows the results obtained using an existing fluxgate sensor. Measurements using a fluxgate sensor cannot detect magnetic fields exceeding 1 mT due to overrange, however, it has been confirmed that the MO probe is capable of continuously measuring DC magnetic fields up to 5 mT.

4.5 Measurement tests simulating magnetic fields generated by railway vehicles

AC magnetic fields generated by the Linear Induction Motor Testing equipment used to drive railway vehicles (hereinafter referred to as the LIM Testing equipment) were measured. This equipment is installed in an experimental building of the Railway Technical Research Institute. This equipment consists of an arc-shaped armature and a cylindrical reaction plate and is driven by an inverter. Figure 13 shows the exterior of the LIM testing equipment, as well as the position of MO probe.

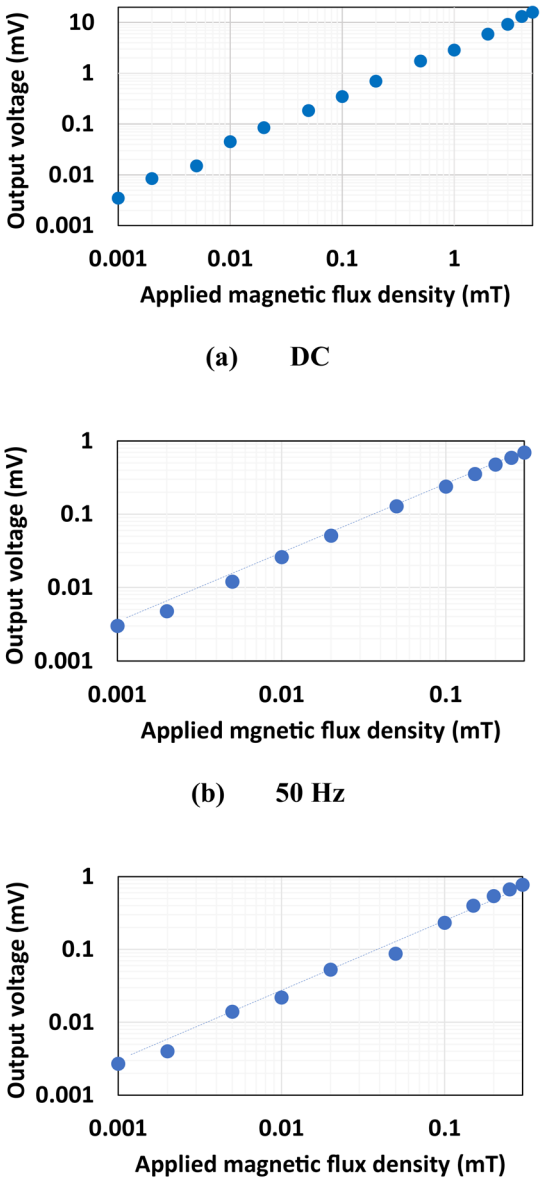

Fig. 11 Relationship between applied magnetic flux density and output voltage from the magne-to-optical probe (X-axis)

Figure 14 shows the measured waveforms for each of the three axes during LIM acceleration near the LIM testing equipment. Also shown the waveform of the current flowing through the cable from the inverter that energizes the LIM. A characteristic waveform with increasing frequency over time is observed. It was confirmed that corresponding waveforms were also output from each of the three axes of the MO probe.

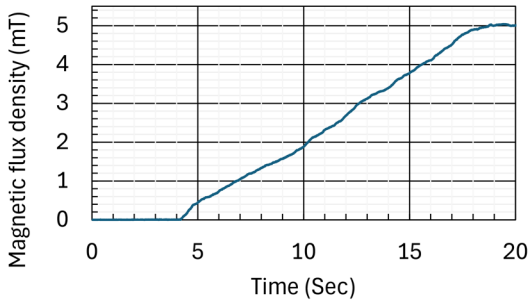

(a) Measurement using the magneto-optical probe

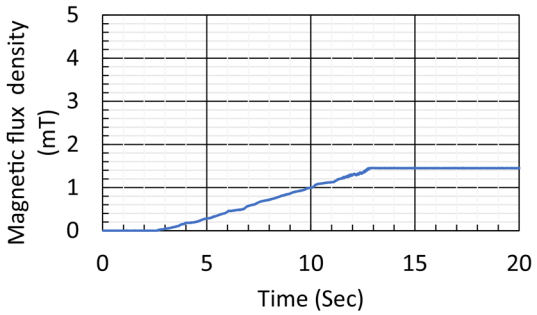

(b) Measurement using a fluxgate sensor

Fig. 12 Measurement of varying DC magnetic fields

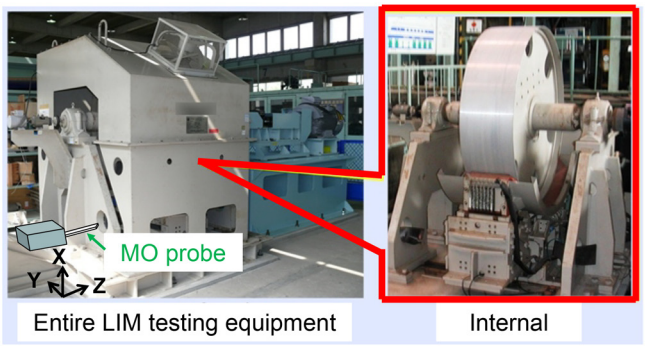

Fig. 13 Measurements near the LIM testing equipment for driving railway vehicles

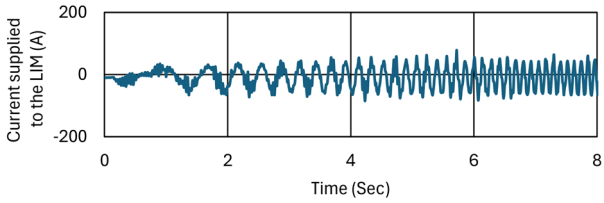

(a) Waveform of current supplied to LIM

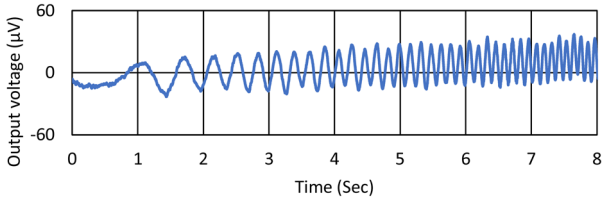

(b) Waveform of magnetic fields measured on X-axis

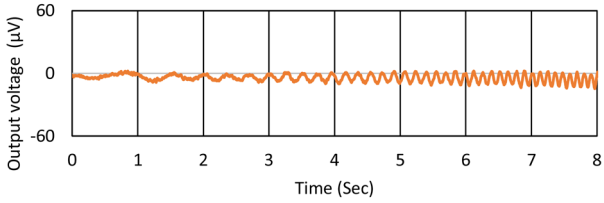

(c) Waveform of magnetic fields measured on Y-axis

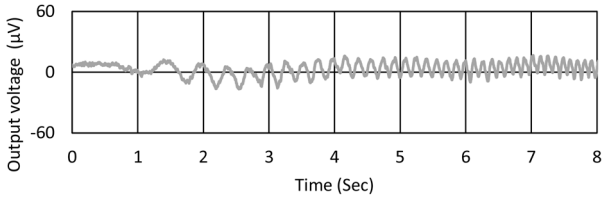

(d) Waveform of magnetic fields measured on Z-axis

Fig. 14 Waveform measured for magnetic fields around LIM testing equipment

5. Conclusions

To address challenges associated with measuring low-frequency magnetic fields in railway vehicles, we have developed a tri-axial MO probe and constructed a magnetic field measurement system. Considering its potential use in various locations, the probe was designed to be as small as possible for portability. We achieved tri-axial functionality by placing the light paths entering the Faraday rotators close together for all three axes, and by using a right-angled prism in the vicinity of the Faraday rotators to deflect the paths for two axes by 90 degrees. Furthermore, to suppress fluctuations in output light intensity caused by bending and vibrations in optical fiber cables, we physically fixed them within the housing. Regarding the light source, it was confirmed that wavelength-tunable lasers exhibit significant noise primarily in the frequency band below 100 Hz. Therefore, a new magnetic field measurement system that achieves substantial noise reduction in these frequency bands was constructed using a fixed-wavelength laser.

The performance verification tests of the measurement system confirmed a significant improvement in noise characteristics, primarily in frequency bands below 100 Hz, compared to the conventional system. Furthermore, measurement tests applying magnetic fields at frequencies ranging from DC to 20 kHz confirmed that the system meets the measurement accuracy required by the international standard (IEC 62597), within ± 20%.

Moving forward, we plan to refine the system for field use and utilize it for actual measurements.

Acknowledgment

We extend our sincere gratitude to Professor Yukihisa Suzuki of Tokyo Metropolitan University and all related parties for their extensive cooperation in conducting the experiments for this research.

References

[1] IEC 62597 ed1.0, "Measurement procedures of magnetic field levels generated by electronic and electrical apparatus in the railway environment with respect to human exposure," 2019.
[2] Kato, Y., Suzuki, Y. and Wake, K., "Magneto-optical probe with integrated optical elements for measuring environmental magnetic fields in the low- and intermediate-frequency bands," *IEEE Transactions on Instrumentation and Measurement*, Vol. 72, pp. 1-8, 2023.
[3] International Commission on Non-Ionizing Radiation Protection, "Guidelines for Limiting Exposure to TimeVarying Electric and Magnetic Fields (1 Hz - 100 kHz), *Health Physics*," Vol. 99, 818-836, 2010.
[4] Wittekoek, S., Popma, T. J. A., Robertson, J. M. and Bongers, P. F., "Magnet-optic spectra and the dielectric tensor elements of bismuth-substituted iron garnets at photon energies between 2.2-5.2 eV," *Phys. Rev. B*, No. 12, pp. 2777-2788, 1975.
[5] Merritt, SR., Purcell, C. and Stroink, G., "Uniform magnetic field produced by three, four, and five square coils," *Rev. Sci. Instrum*., 54(7), pp. 879-882, 1983.

Authors

Yoshihito KATO
Senior Researcher, Electrical Machines Laboratory, Maglev Systems Technology Division
Research Areas: Electromagnetic systems, Bio-EMC

Masateru IKEHATA, Ph.D.
Manager, Comfort Science and Engineering Laboratory, Human Science Division
Research Areas: Genotoxicity, Bioelectromagnetics, Occupational Hygiene

Engine Condition Diagnosis Using Oil Condition Monitoring System

Junichi SUZUMURA **Sadayuki KIKAWA** **Kazuki IKOMA**
Lubricating Materials Laboratory, Materials Technology Division

Tatsuro TAKASHIGE
Traction Systems Laboratory, Vehicle Technology Division

The authors developed an on-board lubricating oil condition monitoring system for diesel-powered vehicles. This system consists of an oil analyzer and a date logger capable of communicating with an external terminal via Wi-Fi. The performance of the system was evaluated using a bench test which artificially simulates internal engine wear and an on-track test using a commercial vehicle. The results showed that the monitoring system operated normally and could detect an increase in iron powder concentration in the engine oil.

***Key words*:** *lubricating oil, oil sensor, condition monitoring, wear particle, diesel engine oil, diesel engine*

1. Introduction

In railway vehicles in commercial operation, abnormal wear or seizure in sliding components, such as bearings or gears in diesel engines and transmissions, can lead to serious accidents or transportation disruptions due to equipment failure. Therefore, some railway operators adopt a condition diagnosis method that involves measuring the concentration of metal particles generated by wear and mixed into the lubricating oil [1]. This method detects signs of such damage and prevents equipment failures during commercial operation. However, such diagnostic instruments are limited to a few locations, such as major vehicle maintenance facilities, as the analyzers currently in use are large and expensive. Consequently, oil samples collected at local vehicle depots must be transported to these facilities for analysis. The time required to transport the samples makes it difficult to diagnose abnormalities rapidly and increase measurement frequency. Furthermore, the current method requires a certain level of proficiency to operate the analyzer and interpret the data. This limits the number of employees capable of handling the equipment. Given this background, there was a demand for developing a device capable of performing oil analysis at lower cost, more rapidly, and with simpler operation.

To address these challenges, the authors developed a stationary analyzer [2]. This device is easy to operate and possesses sufficient precision for diagnosing abnormalities through oil analysis of engines and transmissions. To use this analyzer, tubes are inserted into the oil ports of the vehicle's equipment. The pump in the analyzer then draws in the sample oil and feeds it to an oil sensor which can measure iron particle density. The sample oil is then returned to the vehicle equipment via the oil port. This method allows for the measurement of iron powder density in oil near the vehicle without the need to collect oil into a bottle.

The stationary analyzer is intended for diagnosing abnormalities during monthly vehicle inspections. However, increasing the frequency of analysis is not feasible due to the workload at the site. We therefore considered the adoption of an oil condition monitoring system that uses an on-line oil sensor installed on vehicles to monitor the condition of driving equipment. The aim is to increase the frequency of condition diagnosis and achieve early detection of abnormalities. Implementation of this system is expected to allow condition diagnosis at any time, such as during routine inspections or while the vehicle is in operation. Furthermore, utilizing this system for condition-based maintenance CBM, where inspections are performed based on the internal condition of the equipment, will enable extension of the intervals between major inspections requiring disassembly. This could lead to labor-saving and improved productivity in vehicle maintenance.

In this study, we developed an on-board analyzer which can be installed near the driving equipment of commercial vehicles to apply the condition monitoring system using an on-line oil sensor. We investigated the data transfer method, and evaluated the performance of the condition monitoring system by conducting engine bench tests and field tests.

2. Prototype of the on-board analyzer

A prototype of an on-board analyzer that incorporates an on-line oil sensor and pump was developed taking into account installation near the engine of commercial vehicles. Figure 1 shows the exterior of the device. This device incorporates an on-line oil sensor that operates on the same principle as the stationary analyzer. It can measure the density of iron particles in sample oil fed from sources such as the oil ports of an engine, within a range of 0 to 200 ppm, without any pretreatment. The sample oil is returned to the oil pan

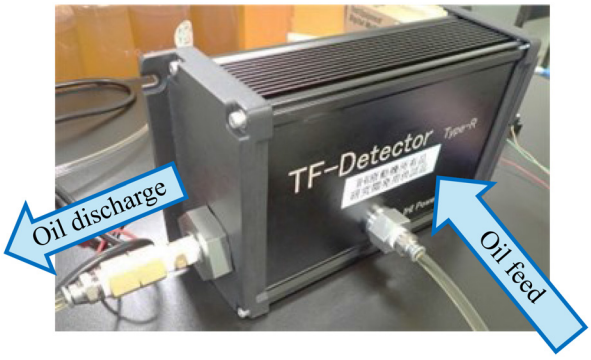

Fig. 1 Appearance of on-board analyzer

Table 1 Main specifications of on-board analyzer

Power supply	DC 24 V, Maximum 2 A
Size, Weight	300×160×40 mm, 5.3 kg
Measurement range, Output	Output current: 4 to 20 mA for iron powder density 0 to 200 ppm
Resolution	±3 ppm, Repeatability
Pump capacity	0.5 to 3 mL/s, depending on sample oil viscosity
Sample oil viscosity	20 to 2000 mm^2/s
Sample oil temperature	0 to 80 degrees Celsius

of the engine after measurement.

Table 1 shows the main specifications of the on-board analyzer. The changes from the stationary analyzer are as follows.

1) Compact design achieved by installing a pump function into the measurement unit

The stationary analyzer has a pump to circulate sample oil, which occupies a significant portion of the internal space of the analyzer. The on-board analyzer uses a mechanism in which a small rotary pump, driven by a motor installed in the measurement unit, feeds sample oil. This achieves significant miniaturization and weight reduction.

2) Omission of the control, display and recording units

The stationary analyzer incorporates a control unit and a touch panel for displaying and recording data and controlling the device. The on-board analyzer omits the control, display and recording units to make the analyzer smaller. Oil suction and measurement occur continuously when the power is on. This analyzer is designed to display and record the current value output by the sensor. This value can be converted to iron powder density using a general-purpose display device or data logger.

3) Operation by a DC 24 V power supply

The stationary analyzer uses AC 100 V power supply. In contrast, the on-board analyzer is designed to be installed under the vehicle floor and uses a DC 24 V power supply, which is widely used in standard diesel railway vehicles. For vehicles with different power supply voltages (e.g., DC 100 V), this can be addressed by installing a DC/DC converter.

3. Data transfer method

As previously mentioned, the prototype on-board analyzer omits the display and recording unit for measured values to miniaturize the analyzer and reduce the cost. Therefore, external devices, such as a data logger, are required to display and record the measured values. Consequently, we prototyped a recording device that allows users to view the measured values and download the data to external devices, such as tablet PCs or smartphones, via Wi-Fi. The reasons for using Wi-Fi for data communication are as follows.

1) It is versatile technology with low implementation costs.
2) It is not subject to legal regulation.
3) External devices, such as tablet PCs and smartphones loaned to crew members and maintenance staff, are available for use, which reduces additional costs.
4) The required data communication distance is typically up to about 20 meters during pre-departure inspections at maintenance depots or sidings, and during condition diagnostics performed by crew members near engines when abnormalities are detected during vehicle operation. Wi-Fi is fully capable of handling this communication distance.

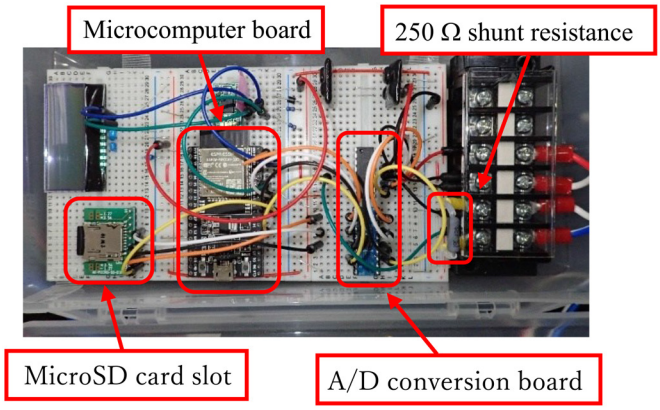

Fig. 2 Circuit configuration of recording device

Figure 2 shows the circuit configuration of the prototype recording device. The power supply is DC 24 V, which is the same as that of the on-board analyzer. The output from the on-board analyzer is recorded as follows.

1) Converts the output current (4 to 20 mA) from the on-board analyzer into a voltage (1 to 5 V) using a 250 Ω shunt resistor.
2) The output voltage is converted into a digital signal using an A/D conversion board (MCP3208).
3) The output voltage, along with the measurement date and time, is recorded in text file format onto the microSD card.

The recording device uses a microcomputer board with Wi-Fi communication capabilities to control the A/D conversion board and other components. By accessing the access point of the recording device from an external devices and entering a password, we can view a page via a browser. This page displays measurement values and allows us to control the recording device. We can perform various actions such as time synchronization, changing measurement intervals, setting conversion formulas from output voltage to iron powder concentration, and downloading data saved on the microSD card.

Sudden changes in vibration acceleration are considered unlikely to occur in the iron particle density of engine oil. The condition monitoring system is therefore currently being developed under the assumption that data will be checked either at fixed intervals, such as during pre-departure inspections; or when abnormalities occur during vehicle operation, such as unusual noises or exhaust irregularities. This system acquires data from recording devices so that maintenance staff and crew members can display and download data to their handheld terminals or other devices as needed. Furthermore, real-time measurement values can be displayed on the driver's console, because the on-board analyzer continuously performs measurements while the power is on.

4. Evaluating condition monitoring system performance through engine bench test

A real engine was fitted with the condition monitoring system consisting of an on-board analyzer and a recording device, and the system's performance was evaluated while the engine was in operation. A bench test simulating abnormal conditions was conducted by adding silicon carbide (SiC), a hard particle, into the engine oil to accelerate the wear of engine components. The iron particle density of

the engine oil was measured during the bench test using a prototype condition monitoring system to evaluate its ability to detect anomalies.

4.1 Installation of a condition monitoring system on real engine

Figure 3 shows an overview of the condition monitoring system's installation on the engine. The piping and mounting base were fabricated to securely attach the on-board analyzer to the engine. The analyzer-mounted base was then bolted to the engine's compressor base. Additionally, oil was fed to and discharged from the on-board analyzer via the engine's oil port. A component incorporating a copper tube that extends to the oil pan was fabricated, and installed in the oil port instead of the port cap. This component was connected to the piping of the on-board analyzer using a resin tube. Oil to be measured is drawn from the oil pan through this component via the oil feed tube attached to the oil port. After the measurement is taken, the oil returns to the oil pan through an oil discharge tube attached to the same component. The recording device is connected to the on-board analyzer via wiring. The measurement data output from the on-board analyzer is transferred from the recording device to an external device via Wi-Fi.

4.2 Overview of the abnormal simulation test

The abnormal simulation test was conducted by installing the test engine on the bench test rig and operating it under idling conditions, with an engine rotation speed of approximately 600 min^{-1}. In this test, SiC particles ranging from 2 to 3 μm in diameter were mixed into the engine oil to simulate abnormal wear on internal engine components, such as main metal bearings.

Table 2 shows the test numbers, operating time since test starts, and SiC density for each abnormal simulation test. The SiC density was set to 0.01–0.02 wt%. Before test No.3 began, a mixture of engine oil and SiC was supplied to achieve a SiC density of 0.02 wt%. Additionally, the stationary analyzers were used to take measurements at specific points, such as the start and end of each test. These results were then compared with those taken by the on-board ana-

Table 2 Overview of abnormal simulation tests

Test No.	Operating time after SiC insertion (seconds)	SiC density (wt%)	Special notes
1	0-3600	0.01	
2	3600-6300	0.01	The analyzer was restarted due to a power supply malfunction around 5010 seconds.
3	6300-9900	0.02	
4	9900-11700	0.02	The test commenced six days after the completion of test No. 3.

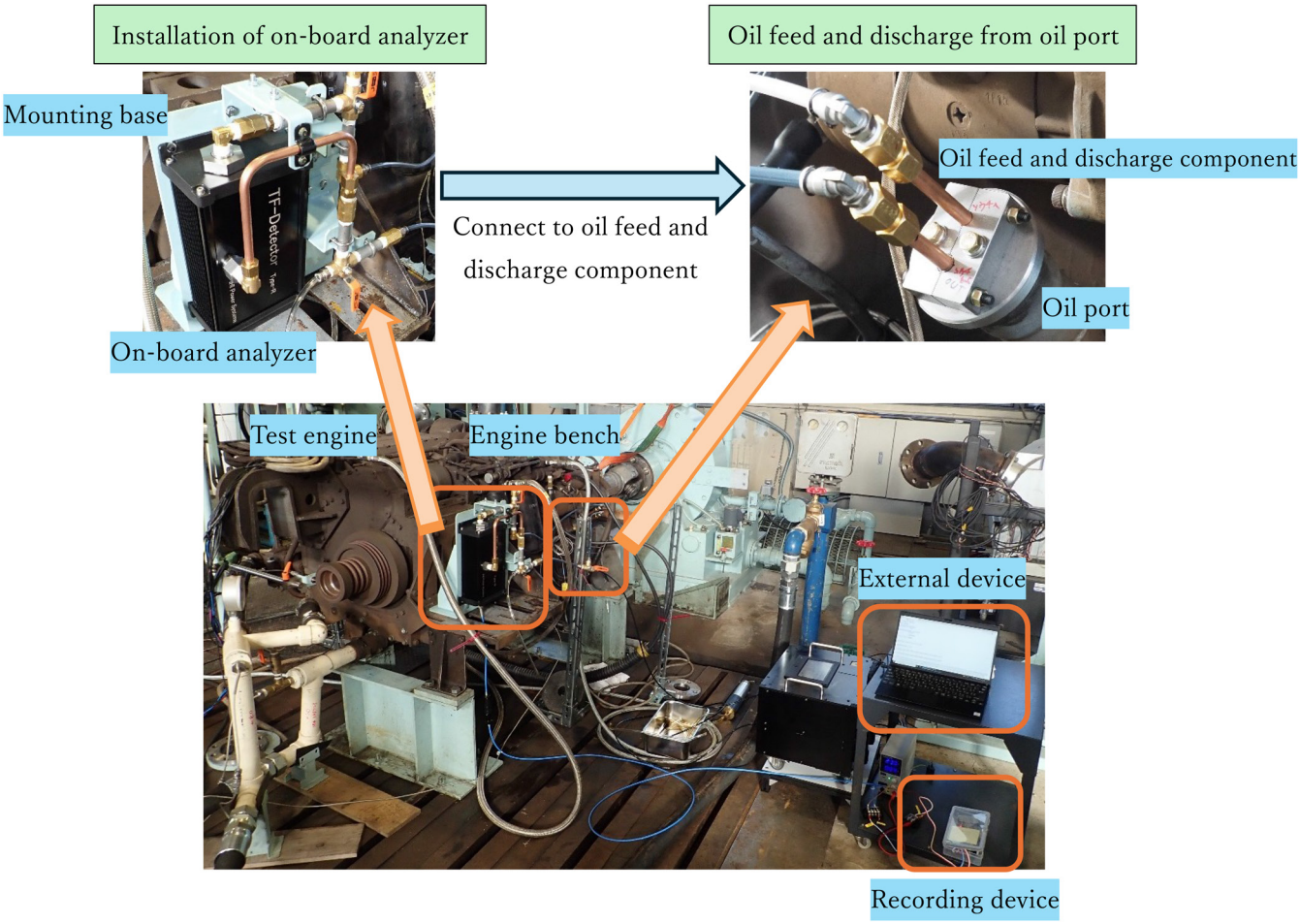

Fig. 3 Installation overview of condition monitoring system in engine bench test

lyzers. During these tests, the engine operated without any abnormalities, and the oil temperature, oil pressure, and exhaust temperature remained within normal ranges from start to finish.

4.3 Measurement results of iron powder density in engine oil

Figure 4 shows the results of the continuous measurement of iron powder density during the abnormal simulation tests. Although temporary disturbances were observed around 3600 seconds (just before the end of test No.1) and around 5010 seconds (the section affected by the power supply malfunction shown in Table 2), data acquisition was generally stable. The temporal changes in iron powder density are detailed as follows.

The measured iron powder density was around several ppm when SiC was not mixed into the engine oil. The iron powder density increased immediately when 0.01 wt% of SiC was added into the engine oil and the engine was rotated. This indicates that the sliding components inside the engine are wearing, resulting in the generation of iron wear particles. On the other hand, the increase in iron powder density slowed over time. For test No.1 and test No.2, which had a SiC density of 0.01 wt%, the iron powder density barely increased once it reached approximately 150 ppm. In test No.3, with a SiC density increased to 0.02 wt%, the iron powder density increased again, but ceased once it reached 190 ppm. In test No.4, which resumed operation after a prolonged shutdown, the iron powder density increased again, but stabilized at approximately 200 ppm. As shown in Table 1, the upper measurement limit of the on-board analyzer is 200 ppm. Therefore, iron powder density exceeding 200 ppm cannot be accurately measured. Measurements conducted using a stationary analyzer with an upper measurement limit of 1000 ppm showed that the iron powder density increased to 371 ppm by the end of test No.4. Furthermore, the iron powder density trends from test No.1 to test No.3 were consistent with the analysis results obtained by the stationary analyzer.

We conducted measurements of engine oil collected from commercial vehicles using the stationary analyzer and proposed 20 ppm as an abnormal judgment criterion [3]. The criteria value is unlikely to exceed 200 ppm, although it varies depending on vehicle models, engine types, etc. Therefore, a measurement upper limit of 200 ppm is considered sufficient for practical use in detecting engine malfunctions.

5. Practical performance evaluation of condition monitoring systems through field tests

Field tests using commercial railway vehicles were conducted to verify the performance and durability of the prototype condition monitoring system after it was installed on a commercial vehicle. In these tests, the condition monitoring system was temporarily installed on a diesel railcar, and vehicle running tests were conducted on the test track at a vehicle maintenance factory.

5.1 Temporary installation of the condition monitoring system on commercial vehicle

When installing the condition monitoring system on the commercial vehicle, the on-board analyzer and piping were secured to the engine using a mounting board, similar to the engine bench test. For oil feeding and discharge to the on-board analyzer, the component attached to the engine's oil port was used, with piping and fixtures connected via copper tubing. The power supply of DC 24 V for the on-board analyzer and recording device was supplied from the vehicle via an isolated DC/DC converter (24 V/24 V). The measured iron powder density data was acquired via Wi-Fi using an external device installed in the cabin. Additionally, data loggers installed on the vehicle recorded data including running direction, notch signals, speed, rotation speed of engine, engine oil temperature, and vibration acceleration in the front-to-back and left-to-right directions near the equipment.

5.2 Functional verification of the condition monitoring system

Prior to running tests on the test track, iron particle density was measured at various engine rotation speeds during idling the engine. This was done to verify the operation of the condition monitoring system and measuring instruments after their installation. Figure 5 shows how the measured iron powder density changes with engine rotation speed. The measured iron particle density, which was 4 to 6 ppm during idle rotation, increased approximately 7 to 8 seconds after the engine speed increased when the notch was engaged. When the engine returned to idle rotation, the measured value tended to decrease slightly after the engine speed dropped. The maximum measured iron powder density was approximately 14 ppm. Increases and decreases in the measured iron particle density were observed with changes in engine speed. However, when the engine returned to idle rotation, the measured value returned to approximately 4 ppm, which is the value prior to engaging the notch. No abnormalities

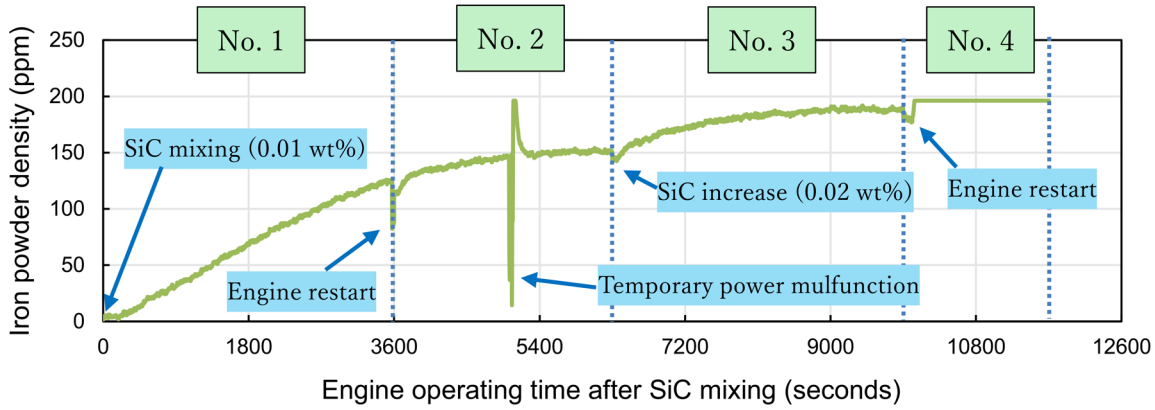

Fig. 4 Results of measuring iron powder density during abnormal simulation tests

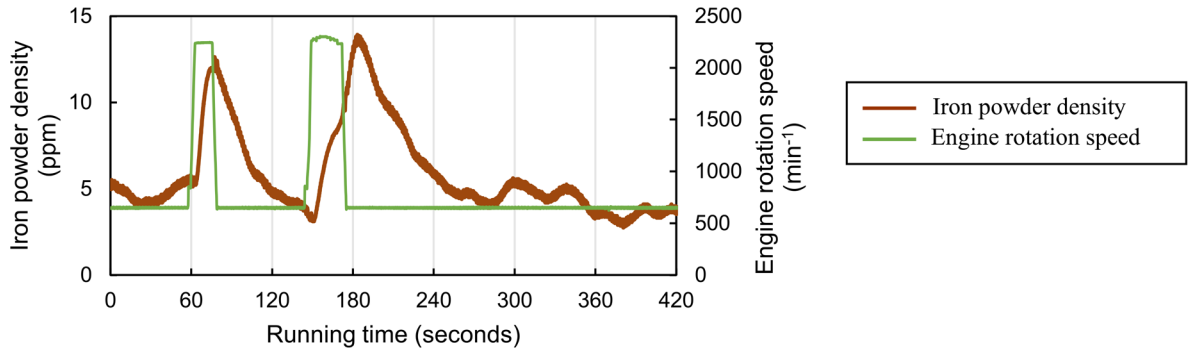

Fig. 5 Results of measuring iron powder density during abnormal simulation tests

were observed, such as issues with oil feeding and discharge during engine rotation or damage to the piping of the measuring equipment.

5.3 Vehicle running tests

During the on-site running tests, a test vehicle equipped with the temporary condition monitoring system was run on the test track (approximately 250 meters in length) at the vehicle maintenance factory. Table 3 shows the operating conditions for each test run. The operating conditions specified the notch and brake patterns up to the maximum speed for each test run. After reaching the maximum speed, the vehicle coasted to the stopping point.

Figure 6 shows the iron powder density during each test run. In nine of the test runs, excluding tests No. 1 and No. 9, an increase in measured iron powder density was observed approximately 7 to 8 seconds after an increase in engine speed. Furthermore, when the engine returned to idle rotation, the increased measured values gradually decreased, approaching levels similar to those before the test (4 to 6 ppm). This result is similar to those of the test described in 5.2.

Oil was sampled from the engine after the running tests, and the iron powder density in the engine oil was measured to be approximately 6 ppm, using an inductively coupled plasma emission spectroscopy (ICP method). This value was close to the measured iron particle density when the engine was idling. Therefore, the increase in measured values accompanying an increase in engine rotation speed is not considered to represent an actual increase in iron particle density. Rather, it is presumed to be caused by the structure or specifications of the oil sensor.

The nine test runs which showed an increase in measured values with increasing engine rotation speed were all performed with two or more notches and engine rotation speeds of 1000 min^{-1} or higher. Therefore, the increase in measured values may be caused by the high engine rotation speeds. However, the degree of increase varied from a maximum of 45 ppm (test No.3) to a minimum of 10 ppm (test No.11), and no significant trend was observed in relation to operating patterns. Therefore, further detailed verification is necessary to identify the cause.

During vehicle stops and coasting, no significant fluctuations in measured iron particle density were observed, except for a decrease in the increased iron particle density. Additionally, no damage to the piping, abnormalities in oil feeding or discharge, or oil leaks from the analyzer and connection points were observed throughout the entire running tests. Furthermore, Wi-Fi data communication was good within a range of approximately 50 meters from the recording device. These results of the running tests indicate that the prototype condition monitoring system functioned properly under these running conditions, except for an increase in measured iron particle density due to increasing engine rotation speed.

6. Application and challenges of the condition monitoring system

The following proposal outlines specific operational methods for applying the condition monitoring system to commercial vehicles.

1) During periodic inspections involving an engine overhaul, a condition diagnosis is conducted to determine the internal wear condition of the engine and formulate a vehicle repair plan.
2) During regular inspections and engine oil changes, a condition diagnosis is performed to detect abnormalities inside the engine and assess oil degradation.
3) During routine inspections and checks performed before train operation, a condition diagnosis is conducted to detect abnormalities inside the engine and prevent failures during vehicle operation.
4) When crew members detect signs of abnormality during vehicle operation, such as unusual noises or irregular exhaust, a condition diagnosis is performed to estimate the internal engine status as part of the process to determine the cause.
5) To collect data for condition-based maintenance (CBM) implementation, condition diagnoses are performed several to over ten times per day at predetermined intervals during vehicle operation. These diagnoses are typically performed at the starting and terminating stations of commercial trains.
6) Continuous condition monitoring is performed during engine operation to acquire data for CBM, including during vehicle operation.

As described in section 5.2, the condition monitoring system faces the challenge that an increase in engine speed affects the measured values. However, the system functions normally when the engine is idling. Therefore, data acquisition is possible during idling for all operational categories described above except No.6, and a condition monitoring system is considered applicable to commercial vehicles. Applying No.6 requires modifications, such as sensor adjustments, to suppress fluctuations in measured values even when the engine rotation speed increases due to notch insertion. Furthermore, when performing actual anomaly diagnosis, it is necessary to determine appropriate anomaly detection criteria based on accumulated measurement data and data analysis at the time of anomaly occurrence.

7. Conclusions

We conducted a prototype of an on-board analyzer and investigated data transfer methods to apply a condition monitoring system

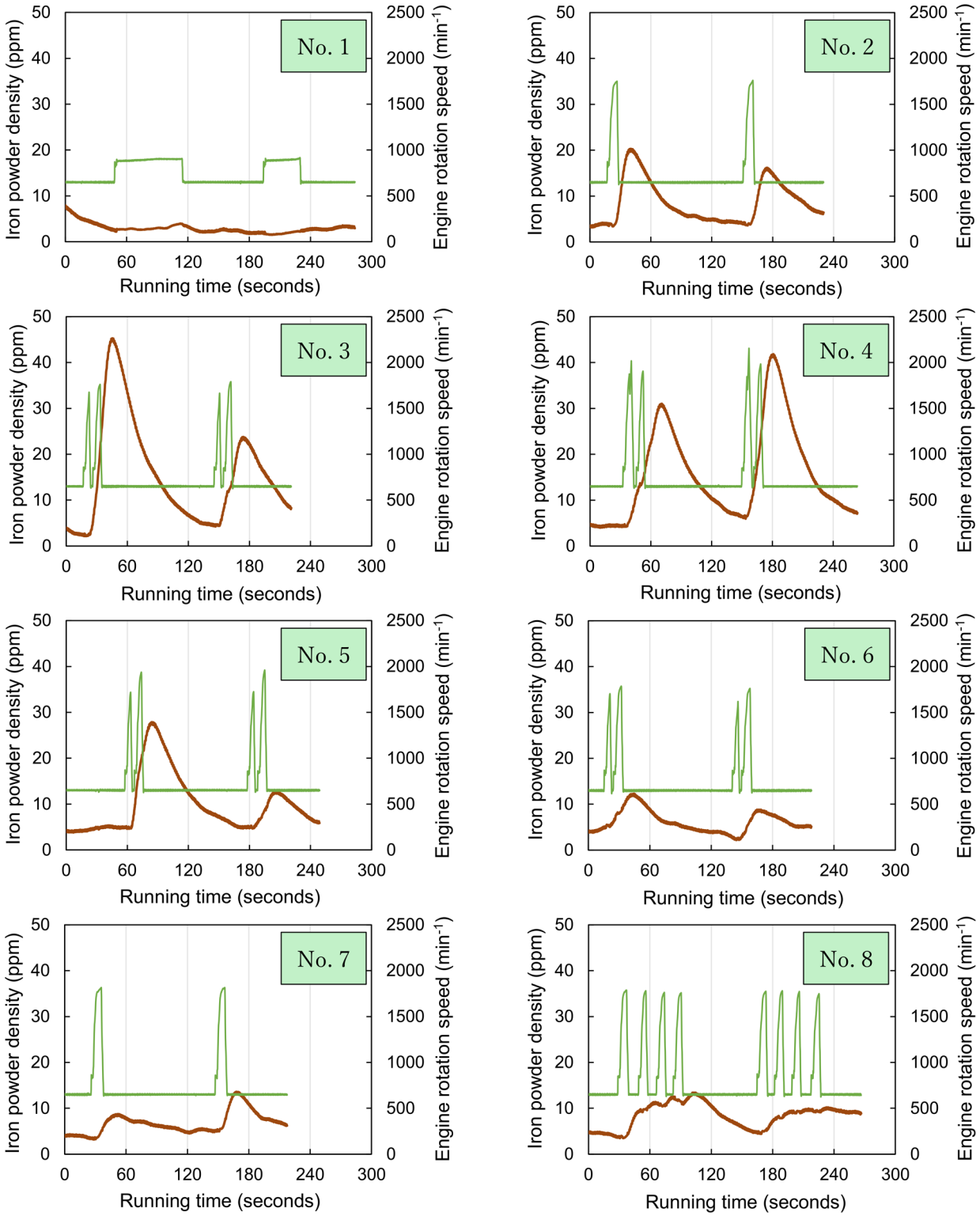

Fig. 6 Results of vehicle running tests

for driving equipment, such as engines, using oil sensors to commercial vehicles. We evaluated the system's performance using engine bench tests and field tests. As a result, the following findings were obtained.

1) We prototyped an on-board analyzer, which can be mounted on vehicles. It uses an oil sensor and a recording device which can transfer measurement data to general-purpose external devices via Wi-Fi. We confirmed that it can be installed on diesel railcar engines.
2) We confirmed through engine bench tests that a condition monitoring system comprising an on-board analyzer and recording device enables the detection of increased iron particle density in engine oil due to internal engine wear caused by foreign object ingress.

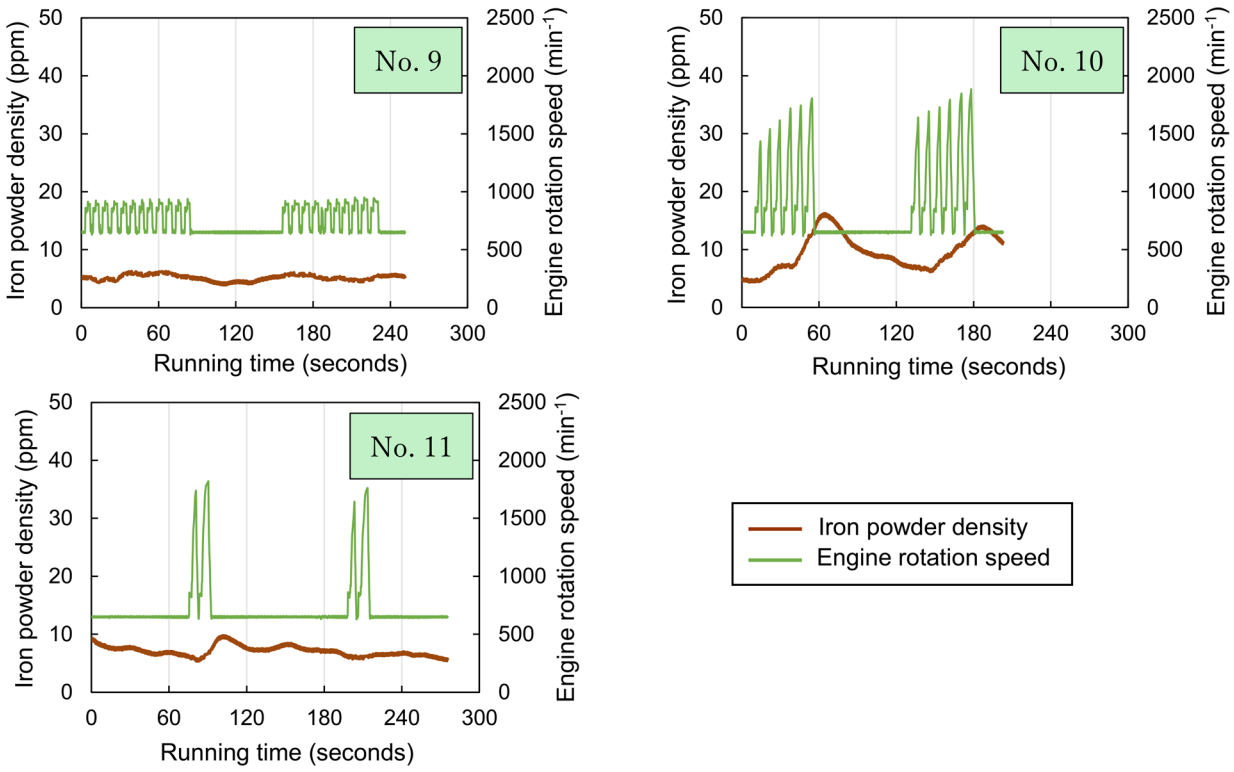

Fig. 6 Results of vehicle running tests

3) Vehicle running tests using commercial vehicles confirmed that system functions such as oil feed/drainage, measurement, and Wi-Fi data transmission operate normally during vehicle operation. However, it was identified as a challenge that the measured values are affected by an increase in engine rotation speed.

Acknowledgment

We would like to take this opportunity to express our sincere gratitude to Mr. Takashi Fujii and Mr. Isao Nishimoto of Mitsui E&S Co., Ltd., who jointly developed the on-board analyzer used in this research. We would also like to thank the Shikoku Railway Company personnel who provided invaluable assistance during the field tests.

References

[1] Suzuki, M., Hosoya, T., Nakamura, K., Sone, Y., "Failure Diagnosis on Damages of a Diesel Engine Caused by Contaminants through Analysis of Wear Particles in Oils," *RTRI Report*, Vol. 10, No. 8, pp. 17-22, 1996 (in Japanese).
[2] Suzumura, J., Kikawa, S., Ikoma, K., Takashige, T., "Abnormality Diagnosis of Diesel Engines and Hydraulic Torque Converters by using Portable Lubricating Oil Analyzer," *RTRI Report*, Vol. 34, No. 10, pp. 29-34, 2020 (in Japanese).
[3] Suzumura, J., Kikawa, S., "Condition Monitoring of Diesel Engines Using Oil Sensors," presented at *JAST tribology conference*, Tokyo, Japan, May 29-31,2023 (in Japanese).

Authors

Junichi SUZUMURA, Ph.D.
Senior Researcher, Lubricating Materials Laboratory, Materials Technology Division
Research Areas: Tribology, Lubricants

Kazuki IKOMA
Senior Researcher, Lubricating Materials Laboratory, Materials Technology Division
Research Areas: Tribology, Lubricants

Sadayuki KIKAWA
Senior Researcher, Lubricating Materials Laboratory, Materials Technology Division
Research Areas: Tribology, Lubricant

Tatsuro TAKASHIGE
Senior Researcher, Traction Systems Laboratory, Vehicle Technology Division
Research Areas: Drive System

Countermeasures of Low-frequency and Aerodynamic Noise Emitted from Shinkansen Trains

Mariko AKUTSU
Noise Analysis Laboratory, Environmental Engineering Division

Toki UDA
Environmental Engineering Division

When Shinkansen vehicles run in open sections at high-speed, bogie sections emit low-frequency noise and audible noise. For Shinkansen trains to be able to run at higher speeds, it is essential to reduce this aerodynamic noise. To understand the mechanisms generating low-frequency and audible noises, we conducted both field tests and low-noise wind tunnel tests. This paper describes a wind tunnel test method and investigates countermeasures against low-frequency and audible noises.

***Key words*:** *bogie section aerodynamic noise, open-section pressure fluctuations, wind tunnel test, microphone array*

1. Introduction

Pressure fluctuations and aerodynamic noise are produced when Shinkansen trains run at high speeds through open sections. These pressure fluctuations arise from viaduct vibrations and variations in the surrounding flow field as the train passes. They include quasi-static pressure fields near the train's front and rear ends, along with low-frequency aerodynamic pressure fluctuations that occur as the middle portion of the train passes through the section. In this report, pressure fluctuations are defined as frequency components at or below 100 Hz; among these, it is known that components in the 5-20 Hz range may cause rattling of fixtures in houses along the railway [1, 2]. Aerodynamic pressure fluctuations exhibit the characteristic that sound pressure levels rise in proportion to the sixth power of train velocity. Hence, clarifying these mechanisms and developing mitigation methods are important as train speeds increase.

Identifying the origins of aerodynamic pressure fluctuations is challenging due to their long wavelengths and the high velocity of Shinkansen trains. The Railway Technical Research Institute (RTRI) proposed installing a linear array of low-frequency sound level meters along actual Shinkansen tracks, and calculated ensemble averages from numerous train passages, and the analysis showed that major sources of pressure fluctuations are located at bogie sections and gaps between cars [3].

Aerodynamic noise refers to wind noise created by irregularities on the train's surface, not only in the bogie sections but also in pantographs and other components. In this paper, audible noise with a frequency at or above 100 Hz is defined as aerodynamic noise. Because aerodynamic noise frequencies are regulated by environmental standards for areas near Shinkansen lines, reducing such noise and ensuring compliance with these standards are vital for improving the quality of the environment in the vicinity of high-speed rail lines as speeds increase.

Both pressure fluctuations and aerodynamic noise stem from aerodynamic effects, so they can be assessed using a wind tunnel. For this reason, RTRI is investigating noise mitigation methods with scale models in a large-scale low-noise wind tunnel, with the goal of reducing pressure fluctuations and aerodynamic noise originating from the bogie section [4-6]. This report describes the measurement procedures used in the large-scale low-noise wind tunnel and presents the proposed noise reduction countermeasures developed in this research. This study represents a fundamental stage of investigation toward implementing mitigation measures and includes some countermeasures for which the feasibility of installation on actual trains has not yet been considered.

2. Wind tunnel test

2.1 Large-scale low-noise wind tunnel

Experiments were conducted in the large-scale low-noise wind tunnel ("low-noise wind tunnel") owned by RTRI in Maibara City, Shiga Prefecture. This wind tunnel was specifically designed for acoustic testing. The anechoic measurement chamber, along with inner wall features such as noise-absorbing concrete walls and silencers, ensures exceptional low-noise performance, with a background level of 75.6 dB(A) at 300 km/h, measured 3 m downstream and 4.5 m laterally from the nozzle [7]. The open test section used for this study measured 3.0 m in width, 2.5 m in height, and 8 m in length, and was capable of producing airflows up to 400 km/h.

2.2 1/5-scale train model

A 1/5-scale train model was employed to reproduce pressure fluctuations and aerodynamic noise arising from the bogie section. The model replicated the underside of a Shinkansen train, positioning the bogie near the rear, as depicted in Figs. 1 and 2. The model is 6,400 mm in length and has a smooth contour except for the bogie region and the mounting area, in order to minimize aerodynamic noise from portions other than the bogie section. A highly detailed precision bogie model replicating a typical bogie structure was installed within a bogie storage space in the car body ("bogie cavity").

Figure 3 illustrates the wind tunnel test. The train model was mounted to the ground plate via a simplified rail setup. Airflow was applied, and measurements were taken while both the train model and ground plate remained stationary. Previous research has shown that, in actual operation, the underside air velocity differs between the leading car and the second or subsequent middle cars [8]. We sought to reproduce the middle car conditions by setting the gap between the underside of the model and the simulated track to 80 mm, which corresponds to one-fifth of the actual value, and raising the wind tunnel nozzle height above the ground plate to utilize the

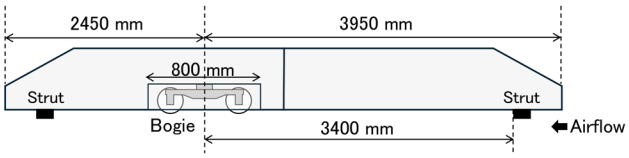

Fig. 1 Overview of 1/5-scale train model

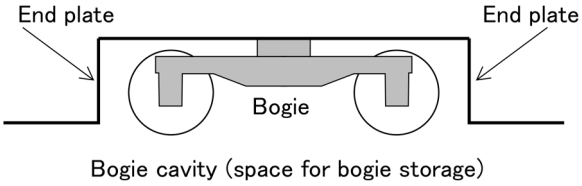

Fig. 2 Overview of bogie section

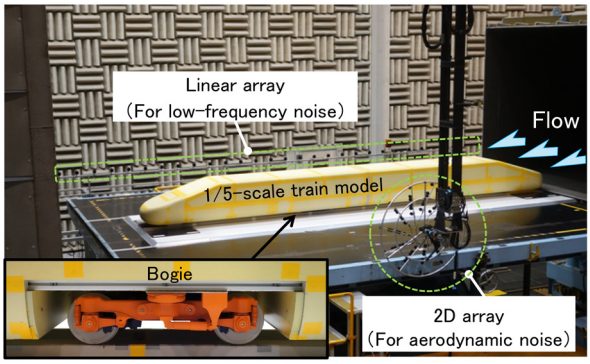

Fig. 3 Wind tunnel test
(A full cover was placed over the bogie section during measurement.)

free shear layer formed downstream of the nozzle exit [9].

Since a 1/5-scale model was used, the recorded sound wavelengths in the wind tunnel test must be scale-converted to actual train frequencies. Wavelength and frequency are inversely related, so the true frequency (f_{real}, "real frequency") for a scale of 1/n can be expressed in terms of the measured frequency (f_{meas}) as follows:

$$f_{real} = f_{meas} / n \quad (1)$$

From Section 3 onwards, the real frequency will be used.

2.3 Measurement equipment

A microphone array placed beside the train model was used to capture pressure fluctuations and aerodynamic noise from the bogie section. A microphone array consists of multiple microphones arranged in a geometric pattern, where the direction of noise arrival and strength can be estimated from the phase differences between the received signals.

The microphone used for measuring pressure fluctuations ("linear array") contained 29 microphones aligned over a span of 8.4 m (42 m at full scale) at 0.3 m intervals (1.5 m at full scale), positioned 4 m (20 m at full scale) to the side of the train model. This setup enabled a 1D mapping of sound source distribution for pressure fluctuations along the length of the train. Figure 4 shows the directivity pattern of the linear array employed in this experiment. Higher gain values correspond to greater sensitivity in that direction. The gain width (main lobe) at 0 m in the primary flow direction shows

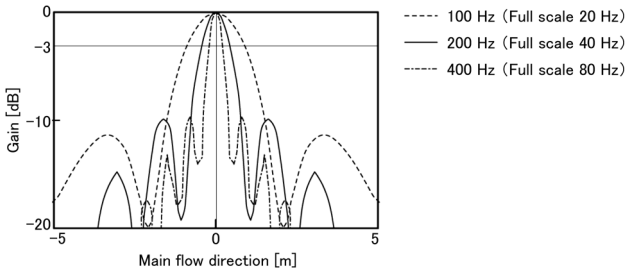

Fig. 4 Directivity of linear array (4 m from array)

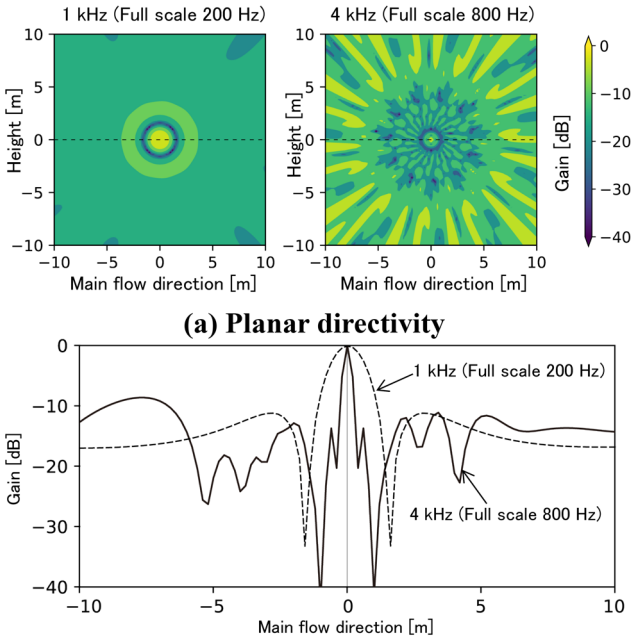

Fig. 5 Directivity of 2D array (3.5 m from array)

that the −3 dB resolution at 100 Hz (real frequency of 20 Hz) is confined within ±1 m. This capability allows for clear separation of the bogie section under study from other low-frequency noise sources, such as support for the train model and the wind tunnel's nozzle and collector.

The microphone array used to measure aerodynamic noise ("2D array") was produced by HBK (Hottinger Brüel & Kjær) and consisted of 66 microphones arranged in a circular configuration. This 2D layout enables the determination of the spatial distribution of sound sources on a plane. Figure 5 shows the directional characteristics at 1 kHz and 4 kHz. In the 2D plots of Fig. 5(a), the main lobe centered in the array exhibits the highest gain for both frequency bands, indicating strong sensitivity at the front of the array. We can see from the main lobe that its area is smaller at 4 kHz than at 1 kHz, showing a sharper directivity. Outside the main lobe region, a radial directivity pattern with side lobes appears more prominently at 4 kHz. These tendencies are also seen in the horizontal directivity at 0 m height in Fig. 5(b). Namely, at lower frequencies, the main lobe is wider and with fewer side lobes, giving a high signal-to-noise (S/N) ratio. Meanwhile, at higher frequencies, the narrower main lobe and multiple side lobes result in a trade-off between resolution and S/N ratio. These results were consistent with typical

characteristics of microphone arrays. The −3 dB resolution of this 2D array was roughly ±0.6 m at 1 kHz (real frequency of 200 Hz), sufficient for evaluating aerodynamic noise in the present wind tunnel test.

We installed the linear array on the left side of the flow and the 2D array on the right, as illustrated in Fig. 3, in order to enable simultaneous measurement of pressure fluctuations and aerodynamic noise. For both the linear and 2D arrays, evaluations of pressure fluctuations and aerodynamic noise were based on spatial integration of sound pressure levels over the area including the bogie section, as determined from the sound source distribution. Furthermore, aerodynamic noise levels were subjected to A-weighting, in accordance with environmental noise evaluation standards.

3. Noise reduction countermeasure proposal

This section describes the mechanisms behind pressure fluctuations and aerodynamic noise generation. Pressure fluctuations are thought to arise from the internal volume of the bogie cavity, such as self-induced vortex oscillations at the front and rear lower edges of the bogie cavity. Accordingly, altering the shape of the bogie cavity is considered a potential way to suppress these noise sources. Aerodynamic noise, on the other hand, is generated when high-speed airflow strikes bogie components, and such noise is known to originate from lower bogie components, namely wheels, traction motors, and gears, as well as from the lower edge of the downstream cover plate [10]. Consequently, preventing high-speed airflow from impacting bogie components is regarded as an effective countermeasure.

Table 1 summarizes the proposed noise reduction countermeasures based on these findings. In the table classification, sound source countermeasures aim to reduce the generation of pressure fluctuations and aerodynamic noise at their origin, whereas propagation countermeasures mitigate the observed noise by isolating or absorbing sound during its transmission. Shinkansen trains on commercial lines operate in both directions, so all the countermeasures described in this section are designed to be symmetrical across the left and right sides as well as the front and rear of the bogie section.

Table 1 Proposed noise reduction countermeasures in the bogie section

Countermeasure	Classification	Variation
Deflector (Fig. 6)	Sound source countermeasure	Lower end of cavity
		Inside cavity
Flat undercover (Fig. 7)	Sound source & propagation countermeasure	Width 15 mm (75 mm in full scale)
		Width 35 mm (175 mm in full scale)
		Width 25 mm + absorber
Angled end plate (Fig. 8)	Sound source countermeasure	–
Side cover protrusion (Fig. 9)	Sound source countermeasure	–
Cavity top unit (Fig. 10)	Sound source & propagation countermeasure	Rectangular
		Rounded
Membrane absorber (Fig. 11)	Propagation countermeasure	–

3.1 Deflector

As shown in Fig. 6, the deflector has a downward-pointing triangular configuration and is designed to redirect the airflow entering the bogie section downward, thereby reducing the velocity of the air striking bogie components. The deflector has a uniform profile in the transverse direction and is installed in two positions, namely at the lower edge of the cavity and inside the cavity itself. The deflector located inside the cavity is mounted and secured using arm-shaped components extending from the axle box.

3.2 Flat undercover

The flat undercover, shown in Fig. 7, consists of a horizontal plate attached to the bottom edge of the bogie-side cover (full cover). Its function is to obstruct lateral airflow entering from the train's side while enveloping the lower end of the side cover, and to block aerodynamic noise from propagating outward from the bogie cavity. In this study, we examined the following three configurations. Two were with different lengths in the transverse direction, and one was with the absorber applied to the top surface of the flat undercover. PET wool, which is a commonly used absorber, was employed for this purpose (the same applies hereafter).

3.3 Angled end plates

Figure 8 illustrates the angled end plates, whose front and rear panels are inclined 60 degrees from the horizontal. These plates are

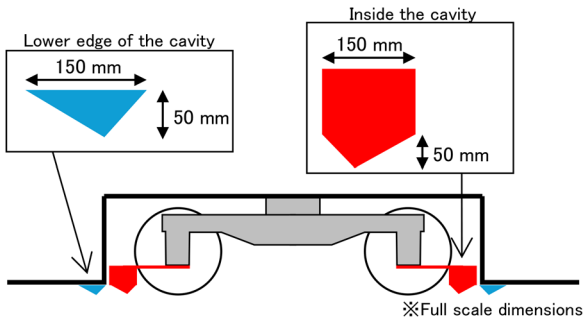

Fig. 6 Deflector

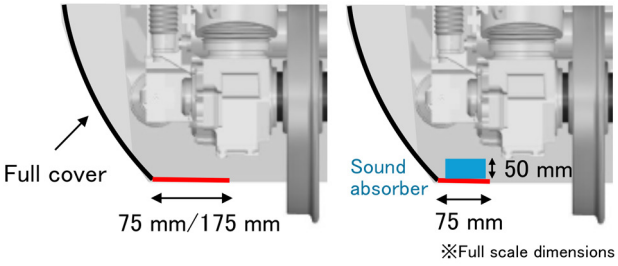

Fig. 7 Flat undercover

intended to modify the airflow inside the bogie cavity to lessen pressure fluctuations.

3.4 Side cover protrusions

As depicted in Fig. 9, the side cover protrusions extend from the lower edges of the train's side covers (excluding the bogie section) by 30 mm (150 mm at full scale). This design aims to suppress lateral airflow fluctuations on the underside of the train and alter the flow impacting the bogie section. In this experiment, the protrusions were fitted only on the upstream side of the bogie, but for application to real rolling stock, they are expected to extend along the entire train length, excluding the bogie region.

3.5 Cavity top unit

As shown in Fig. 10, the cavity top unit is a device consisting of a component containing an absorber installed at the corner between the front and rear cover plates and the upper surface of the bogie cavity. Its role is to reduce pressure fluctuations arising from airflow variations inside the cavity and to lower aerodynamic noise through the use of an absorber. The surface of the unit is made from a perforated plate with a sufficiently large aperture, ensuring the effectiveness of both the structural unit and the embedded absorber.

3.6 Membrane absorber

The membrane absorber, shown in Fig. 11, is designed to reduce pressure fluctuations caused by membrane resonance. This countermeasure uses a polyvinyl chloride (PVC) membrane attached to the upper surface of the bogie cavity. A 10 mm space (50 mm at full scale) was created beneath the membrane as an air gap, which was filled with an absorber.

4. Wind tunnel test results

4.1 Verification of S/N ratio for basic configuration

This section presents an overview of the wind tunnel test results, focusing on the baseline condition, without countermeasures, and smooth condition, in which the bogie was removed and the cavity was sealed. Figure 12 shows the data obtained using an omnidirectional microphone. Because the S/N ratio of pressure fluctuations tended to decrease at 320 km/h, subsequent analyses present pressure fluctuation results at 260 km/h and aerodynamic noise results at 320 km/h.

The omnidirectional microphone, which has nearly equal sensitivity in all directions, was positioned at the center of the 2D array. As a result, the recorded data include not only aerodynamic noise generated by the bogie section under study but also noise produced by the wind tunnel itself and the supporting structures of the train model. Figure 12 indicates that the sound pressure level for pressure fluctuations under the smooth condition exceeded that under the baseline condition. The smooth condition was free of irregularities that could act as sound sources, so its higher level suggests that the omnidirectional microphone did not properly capture the actual pressure fluctuations. Furthermore, although aerodynamic noise levels under the baseline condition were higher than those under the smooth condition, the difference was only about 5 dB at most, which was insufficient to achieve the S/N ratio necessary for reliable noise evaluation.

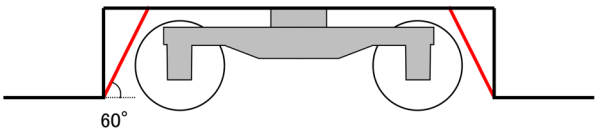

Fig. 8 Angled end plate

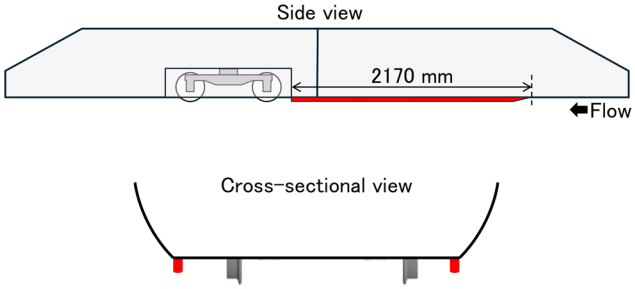

Fig. 9 Side cover protrusion

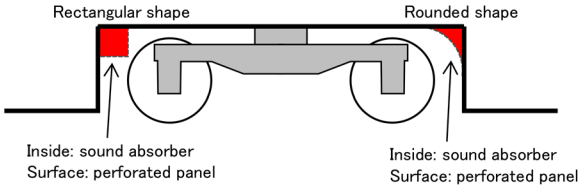

Fig. 10 Cavity top unit

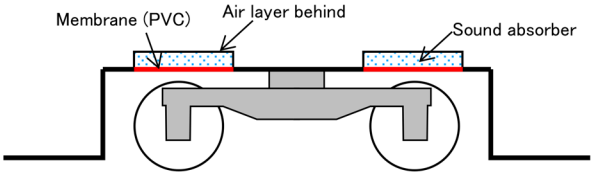

Fig. 11 Membrane absorber

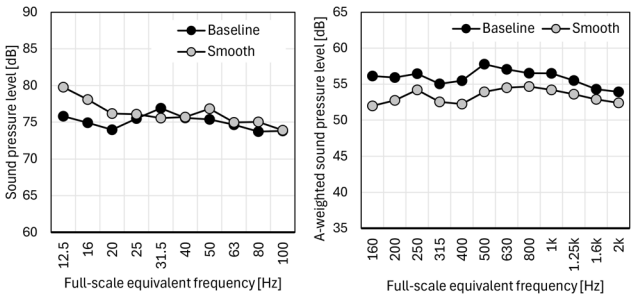

Fig. 12 Measurement results using omnidirectional microphone (Left: Pressure fluctuations at 260 km/h, Right: Aerodynamic noise at 320 km/h)

Next, Fig. 13 presents the results obtained using the linear and 2D arrays. The baseline condition produced higher sound pressure levels than the smooth condition for both pressure fluctuations and aerodynamic noise. In the aerodynamic noise results, the difference between baseline and smooth conditions represented the aerodynamic noise produced by the bogie section. This difference was most prominent in the 250–400 Hz range, indicating that the strongest aerodynamic noise occurred within these frequency bands. In addition, the sound pressure level difference was at least 10 dB

across all frequency ranges, confirming that a sufficient S/N ratio was achieved. For pressure fluctuations, the baseline condition also showed higher levels than the smooth condition, though the difference was smaller, ranging from approximately 2 to 10 dB. Nevertheless, a comparison with the omnidirectional microphone results in Fig. 12 clearly demonstrated the ability to detect pressure fluctuation generation in the linear array measurements. However, even with the linear array, the S/N ratio was low in the 31.5 Hz band, so in this paper, data within that frequency band are treated as reference values only. Moreover, because these spectra are derived from wind tunnel tests, they differ from those produced by real Shinkansen bogie sections. Consequently, variations in sound pressure levels across frequency bands are used for verification purposes.

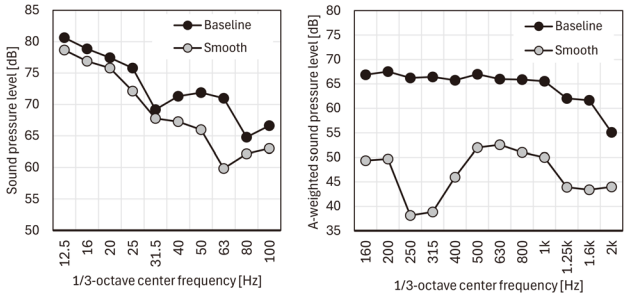

Fig. 13 Microphone array measurement results (Left: Pressure fluctuations at 260 km/h, Right: Aerodynamic noise at 320 km/h)

4.2 Noise reduction countermeasures

This section discusses the results for cases where noise reduction countermeasures were applied, based on measurements obtained with microphone arrays in the wind tunnel. Note that for some countermeasures, a single measurement result is presented, whereas for others, the values represent the average of multiple trials.

4.2.1 Deflector

Figure 14 presents the variations in pressure fluctuations and aerodynamic noise observed when the deflector countermeasure was applied. This figure compares sound pressure level differences relative to measurements taken under basic (no-countermeasure) conditions within the same series. Installing the deflector at the bottom of the cavity effectively lowered pressure fluctuations below 31.5 Hz and decreased aerodynamic noise at frequencies above 400 Hz. Conversely, the rise in aerodynamic noise sound pressure below 250 Hz is thought to originate from wheel-related aerodynamic noise caused by the deflected downward airflow striking the wheels. The deflector placed inside the cavity increased pressure fluctuations below 31.5 Hz but also reduced fluctuations above 40 Hz, and diminished aerodynamic noise across a wide frequency band. It should be noted that above 400 Hz, the sound pressure level surpassed that achieved with the deflector located at the bottom of the cavity.

This reduction effect probably results from the downward diversion of underside airflow by the deflector. However, because the extent of sound pressure reduction varies with frequency for each type of deflector, it is advisable to select an appropriate deflector based on the frequency spectrum of the actual train.

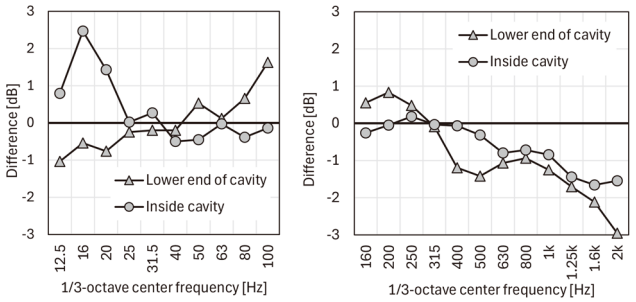

Fig. 14 Noise reduction effect of deflector (Left: Pressure fluctuations at 260 km/h, Right: Aerodynamic noise at 320 km/h)

4.2.2 Flat undercover

Figure 15 displays the results for the flat undercover. The pressure fluctuation reduction was greatest at a width of 35 mm (175 mm at full scale) across almost all frequency bands, and almost no reduction was observed at a width of 25 mm (125 mm at full scale). The 35 mm width represented the broadest condition examined, so its effectiveness is thought to stem from alterations in airflow patterns within the bogie section. By contrast, the 25 mm width, when used together with an absorber, reduced pressure fluctuations in nearly all frequency bands except 31.5 Hz. The 31.5 Hz band might, in fact, be more effective, though this could not be verified due to an insufficient S/N ratio in the measurements. Similarly, the 35 mm width slightly outperformed the 25 mm width in reducing aerodynamic noise. When combined with the absorber, both the flat undercover and the absorber demonstrated clear benefits, decreasing aerodynamic noise by roughly 1 dB in nearly all frequency bands.

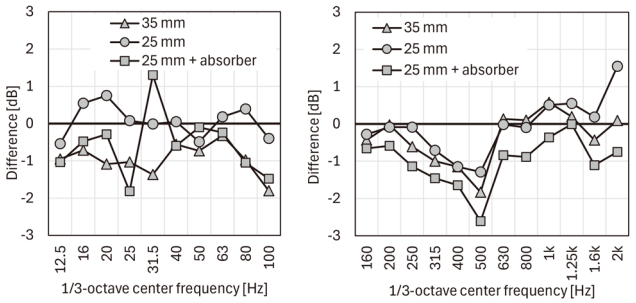

Fig. 15 Noise reduction effect of flat undercover (Left: Pressure fluctuation at 260 km/h, Right: Aerodynamic noise at 320 km/h)

4.2.3 Angled end plates

Figure 16 shows the results obtained for the angled front and rear end plates. This countermeasure proved particularly effective at reducing pressure fluctuations below 63 Hz. This outcome is attributed to the reduced bogie cavity volume and modified airflow resulting from the altered cover plate angles. In contrast, aerodynamic noise levels slightly increased above 250 Hz, which is presumed to result from modified internal flow patterns within the cavity. These findings indicate that the angle of the cover plates influences aerodynamic noise characteristics as well.

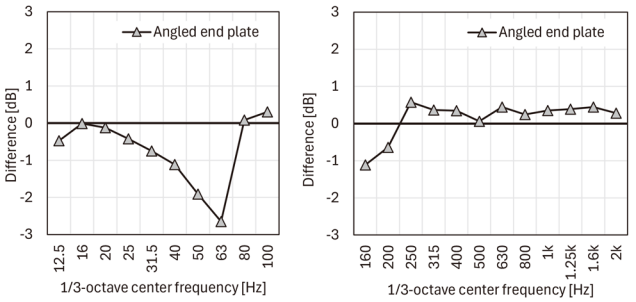

Fig. 16 Noise reduction effect of angled end plates (Left: Pressure fluctuation at 260 km/h, Right: Aerodynamic noise at 320 km/h)

4.2.4 Side cover protrusion

Figure 17 presents the results for the side cover protrusion configuration. Pressure fluctuation reduction appeared across multiple frequency ranges, with particularly strong suppression at 20 Hz and 40 Hz, so modifying the protrusion's shape could allow targeted reduction at specific frequencies. However, a slight rise in aerodynamic noise sound pressure levels was seen over nearly all frequency bands, showing no measurable noise reduction effect. Increases over 0.5 dB were observed, especially above 1 kHz, suggesting that the protrusion itself could be a new source of aerodynamic noise.

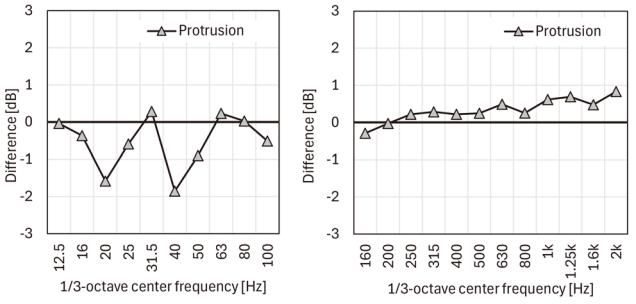

Fig. 17 Noise reduction effect of side cover protrusions (Left: Pressure fluctuation at 260 km/h, Right: Aerodynamic noise at 320 km/h)

4.2.5 Cavity top unit

Figure 18 illustrates the results for the cavity top unit configuration. Both rectangular and rounded configurations decreased sound pressure levels for pressure fluctuations across almost all frequencies above 25 Hz. This improvement likely arises from reduced bogie cavity volume and altered flow behavior following installation of the cavity top unit structure. Aerodynamic noise was also diminished in almost all frequency bands, reflecting the acoustic absorption performance of the absorber contained inside the unit.

4.2.6 Membrane absorber

Figure 19 presents the results for the membrane absorber configuration. Reductions in pressure fluctuations were observed between 25 Hz and 63 Hz, but aerodynamic noise was hardly affected. Membrane absorbers perform best at relatively low frequencies, so the observed outcome confirms that the membrane's acoustic absorption properties were active. Airtight materials such as the PVC sheet used in this test can form the membrane, so this countermeasure offers easy maintenance advantages when installed on actual trains.

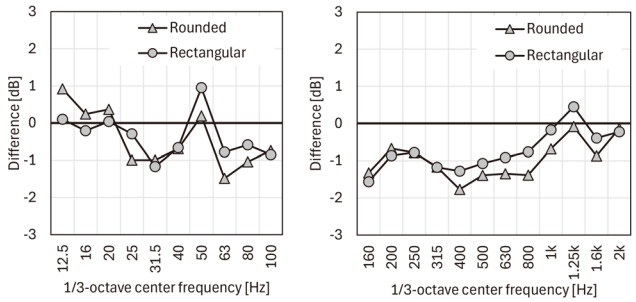

Fig. 18 Noise reduction effect of cavity top unit (Left: Pressure fluctuation at 260 km/h, Right: Aerodynamic noise at 320 km/h)

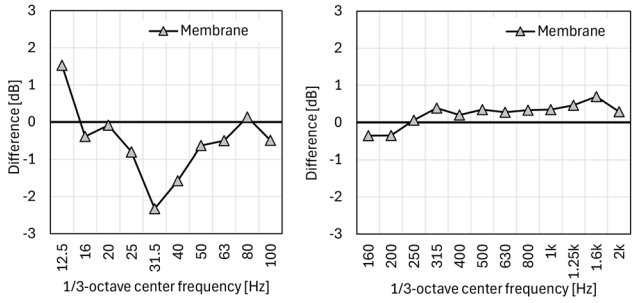

Fig. 19 Noise reduction effect of membrane absorber (Left: Pressure fluctuation at 260 km/h, Right: Aerodynamic noise at 320 km/h)

5. Conclusion

This paper describes a method for measuring aerodynamic pressure fluctuations and aerodynamic noise generated by the bogie section of a Shinkansen train in a large-scale, low-noise wind tunnel and develops countermeasures to mitigate both phenomena. Two types of microphone arrays were used simultaneously to capture pressure fluctuations and aerodynamic noise. The results confirmed that angled end plates, side cover protrusions, and membrane absorbers reduce pressure fluctuations. Meanwhile, deflectors, flat undercovers, and cavity top units effectively suppress both pressure fluctuations and aerodynamic noise. This study serves as a foundational investigation into noise reduction countermeasures. Building on these results, further research will pursue the development of practical countermeasures suitable for implementation on operating trains.

References

[1] Takami, H., Kikuchi, K., Maekawa, H., Kurita, T., and Wakabayashi, Y., "Low-frequency noise radiated from a high-speed train passing an open section," *Transactions of the Japan Society of Mechanical Engineers (B)*, Vol. 73, No. 735, 2007 (in Japanese).

[2] Takami, H. and Kikuchi, K., "Analysis of wayside low-frequency noise from a high-speed train," *RTRI Report*, Vol. 23, No. 7, 2009 (in Japanese).

[3] Uda, T., Kitagawa, T., Wakabayashi, Y., and Kurita, T., "Identification

of aerodynamic pressure fluctuations generated from high-speed trains passing an open section," *Transactions of the Japan Society of Mechanical Engineers*, Vol. 85, No. 879, 2019 (in Japanese).
[4] Uda, T. and Kitagawa, T., "Numerical simulation and wind tunnel test on aerodynamic bogie noise in high-speed trains," *Proceedings of the JSME Fluid Engineering Conference*, 2019 (in Japanese).
[5] Uda, T. and Kitagawa, T., "Analysis of flow and aerodynamic noise near the bogie region of high-speed railway vehicles," *Proceedings of the Autumn Meeting of the INCE/Japan*, 2019 (in Japanese).
[6] Uda, T. and Akutsu, M., "Sound source distribution of high-speed trains and reduction of aerodynamic bogie noise," *INTER-NOISE Conference Proceedings*, pp. 3709–3716(8), 2022 (in Japanese).
[7] Ido, A., Zenda, Y., Kondo, Y., Matsumura, G., Suzuki, M., and Kitagawa, T., "Basic performance of large-scale low-noise wind tunnel," *RTRI Report*, Vol. 13, No. 12, 1999 (in Japanese).
[8] Uda, T., Wakabayashi, Y., Kurita, T., Iwasaki, M., Yamazaki, N., and Ido, A., "Velocity profile under Shinkansen vehicle on slab track," *Transactions of the Japan Society of Mechanical Engineers*, Vol. 81, No. 830, 2015 (in Japanese).
[9] Yamazaki, N., Nagakura, K., Kitagawa, T., Uda, T., and Wakabayashi, Y., "An evaluation method for aerodynamic noise generated from the lower part of Shinkansen train," *RTRI Report*, Vol. 29, No. 5, 2015 (in Japanese).
[10] Uda, T. and Kitagawa, T., "Development of measurement method for aerodynamic bogie noise using porous plate," *RTRI Report*, Vol. 34, No. 3, 2020 (in Japanese).

Authors

Mariko AKUTSU, Dr.Eng.
Senior Researcher, Noise Analysis Laboratory, Environmental Engineering Division
Research Areas: Acoustics, Aerodynamic Noise, Railway Noise

Toki UDA, Ph.D.
Director, Head of Environmental Engineering Division
Research Areas: Aerodynamic Noise, Railway Noise

Development of a Method for Diagnosing Deterioration of Wayside Equipment using Forward-facing Train Images

Riho MAEDA **Hiroki MUKOJIMA** **Nozomi NAGAMINE**
Image Analysis Laboratory, Information and Communication Technology Division

Wayside equipment is installed both within stations and at different locations between them, making inspection and management labor-intensive. With the decline in maintenance staff, improving efficiency in equipment management has become essential. To address this issue, we developed a system that enables remote monitoring of trackside equipment using forward-facing train images captured by an onboard camera. The system estimates kilometrage, automatically detects equipment, and estimates deterioration of signalling equipment boxes. This paper presents the system overview, accuracy evaluation, and prospects for long-term deterioration monitoring.

***Key words*:** *trackside equipment, image processing, diagnosing deterioration, AI*

1. Introduction

Trackside equipment is installed at scattered locations along a railway line, including within station premises and between stations. Consequently, facility management tasks such as identifying equipment types and positions, and conducting individual inspections require a substantial amount of manpower and time. Considering the ongoing decline in the working population due to demographic changes in Japan, improving the efficiency of these maintenance activities has become an urgent issue.

To address this challenge, we developed a system that allows maintenance personnel to evaluate wayside conditions remotely. The system can automatically detect 22 types of trackside equipment and diagnose deterioration of signal equipment boxes [1][2]. The system consists of a commercially available video camera and a suction cup mount, which are installed on the windshield of the driver's cab to capture forward-facing images from the train.

This paper first provides an overview of the deterioration diagnosis system using forward-facing images captured from the train This is followed by detailed explanations and accuracy evaluations of each processing module.

2. Proposed system

2.1 System overview

To enable simple and cost-effective acquisition of data, commercially available video cameras are affixed to the train cab window using suction-cup mounts and record forward-facing images of the railway line. Examples of the image acquisition system and the images captured by it are shown in Fig. 1 and Fig. 2. Hereafter, such images are referred to as "forward-facing train images."

The system uses these images to perform kilometrage estimation for each frame, generates long bird's-eye view images of the track surface, and automatically detects trackside equipment using AI and image processing. Additionally, the system estimates the visual deterioration level of the detected equipment for deterioration diagnosis. A schematic diagram of the system is shown in Fig. 3, and the main processing steps are summarized below:

1. **Generation of long bird's-eye view images of the track surface:**
   The region of the track surface in the forward-facing image is converted into a bird's-eye view. Consecutive frames are stitched together to create a long, continuous top-view image, as if the track surface were photographed from directly above.
2. **Kilometrage estimation:**
   Pixel displacement between image frames is converted into a real-world distance to estimate the train speed and traveled distance. The system assigns kilometrage information to each frame by inputting the start and end kilometrage values.
3. **Automatic equipment recognition:**
   A total of 22 types of wayside signalling and related equipment are detected using an AI model for object detection. The detected results are output as bounding boxes.

Fig. 1 Image acquisition system

Fig. 2 Forward-facing train images

4. Deterioration evaluation of signal equipment boxes:
The system estimates the visual deterioration level of signal equipment boxes for detected signals. The model is trained as a classification problem. During inference, the deterioration score is obtained as a weighted sum of class probabilities and output as a continuous value.

Sections 3.2 to 3.3 describe processes (1) to (3), while Chapter 4 provides details of the deterioration estimation in (4).

2.2 Generation of long track-surface bird's-eye images

Images captured from the train cab show the track surface as a trapezoid, appearing smaller towards the upper part of the frame. Therefore, the first step is to apply a projective transformation to generate a bird's-eye view of the track surface, as if it were viewed from above.

Next, to generate a long continuous image, the obtained bird's-eye view images are stitched together. A bird's-eye view image is created for each frame of the forward-facing train video. Then, the distance from the bird's-eye view image of the previous frame is calculated, and the images are overlaid according to this distance. This inter-frame distance is expressed as pixel displacement and is calculated using optical flow. Optical flow is a technique that analyzes changes in pixel intensity across frames to estimate the motion field, including the direction and the amount of movement of objects.

Based on the calculated pixel displacement, the position of each bird's-eye view image is adjusted along the track direction, and images are stitched with the rail position as a reference. Smooth transitions at the seams are created by applying multiband blending [3][4] to overlapping regions, where image opacity is weighted according to spatial frequency.

Figure 4 shows an example of the resulting long bird's-eye view image of the track surface, demonstrating how short segments of the track are successfully combined into a continuous image along the railway line.

2.3 Kilometrage estimation method

In order to capture forward-facing images from the train, the bird's-eye-view images and equipment detection results generated by this system to be useful in practical maintenance operations, it is essential that they are associated with actual kilometrage information. Therefore, the system estimates the travel distance and speed from the forward-facing images and assigns kilometrage values to each frame based on the position of the vehicle.

To calculate the distance and speed between frames, the system first accumulates pixel-level displacements obtained from optical flow to compute the relative travel distance (in pixels) over the entire section. This enables the relative distance of each frame from the start of recording to be determined.

Next, to convert this relative pixel-based distance into an actual kilometrage value, two or more reference points with known kilometrage (e.g., stations, ground coils) are used. The pixel-based distances between these reference points and the current frame are measured, and the kilometrage of each frame is interpolated. Specif-

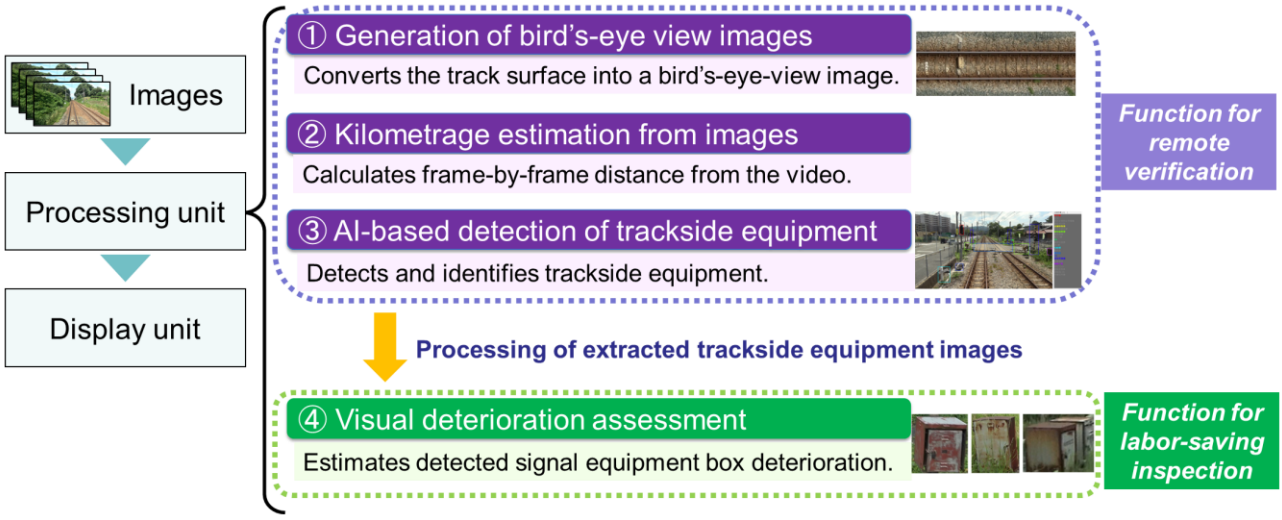

Fig. 3 Schematic diagram of the system

Fig. 4 Example of a generated extended bird's-eye view image of the track surface

ically, as shown in Fig. 5, if the relative pixel displacement at the frame of interest S is D_S, and the pixel displacements and known kilometrages of reference points R_1 and R_2 are (D_{R1}, X_{R1}) and (D_{R2}, X_{R2}), respectively, then the kilometrage at S, denoted by X_S, is calculated as follows:

$$X_S = \frac{(D_{R2} - D_S) X_{R1} + (D_S - D_{R1}) X_{R2}}{D_{R2} - D_{R1}} \quad (1)$$

Applying this equation to each frame allows kilometrage information to be assigned across the entire video. Additionally, travel speed can be calculated based on the relative distance between frames and the corresponding time intervals.

2.4 Equipment recognition using object detection AI

To automatically identify the types and positions of equipment from captured visible-light images, we applied an object detection AI model that recognizes railway trackside equipment. Note that the model was built based on YOLOX [5], a deep-learning-based object detection algorithm developed by Megvii Technology in 2021 as part of the YOLO (You Only Look Once) family. Due to improvements in training methods, YOLOX achieves detection accuracy comparable to that of conventional YOLO models while using fewer parameters, providing a good balance between detection performance and processing speed. Since our proposed system must process many frames obtained from continuously recorded forward-facing train images, YOLOX was adopted due to its efficiency and robustness.

This study used approximately 18,000 forward-facing train images as training data to construct a model that can recognize 22 categories of trackside equipment. The trained object detection AI outputs bounding boxes that represent both the detected equipment types and their locations within the input image. An example of detection results is shown in Fig. 6.

3. Estimation method of the external deterioration level of signalling equipment boxes

3.1 Overview of the method

Visual inspections of signalling equipment boxes depend greatly on the subjective judgment of workers. If deterioration could be expressed numerically, the difference between inspection operators or between regions could be reduced. To achieve this, our system uses AI to estimate the level of external deterioration of equipment boxes captured in forward-facing train images.

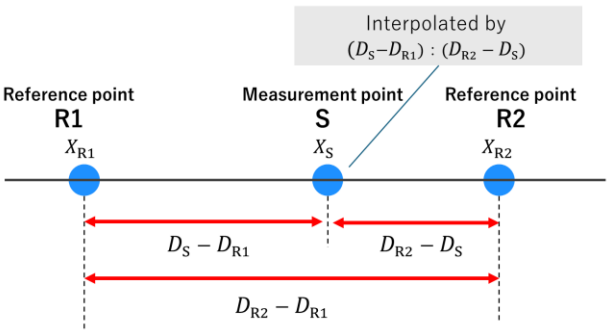

Fig. 5 Estimation of kilometrage based on reference points

From the images extracted by the object-detection AI, the proposed method applies an image classification model (AI that assigns categories to images) to estimate a continuous deterioration score from 0 to 10, based on images extracted by the object-detection AI. Figure 7 shows an overview of the proposed algorithm for estimating deterioration. A dataset of around 3,500 images was created, and each image was manually rated by inspection operators on a scale of 0-10. Using this dataset, we trained a model based on the Swin Transformer [6] architecture.

The Swin Transformer is an AI that was originally developed for language processing. Since it uses self-attention, it allows the model to focus on relationships between different parts of the image. Therefore, this is similar to how an inspection operator checks several rusted areas in relation to each other. The Swin Transformer processes images in small patches and combines information across multiple scales, making it robust even when the apparent size of the box changes due to train distance. We further adapted the model for "ordinal" deterioration levels by using a loss function that penalizes large deviations more strongly than small ones.

Finally, the model outputs scores for each class and converts them into probabilities using the Softmax function, which turns scores into likelihoods. A weighted average of these probabilities yields a continuous deterioration score, which enables quantitative evaluation based on discrete labels.

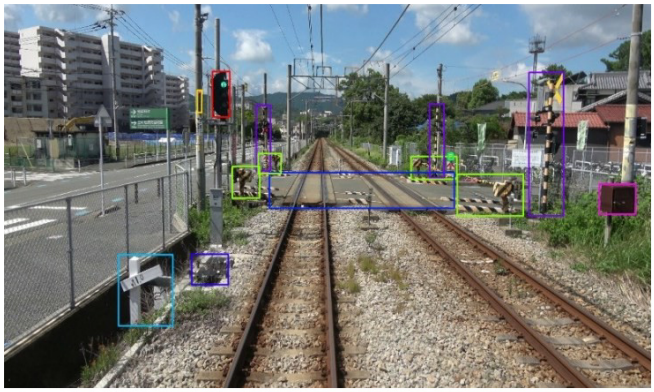

Fig. 6 Example of detection results

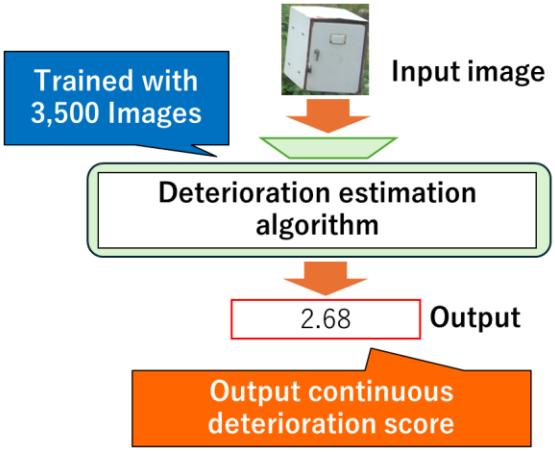

Fig. 7 Deterioration estimation algorithm

3.2 Accuracy evaluation

3.2.1 A Comparison of results obtained using the proposed method and those obtained by inspection workers

To evaluate the proposed method, 1,410 images of signalling equipment boxes were extracted from forward-facing train videos. Their deterioration levels (0-10) of these boxes were then estimated by experienced inspection operators. Figure 8 shows a violin plot comparing inspection operator assigned values (true values) with the model's continuous estimates. The estimated values were generally close to the true values, with the medians matching closely. However, slight shifts were observed at levels 0 and 10 due to the boundary effects of weighted averaging.

The classification accuracy was then evaluated by considering an estimate to be correct if the error relative to the true value was within ±0.5. Under this criterion, the accuracy rate was 78.1%. This was mainly caused by variability in human labels at low deterioration levels. However, this has minimal impact on practical use, as the system is primarily intended to detect heavily deteriorated equipment.

3.2.2 Comparison results obtained using the proposed method with on-site inspection results

To evaluate the practical usefulness of the AI-based deterioration estimation, we compared the scores of on-site inspections, during which engineers evaluate signalling equipment boxes for internal and bottom corrosion that cannot be seen in forward-facing images. We focused on 57 level crossing equipment boxes that were used in the previous experiment, as described in the preceding section.

During annual field inspections, engineers classify each box as "No Problem," "Caution Required" or "Action Required." We retrieved the forward-facing images taken closest to the inspection date for each box and obtained the AI-estimated deterioration scores. Figure 9 shows the relationship between on-site ratings and AI estimates. Of the 57 boxes, 47 were labeled No Problem, 1 Caution Required, and 9 Action Required. Their average AI scores were 1.82, 3.85, and 3.54, respectively. Although the Caution Required group contained only one sample, the Action Required group still showed scores about 1.9 times higher than No Problem, indicating a meaningful correlation between AI estimates and human field evaluation.

Figures 10 and 11 show Action Required samples with the highest and lowest AI scores. The box in Fig. 10 received a high score due to visible rust on the top surface rust, whereas the box in Fig. 11 showed little external deterioration despite internal corrosion, resulting in a score close to 3.0 like No Problem samples. If a threshold such as 3.0 were used for flagging Action Required boxes, some false positives would occur. However, such a threshold could still be effective for preliminary screening or supporting visual inspections. For practical implementation, further refinement, such as safety-margin-based threshold design, is needed.

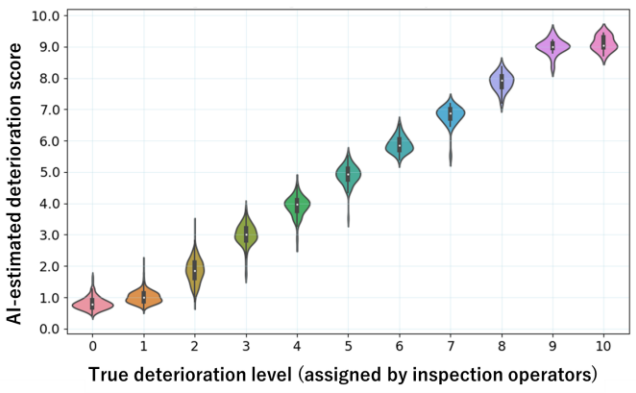

Fig. 8 Comparison between AI estimates and inspection-operator-evaluated deterioration levels

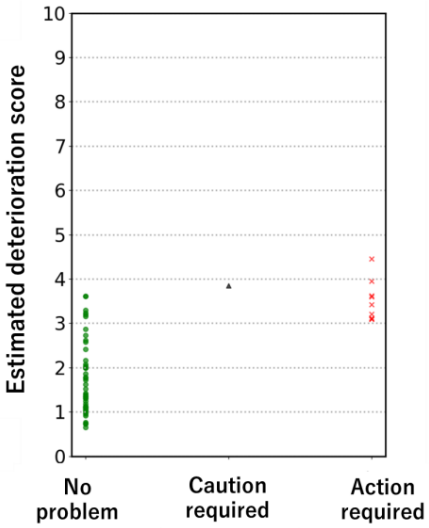

Fig. 9 Comparison model results and on-site inspection results

Fig. 10 Most deteriorated level crossing equipment box

Fig. 11 Least deteriorated level crossing equipment box

4. Conclusions

To reduce the labor and cost associated with managing trackside equipment, we developed a system that enables trackside conditions and equipment to be visually inspected without the need for on-site visits. This system uses forward-facing images captured by a commercial video camera.

This paper described the methods used in the system, including the estimation of kilometrage, the generation of long bird's-eye view image of the track surface, the automatic recognition of equipment, and the quantitative estimation of the level of external deterioration of signalling equipment boxes.

Furthermore, we confirmed that the external condition of level crossing equipment boxes can be quantitatively evaluated based on continuous deterioration values obtained from forward-facing images using the deterioration estimation method developed in this study.

In the future, we plan to conduct further studies to develop a method for monitoring equipment deterioration. This involves acquiring image data over long periods of time and applying predictive models based on accumulated data. Ultimately, we aim to build a system that will contribute to the automation and efficiency of inspection operations.

References

[1] Mukojima, H., and Nagamine, N., "Development of a support system for managing signaling equipment using forward-facing train videos captured with a handheld camera," *RTRI Report*, Vol. 36, No. 8, pp. 45-50, 2022 (in Japanese).

[2] Nagamine, N., and Mukojima, H., "Signal equipment recognition method from handheld camera images," *IEEJ Technical Meeting on Transportation and Electric Railway / Linear Drives*, TER-20-025, 2020 (in Japanese).

[3] Burt, P. J., and Adelson, E. H., "A multiresolution spline with application to image mosaics," *ACM Transactions on Graphics*, Vol. 2, No. 2, pp. 217-236, 1983.

[4] Mukojima, H., and Nagamine, N., "Generation of long bird's-eye-view images around railway tracks using forward-facing train videos for reducing maintenance workload of wayside equipment," *IEEJ Transactions on Industry Applications*, Vol. 144, No. 3, pp. 60-69, 2024 (in Japanese).

[5] Ge, Z., Liu, S., Wang, F., Li, Z., and Sun, J., "YOLOX: Exceeding YOLO Series in 2021," arXiv preprint arXiv:2107.08430, 2021.

[6] Liu, Z., Lin, Y., Cao, Y., et al., "Swin Transformer: Hierarchical Vision Transformer Using Shifted Windows," *Proceedings of the IEEE/CVF International Conference on Computer Vision*, pp. 10012-10022, 2021.

Authors

Riho MAEDA
Researcher, Image Analysis Laboratory, Information and Communication Technology Division
Research Areas: Computer Vision, Image Processing

Hiroki MUKOJIMA
Senior Researcher, Image Analysis Laboratory, Information and Communication Technology Division
Research Areas: Computer Vision, Image Processing

Nozomi NAGAMINE, Ph.D.
Senior Chief Researcher, Head of Image Analysis Laboratory, Information and Communication Technology Division
Research Areas: Computer Vision, Image Processing, Signalling Systems

Summaries of Papers in RTRI REPORT (in Japanese)

Pressure Tightness Model for Freight Containers Passing in Tunnel

Sanetoshi SAITO

(Vol.40, No.2, 1-11, 2026.2)

In mixed traffic, high-speed and conventional trains share the same tracks. This exacerbates the problem of aerodynamic loads due to pressure variations in the tunnel on conventional trains when they pass high-speed trains in a tunnel. In particular, freight cars, such as containers and wagons, may be damaged by these loads, as their structural strength is lower than that of passenger trains. To predict the aerodynamic loads, it is necessary to estimate not only the external pressure (i.e., the pressure in the tunnel) but also the internal pressure. This study involved conducting an experiment using a train model launcher to measure the pressure inside and outside a model freight container. The pressure tightness model proposed in previous studies was validated quantitatively using experimental results. It was also confirmed that the pressure tightness model which takes into account the influence of the elastic deformation of vehicle bodies is suitable for predicting the internal pressure in vehicles with low rigidity, such as freight cars.

A Method to Estimate Newly Fallen Snow Density Based on Disdrometer Data

Kazuya TAKAMI

(Vol.40, No.2, 12-18, 2026.2)

This study proposes a method to estimate the density of newly fallen snow using disdrometer data. By analyzing the particle size and fall velocity distributions obtained from a disdrometer, the degree of riming is quantified and used to derive snow density. Compared to conventional temperature-based methods, the proposed approach shows a stronger correlation ($R = 0.78$) and significantly lower RMSE (10.5 kg m^{-3}). This technique enables automated, high-frequency estimation of snow density, improving snowfall depth calculations and snow hazard assessments, especially under sub-zero conditions where conventional temperature-based methods are less accurate.

Proposal of Modeling Method for Segment Joints Using Element Experiments for Shield Tunnel and Its Application to Structural Analysis

Kaho KINOSHITA, Takashi USHIDA, Kazuhide YASHIRO, Akira HOSODA

(Vol.40, No.2, 19-30, 2026.2)

Full-scale bending tests of segment joints for shield tunnels are important for understanding and properly evaluating the behavior of joint sections. However full-scale tests are costly and time-consuming. Therefore, numerical analysis is expected to complement these tests. This study proposes a modeling method for segment joints. This method is based on behavior observed in full-scale joint bending experiments using a three-dimensional FEM analysis. Firstly, a model case of railway shield tunnels was established. Secondly, a series of steps was demonstrated, from setting rotation characteristics with finite element analysis to analyzing the frame structure of the shield tunnel, illustrating the usefulness of this study.

A Method for Estimating Bridge Deflection of Multi-bridge Section Based on Track Geometries Measured by 2- Bogie Track Inspection Vehicle

Koji HATTORI, Kodai MATSUOKA, Hirofumi TANAKA

(Vol.40, No.2, 31-41, 2026.2)

A drive-by methodology for estimating bridge deflection based on the difference between two track geometries (DTG) has been proposed. Through numerical simulations, this paper demonstrates that the DTG in a section of consecutive simply supported bridges is equal to the sum of the DTG of each bridge. Based on this property, we propose a simultaneous estimation method for each bridge deflection using linear regression. On-site verification on five consecutive bridges indicates that the proposed method can estimate bridge deflection with an error of 3% or less, provided that the bearings are defect-free.

Automatic Crew Scheduling Algorithm After a Large-scale Natural Disaster

Satoshi KATO, Jun IMAIZUMI, Taichi NAKAHIGASHI

(Vol.40, No.2, 42-51, 2026.2)

When sections of railway lines are partially disrupted due to damage from large-scale natural disasters, it is necessary to prepare crew schedule plans for temporary timetables. In such cases, crew schedule plans ensure that the duties once assigned to crews are not altered. As this task is time-consuming for schedule planners, there is a desire for an automatic crew scheduling method. This paper focuses on crew scheduling in the aftermath of a large-scale natural disaster and proposes an automated generation algorithm based on mathematical optimization. In addition, we show the results of computational experiments based on a real disaster case, demonstrating that the proposed algorithm can generate an efficient schedule plan in a short time.

Evaluation of Yield Management with Randomized Controlled Trial (A/B Testing)

Ryosuke MATSUMOTO

(Vol.40, No.2, 52-61, 2026.2)

This study proposes a method to evaluate yield management through sales slot control for discount railway tickets using a randomized controlled trial (A/B test). Implemented on an operating railway line, this method empirically shows how sales slot adjustments influence revenue. The results demonstrate that the appropriate strategy is time-dependent: in certain periods, increasing slots stimulates demand and boosts revenue, while in others, decreasing slots suppresses down-selling for a similar positive effect. As the first published case of A/B testing for yield management in the Japanese railway industry, this paper provides a practical framework for implementation and analysis.

Door Pinching Detection Using Door End Rubber with Built-in Pressure-sensitive Sensor

Shogo MAMADA, Hiroshi TANAKA, Momoko YOSHIDA, Tatsuya OTA, Yukihiro AKASAKA, Rena WATANABE

(Vol.40, No.3, 1-10, 2026.3)

Current door pinch detection devices cannot detect narrow objects being pinched, nor the dragging caused by such pinching. To detect these events, we have developed a door pinch detection device (DPDD) that uses a door end rubber with a built-in pressure-sensitive sensor (DRBPS). The developed device can detect objects with a diameter of 8 mm or larger being pinched, as well as dragging occurring outside the vehicle at loads of approximately 150 N or less. The DPDD transmits detection information obtained by the DRBPS to the vehicle body using a non-contact power supply device, making it easy to install on existing vehicles. In a test in which the DPDD was installed on a real vehicle for around one year, there were no instances of missed detections or false alarms.

Effect of Operating Conditions on the Life of Traction Motor Bearings
Daisuke SUZUKI, Ken TAKAHASHI
(Vol.40, No.3, 11-18, 2026.3)

Currently, there is no practical method for determining the life of bearings used in traction motors for railway vehicles. Therefore, the first step in establishing such a method is to investigate how operating conditions affect bearing life. In this report, using a test rig capable of rotating traction motor bearings under conditions close to those experienced in real operating environments, we investigated the effects of "bearing temperature," "vibration acceleration," and "grease mass" on bearing life. The results showed that altering any of these conditions affects life, and that this effect can be quantified.

Proposal of New Maintenance Standard Values of Track Irregularity for High-speed Type Turnout
Katsutoshi SHIOTA, Ayano MIYASHITA
(Vol.40, No.3, 19-28, 2026.3)

Maintenance standard values for track irregularity at high-speed type turnouts where trains pass through the main line of the turnout at a speed of 120 km/h on a conventional line, are managed with stricter values than those for general turnouts. These values were empirically determined from past running tests. In this study, we constructed turnout running simulation models which enable us to quantitatively evaluate the effects of track irregularity on turnout component damage and vehicle dynamics, in order to establish new maintenance values on the basis of mechanical evidence. Furthermore, we carried out various studies on track irregularity using each constructed simulation model and proposed new maintenance standard values.

Study on Frost Damage Area of Slab Track Filling Layer
Takatada TAKAHASHI, Yoshifumi MISAWA, Shigehiko SAITO
(Vol.40, No.3, 29-35, 2026.3)

Some slab tracks have sustained frost damage due to repeated freezing and thawing in their filling layers. Previous studies have shown that frost damage extends further at the corners than at the sides; however, the underlying cause remains unclear. In this study, we conducted temperature variation tests and unsteady heat conduction analyses using the finite element method. The results showed that heat transfer from the side and end faces of the slab track expands the freezing area at the corners.

Survey of Load Condition and Evaluation of Bending Load Capacity of Aged Shinkansen Prestressed Concrete Sleeper
Tsutomu WATANABE, Shintaro MINOURA, Keiichi GOTO
(Vol.40, No.3, 36-44, 2026.3)

In order to quantify the actual load condition of the prestressed concrete (PC) sleeper for high-speed trains, field measurement tests and numerical analyses were conducted on PC sleepers. As a result, it was clarified that the loading condition of the PC sleepers had a margin of safety compared to the design limit value for cracking due to bending. In addition, the results of the bending tests of the PC sleepers specified in Japanese industrial standard showed that the load capacity of the PC sleepers tends to decrease with age. Although the load capacity of PC sleepers over 50 years old met the standard value of bending fracture load, in some cases this was lower than the standard value of flexural proof load of crack.

Formalization of Tacit Knowledge of Field Engineers using Statistical Occurrence Prediction Model of Point Machines Lock Adjustment
Wataru INABA, Kodai MATSUOKA, Shigeyuki TAMEHIRO, Mitsuyoshi FUKUDA, Kiyoyuki KAITO
(Vol.40, No.3, 45-54, 2026.3)

This study aims to estimate a mixed Weibull hazard model from inspection records of lock adjustment, which are a major inspection item for point machines with a short inspection cycle. Furthermore, we conducted a survey to verify whether tacit knowledge regarding lock adjustment held by engineers has been formalized through the statistical model. The result clarified that the characteristic of lock adjustment, wherein one adjustment triggers the next, has been formalized as acceleration parameter estimates for an initial defect type. In addition, ten of the sixteen point machines with large heterogeneity parameter estimates, were identified as being subject to frequent adjustments. This confirms that some of the explicit knowledge is consistent with the tacit knowledge of engineers.

Analysis and Verification of Passengers' Train Choice Behavior Considering the Imbalance in Load Factors between Extra and Regular Trains
Daiki OKUDA, Seiya HOKIMOTO, Wataru INABA
(Vol.40, No.3, 55-61, 2026.3)

On high-grade lines served by Shinkansen or limited express trains, the load factor of extra trains is often significantly lower than that of regular trains, even when the level of service is comparable. This study conducted a basic investigation into passengers' train choice behavior, as it is considered a potential factor contributing to this imbalance. Firstly, a comparative analysis of booking curves for extra and regular trains was conducted to identify passengers' train choice patterns. Secondly, based on the identified choice patterns, two hypotheses regarding the relationship between load factor disparity and passenger choice behavior were formulated under different assumptions. Finally, the validity of these hypotheses was verified using actual choice behavior data obtained from an on-board questionnaire survey conducted on a certain high-grade line.

Effect of Train Underbody Meandering Flow on Fluctuating Aerodynamic Force of a Tail Car
Takumi ABE, Koji NAKADE
(Vol.40, No.4, 1-11, 2026.4)

This study employs large-eddy simulation (LES) to examine the relationship between meandering flow beneath the underbody of a six-car train model and the fluctuating lateral aerodynamic forces acting on the tail car. While previous studies have identified large-scale meandering flow structures and clarified their role in flow-induced vibrations of car body within tunnel, their influence on the aerodynamic forces of a tail car in open-air conditions remains unclear. The present results demonstrate that fluctuating aerodynamic forces on the tail car intensify in synchronization with the meandering flow. Mode decomposition further reveals that the dominant fluctuating flow structure is an antisymmetric mode, with a frequency close to that of the meandering flow. This mode generates significant fluctuating aerodynamic force near the tail region.

Countermeasures for Friction-Induced Vibration in Pantographs Using Modal Coupling Strength Analysis
Shigeyuki KOBAYASHI, Yuki AMANO, Yoshitaka YAMASHITA
(Vol.40, No.4, 12-21, 2026.4)

This study investigates friction-induced unstable vibrations in railway pantographs through modal coupling analysis. A flexible multibody dynamics model was developed to examine the effect of sliding friction on natural modes. Coupling strength was introduced as a quantitative measure. The

results showed that under knuckle-backward conditions, increasing friction narrows the frequency gap between the first and fourth modes, causing instability above a friction coefficient of 0.79. Parametric studies revealed that reducing plate spring stiffness weakens coupling and suppresses vibrations. Hammering tests and modal analysis confirmed the validity of the simulations, showing that reducing the thickness of plate springs decreases coupling strength and mitigates instability.

Automatic Generation of Maintenance Worker Scheduling at Rolling Stock Depot

Satoshi KATO, Tatsuya KOKUBO, Taichi NAKAHIGASHI
(Vol.40, No.4, 22-31, 2026.4)

This paper proposes an automated scheduling method for maintenance worker at rolling stock depots. Maintenance worker schedules at rolling stock depots are daily plans assigned to teams of maintenance worker for tasks such as cleaning rolling stock and performing inspection during turnaround operations of superior trains. The effectiveness of the proposed method is evaluated by comparing the schedules it generated with actual schedules, and those generated by a mathematical programming method, and a local search method. The results indicate that the proposed method generates maintenance worker schedules that satisfy high priority relaxable constraints within a practical computation time.

Retrofit for Preventing Fatigue Crack Initiation at End Stiffener Using Splice Plate with Bearing-type Bolt

Yoshinori YOSHIDA, Kengo ANAMI, Yasushi NAGASAKA, Toshio TAKEBUCHI, Yusuke KOBAYASHI
(Vol.40, No.4, 32-39, 2026.4)

One of the typical fatigue cracks found in welded girders of railway steel bridges is observed at the bottom of end stiffener. Bearing settlement leads to stress concentration and fatigue cracking at the bottom of end stiffener. Consequently, the necessary retrofits impose a significant maintenance burden. This study proposes a method for retrofitting end stiffener using splice plate with bearing-type bolt for pressing. This paper reports the results of static load test and cyclic load test conducted for evaluating the applicability of the proposed method.

Predicting Tunnel Deterioration via Subsurface Brine Flow at Tidal River Crossing

Takashi USHIDA, Takashi NAKAYAMA, Kaho KINOSHITA, Kenjiro TERADA
(Vol.40, No.4, 40-52, 2026.4)

Progressive aging of various infrastructure is making maintenance more important. In urban areas, many reinforced concrete railway tunnels, constructed using the cut-and-cover or shield methods, are beginning to show signs of degradation due to material deterioration. Cases of rebar corrosion caused by chloride ions have been reported, particularly in tunnels crossing tidal rivers. Since repeated repairs are often required due to chloride attack, preventive maintenance is expected to reduce maintenance efforts. This study proposes a method for predicting deterioration via subsurface brine flow, and demonstrates its application through a model case.

Evaluation of Pile Group Efficiency in Pile Foundations without Footing Beams

Ichiro DOI, Ryuga NOHARA, Takeshi YAMAMOTO, Taisuke SANAGAWA, Shuji TAMURA
(Vol.40, No.4, 53-63, 2026.4)

When designing pile foundations against lateral forces, pile group efficiency is considered when evaluating lateral subgrade reaction. Pile group efficiency is generally assessed under the assumption that footing beams or footings are used. However, in some cases, such as pile foundations for overtracks buildings, neither footing beams nor footings are used. Therefore, this study investigates the influence of footing beams on pile group efficiency through centrifuge model tests and 3D elasto-plastic finite element analysis. The results indicate that the absence of footing beams enhances the pile group efficiency. The mechanism is elucidated by examining the pile deformation modes and the stress distribution in the surrounding soil.

Quantitative Evaluation of Track Characteristics and Optimization of Resource Allocation for Maintenance

Mami MATSUMOTO, Kenya MORI, Daiki SAITO, Shuhei KONNO, Yousuke TSUBOKAWA
(Vol.40, No.4, 64-71, 2026.4)

Sustainable management of railway tracks requires an effective investment plan for allocating limited resources to ensure future infrastructure availability. In order to achieve this, it is necessary to quantify the track characteristics, establish the target maintenance level for track irregularity based on these characteristics, and develop an economical track maintenance plan. By applying principal component analysis, we develop a method that quantitatively evaluates the track characteristics based on various influencing factors, which are verified using date on a railway operator. We develop a "track maintenance condition simulation tool" to determine target maintenance levels and optimize the allocation of investment resources based on the track characteristics and the predicted track irregularity values. Using this tool, we evaluate the relationship between the target maintenance levels and investment resources through a scenario analysis.

QUARTERLY REPORT of RTRI

第 67 巻　第 2 号
2026 年 5 月 1 日　発行
監修・発行所：公益財団法人鉄道総合技術研究所
〒 185-8540　東京都国分寺市光町 2-8-38
発行人：芦谷公稔
問い合わせ：鉄道総研広報

Vol. 67, No. 2
Published date: 1 May 2026
Supervision/Publisher: Railway Technical Research Institute
Address: 2-8-38 Hikari-cho, Kokubunji-shi, Tokyo 185-8540, Japan
Issuer: Dr. Kimitoshi ASHIYA
Contact us: Public Relations, Railway Technical Research Institute
Mail Address: rtripr@rtri.or.jp

QUARTERLY REPORT of RTRI

RAILWAY TECHNICAL RESEARCH INSTITUTE

Printed in Japan